NOVEL NONLINEAR OPTICS AND QUANTUM OPTICS APPROACHES FOR ULTRASOUND-MODULATED OPTICAL TOMOGRAPHY IN SOFT BIOLOGICAL TISSUE

A Disseratation

by

HUILIANG ZHANG

Submitted to the Office of Graduate Studies of
Texas A&M University
in partial fulfillment of the requirements for the degree of

DOCTOR OF PHILOSOPHY

December 2010

Major Subject: Electrical Engineering

Novel Nonlinear Optics and Quantum Optics Approaches for Ultrasound-Modulated Optical Tomography in Soft Biological Tissue

NOVEL NONLINEAR OPTICS AND QUANTUM OPTICS APPROACHES FOR ULTRASOUND-MODULATED OPTICAL TOMOGRAPHY IN SOFT BIOLOGICAL TISSUE

A Disseration

by

HUILIANG ZHANG

Submitted to the Office of Graduate Studies of
Texas A&M University
in partial fulfillment of the requirements for the degree of

DOCTOR OF PHILOSOPHY

Approved by:

Chair of Committee,	Philip R. Hemmer
Committee Members,	Robert D. Nevels
	Jun Kameoka
	Kenith Meissner
Head of Department,	Costas N. Georghiades

December 2010

Major Subject: Electrical Engineering

ABSTRACT

Novel Nonlinear Optics and Quantum Optics Approaches for Ultrasound-Modulated Optical Tomography in Soft Biological Tissue. (December 2010)

Huiliang Zhang, B.S., Peking University, China

Chair of Advisory Committee: Dr. Philip R. Hemmer

Optical imaging of soft biological tissue is highly desirable since it is nonionizing and provides sensitive contrast information which enables the detection of physiological functions and abnormalities, including potentially early cancer detection. However, due to the diffusive nature of light in soft biological tissue, it is difficult to achieve simultaneously good spatial resolution and good imaging depth with pure optical imaging modalities.

This work focuses on the ultrasound-modulated optical tomography (UOT): a hybrid technique which combines the advantages of ultrasonic resolution and optical contrast. In this technique, focused ultrasound and optical radiation of high temporal coherence are simultaneously applied to soft biological tissue. The intensity of the sideband, or ultrasound 'tagged' photons depends on the optical absorption in the region of interest where the ultrasound is focused. Demodulation of the optical speckle pattern yields the intensity of tagged photons for each location of the ultrasonic focal spot. Thus UOT yields an image with spatial resolution of the focused ultrasound — typically submillimeter — whose contrast is related to local optical absorption and the diffusive

properties of light in the organ. Thus it extends all the advantages of optical imaging deep into highly scattering tissue. However lack of efficient tagged light detection techniques has so far prevented ultrasound-modulated optical tomography from achieving maturity. The signal-to-noise ratio (SNR) and imaging speed are two of the most important figures of merit and need further improvement for UOT to become widely applicable.

In the first part of this work, nonlinear optics detection methods have been implemented to demodulate the "tagged" photons. The most common of these is photorefractive (PR) two wave mixing (TWM) interferometry, which is a time-domain filtering technique. When used for UOT, it is found that this approach extracts not only optical properties but also mechanical properties for the area of interest. To improve on TWM, PR four wave mixing (FWM) experiments were performed to read out only the modulated light and at the same time strongly suppressing the 'untagged' light.

Spectral-hole burning (SHB) in a rare-earth-ion-doped crystal has been developed for UOT more recently. Experiments in $Tm^{3+}:Y_3Al_5O_{12}$ (Tm:YAG) show the outstanding features of SHB: large angle acceptance (*etendue*), light speckle processing in parallel (insensitive to the diffusive light nature) and real-time signal collection (immune to light speckle decorrelation). With the help of advanced laser stabilization techniques, two orders of magnitude improvement of SNR have been achieved in a persistent SHB material ($Pr^{3+}:Y_2SiO_5$) compared to Tm:YAG. Also slow light with PSHB further reduces noise in Pr:YSO UOT that is caused by polarization leakage by performing time-domain filtering.

DEDICATION

To my parents and friends for their love

ACKNOWLEDGEMENTS

I would like to thank my graduate study advisor and committee chair, Dr. Philip Hemmer, for always being available for me, for providing an intellectually stimulating and friendly environment for research, and for all the time he spent on discussing and correcting the manuscripts with me. In every sense, none of this work would have been possible without him. I also thank Dr. Lihong V. Wang, Dr. Stefan Kröll, Dr. Hong Liang and Dr. Fedor Jelezko for their advice and help in research collaboration. I thank my committee members, Dr. Nevels, Dr. Kameoka and Dr. Meissner, for their valuable instructions. A special thanks to Dr. Andrew Chan and Dr. Jim Ji for advice about career in academia.

Thanks also go to my co-workers and colleagues, Dr. Chang-Seok Shin, Dr. HoNam Yum, Dr. Zhijie Deng, Dr. Mughees Khan, Dr. Dekui Qing, Dr. Changdong Kim, Xiao Xu, Dr. Chulhong Kim, Dr. Sava Sakadžić, Dr. Roger Zemp, Dr. Youzhi Li, Dr. Lars Rippe, Mahmood Sabooni, Wenlong Yang, Dr. Luohan Peng and Dr. Helmut Fedder for their extensive support and co-work during my research. I also want to extend my gratitude to the department faculty and staff for making my time at Texas A&M University a great experience.

Finally, thanks to my mother and father for their unconditional love and to my extended family in China for their encouragement. Also thanks to all my beloved friends in my life.

NOMENCLATURE

CCD	charge-coupled device
MRI	magnetic resonance imaging
UOT	ultrasound-modulated optical tomography
DOT	diffuse optical tomography
OCT	optical coherence tomography
PAT	photo-acoustic tomography
US	ultrasound
SNR	signal-to-noise ratio
SBR	signal-to-background ratio
SO_2	saturation level of oxygen
PR	photorefractive
TWM	two wave mixing
FWM	four wave mixing
RE	rare earth
SHB	spectral-hole burning
PSHB	persistent spectral-hole burning
Tm:YAG	$Tm^{3+}:Y_3Al_5O_{12}$
Pr:YSO	$Pr^{3+}: Y_2SiO_5$
Eu:YSO	$Eu^{3+}: Y_2SiO_5$
DPSS	diode pumped solid state

1D	one dimensional
2D	two dimensional
RF	radio-frequency
dc	direct current
ac	alternating current

TABLE OF CONTENTS

CHAPTER Page

CHAPTER Page

LIST OF FIGURES

FIGURE Page

FIGURE Page

FIGURE Page

FIGURE Page

FIGURE Page

FIGURE Page

LIST OF TABLES

CHAPTER I

INTRODUCTION

A. Importance of UOT

In past a few decades, novel optical imaging techniques have been increasingly explored as new medical imaging methods. These techniques have been critical to map morphological and functional information of biological tissues, using optical properties such as absorption, scattering, polarization and *etc*. from the microscopic to the macroscopic level. They also make use of non-ionizing radiation (~2 eV), and are highly sensitive to endogenous and exogenous optical contrast as well as being relatively cost-effective[1-6].

Optical contrast can be categorized by three properties: absorption, scattering, and polarization. Hemoglobin and melanin are major optical absorbers in biological tissues in the visible and near-infrared (NIR) regions. The imaging of melanin is used in melanoma studies, and the quantification of hemoglobin concentration can be extended to estimate the total hemoglobin concentration and saturation of oxygen in blood, which are the hallmarks of tumors. By exploiting differential absorption at a set of suitable visible or near infrared wavelengths, the concentrations of two forms of hemoglobin, oxyhemoglobin and deoxyhemoglobin, can be quantified. Using these concentrations, the saturation level of oxygen (SO_2), a physiologically important functional parameter,

---

This dissertation follows the style of *Nature Physics*.

can be inferred. For example, tumor development usually involves hypoxia, a low level of SO_2. Therefore, blood vasculature and SO_2 can be readily mapped by modalities sensitive to optical absorption[6]. Optical scattering is able to provide the size of optical scatters such as cell nuclei, mitochondria, and collagen fiber. Thus, variations in scattering coefficient can provide information about neuronal activity and diseased tissue[7]. Optical polarization is related to anisotropic tissue components such as collagen and fibers. In addition to mentioned optical properties, optical spectra, optical Doppler effect, Raman scattering, bioluminescence and so on, all these information makes optical imaging extremely attractive for diagnostics and treatment.

Due to the mentioned motivations, an impressive array of optical imaging modalities, such as optical coherence tomography (OCT); diffuse optical tomography (DOT); photoacoustic tomography (PAT) can now provide structural, functional, and molecular information about the scattering biological tissue based on various optical contrast mechanisms[3,4,8].

Optical imaging offers excellent intrinsic optical contrast but suffers from poor spatial resolution at depths beyond one transport mean free path in biological tissue due to strong scattering of light in biological tissue. Diffuse optical tomography (DOT) with model-based reconstruction is capable of providing optical scattering and absorption, using diffusive light, so the penetration depth is extended to a few centimeters[5]. However, this technique still struggles with poor spatial resolution, typically 1/10 of the imaging depth. To overcome the drawback of pure optical imaging techniques, two ultrasound-mediated optical imaging techniques, ultrasound-modulated optical

tomography (UOT)[9] and photoacoustic tomography (PAT)[4], have been studied. Both imaging techniques take advantages of strong optical contrast and high ultrasonic spatial resolution, so the spatial resolution and imaging depth are scalable and within the reach of diffusive photons.

B. Prior Work in UOT: Literature Review

In the very beginning (the end of 1980s), A patent by Dolfi and Micheron[10] illustrates the idea how to use nonlinear optics method to extract "frequency marking" or "sound tagged" photons. Marks *et al.*[11] gives a collection of experimental approaches and results for pulsed sound tagging light information extraction.

Inasmuch as CW UOT (alone) does not give ultrasound axial resolution, different approaches have been investigated to obtain an image of a cross section containing the ultrasonic axis. Most straightforward method is to axially scan the ultrasound beam focus (still in ultrasound CW mode) as reported by Lévêque-Fort[12]. However its resolution is poor because the axial dimension of the ultrasonic focal zone is quite long. US focal zone is typically a cylinder of 2 mm in diameter and 20 mm or more in length. Wang and Ku[13] proposes frequency-swept UOT technique and realizes this method in the quasi-ballistic regime first. The basic idea is to tag different positions (in sound axis) with different frequencies of sound modulation. So in principle it is quite similar to MRI. Due to sound energy spread into a pretty wide frequency range, the SNR needs to be improved by signal processing. After integration of this method with parallel signal processing[14], 2.7 mm thick buried rubber (optical absorber) can be imaged inside 1.2 cm

chicken breast tissue. However the tradeoff between resolution z_R in sound propagation direction is given by ($z_R \approx \frac{v_s}{\Delta f}$), where v_s, speed of sound, Δf denotes the frequency span of the chirp. As seen z_R is inversely proportional to chirp range and the signal intensity limits use of this method for deeper imaging inside soft biological tissue. In work by Yao *et al.*[14], imaging along the ultrasonic axis is accomplished by electronically scanning the time delay between laser and US, both modulated by chirp functions. Another approach combining chirped US and parallel signal processing is taking the Fourier transform of the time-domain signal recorded by each pixel in CCD camera to get US axial resolution. With this technique a better resolution (~1 mm) in US axis has been reported[15].

In analogy to OCT, a "low coherence acousto-optic source"[16] can be generated by randomizing phases of illumination light and US. The random phase law is the same for both light and US, but with a short delay between each to select the spatial coherence region, which in turn determines the US axis resolution. Because of the statistic nature of this method, averaging is inevitable and time-consuming.

Certainly the most intuitive way obtaining US axial resolution is to implement short US pulse with only several sound cycles[11], usually called Doppler mode. The advantages are obvious: 1), relatively fast imaging speed, because each A scan supplies 1D profile; 2), compatible with commercial US imaging system. The same reasons also contribute to significant success of PAT[17]. However due to poor SNR (more noise picked up because of wide signal power spectrum), pulsed US was not adopted in the

early stage of UOT research, instead CW UOT attracts most research efforts. Work of Lev and Sfez[18] revives interests of pulsed UOT, where they show that SNR can be improved by making the phase of the US pulse continuous, more specifically the phase of the ultrasound pulse trail must coincide with the phase of the next ultrasonic pulse head. In this way as every US pulse propagates, a continuous (narrow bandwidth) signal can be reconstructed to give a photon density representation for the US axial resolution. Though 3D photon densities can be mapped with this approach, no follow up research is reported mainly due to signal processing complexities and very long averaging time.

Another way to enhance the SNR of pulsed UOT is to use heterodyne digital holography[19,20], which helps by increasing heterodyne gain and filtering out speckle decorrelation noise in spatial frequency (*k* space). However a diaphragm positioned between sample and detector (to extend speckle grains over several CCD pixels) severely limits optical system *etendue*.

A simpler but quite powerful approach is to make use of adaptive optics materials, namely PR crystals or polymers, to enhance *etendue* and so SNR. Because of the novelty filter effect, high US axis resolution (millimeter) can be achieved inside 2.7 cm thick tissue phantom[21,22]. This work ignited wide-spread efforts in the UOT community. Chapter II of my thesis will focus on this topic, where our work with PR materials as well as the most recent progress from other groups will be included.

In addition to PR based UOT, Fabry-Perot cavity has also been implemented to extract tagged photons from untagged background[23] because of its well-known light frequency discrimination capability. This method distinguishes itself by its microscopy

resolution at the price of only several millimeters imaging depth[24]. To get a better noise rejection, a double-pass confocal resonator is able to image deeper (6 cm) with several mm resolution[25]. Though quite good results have been demonstrated with CFPI, several severe drawbacks are in the way for further development: 1), not scalable with different US frequency, especially in the low frequency range, 2) fixed FP linewidth and shape (Lorentzian) limits wide bandwidth pulsed signal collection, 3), small *etendue*.

Up to now, we believe that the most promising technique for UOT (with pulsed US) is spectral hole burning approach, which will be extensively discussed in chapter IV. and V. An upgraded version, i.e. spectral hole burning slow light UOT, supplements the frequency domain filtering task with time domain signal and noise separation. Slow light UOT is analogous to time-domain DOT[6].

It is worthwhile to give a brief overview of previous published work about how to physically arrange optics such that the whole working system can be well prepared for clinical application. The transmission light collection method is relatively easy because of low un-modulated background and straightforward optics arrangement[9]. However for clinical applications, reflectance geometry detection (illumination and detection in the same side of sample investigated)[26] and/or side geometry detection[27] is preferred, certainly at the price of higher requirements for signal processing sensitivity. Research efforts are also spent on side illumination. Examples include coaxial transmission system (as reported by Hisaka *et al.*[28], where US transducer and illumination laser are coaxially adjusted on one side of the sample, CCD detector on the other), coaxial reflection system[29] (optics adjustments are almost the same as reported by Hisaka *et al.*[28], except

that backscattered light was reflected to a CCD camera by a mirror with a 2.0 mm hole), reflection mode ring-shaped light illumination[30], which not only offers the advantages of the former two methods but also reduces effects of light shadow and unwanted surface modulation.

During of the UOT detection sensitivity development history, various applications have also emerged for different purposes. To name a few, noninvasive photon density measurement inside gelatin medium[31], assessment of osteoporosis with UOT[32], fluorescence detection inside turbid median[33], Optical spectroscopy[34], multi-wavelength imaging[35] and so on. Because UOT is an information rich diagnostic modality, efforts also go toward combining with other existing imaging techniques, for example with PAT[36], conventional ultrasound imaging[22] and OCT (for resolution enhancement)[37].

C. Challenges in UOT: Signal-to-Noise Ratio (SNR) and *Etendue*

Major noise sources for UOT are shot noise and speckle deccorelation noise. Yao and Wang[38] gives a complete review on this topic. A decent characterization of speckle decorrelation time for *in vivo* situation is around 0.1 ms[39], which means corresponding noise is on the order of 10 kHz. More discussions about SNR can be found in following chapters.

To have a sensitive optical detector, a significant portion of the scattered light should be collected. The parameter *etendue* (also called the light-gathering power or optical throughput[40,41]) is used to characterize the light-collection efficiency of an optical

system. Consider diffuse light from a tissue sample surface, having a direct optical path to the system, as shown in Fig. 1.1. The light-gathering power of the optical system, known as the *etendue*, is defined as the product of the collecting-lens area and the solid angle subtended at the lens by the observed region of the source. The importance of this *etendue* parameter stems from its invariance within the geometrical framework, such that

$$A\Omega = L\Omega_1 = D\Omega_2 = invariance \tag{1.1}$$

for maximum power transfer of light. In practice, the UOT detection requirement and the optical elements within the optical filter system determine the maximum available *etendue*. Consequently the external optical path (including light-collecting lens or lens system) is required to match to the optical filter system, as indicated by equation (1.1). Failure to satisfy this condition has the consequence that the filter system is not used economically to its full light-gathering capability; that is, either the front lens (or lens system) is unnecessarily large or part of the illuminated area is not viewed by the filter system.

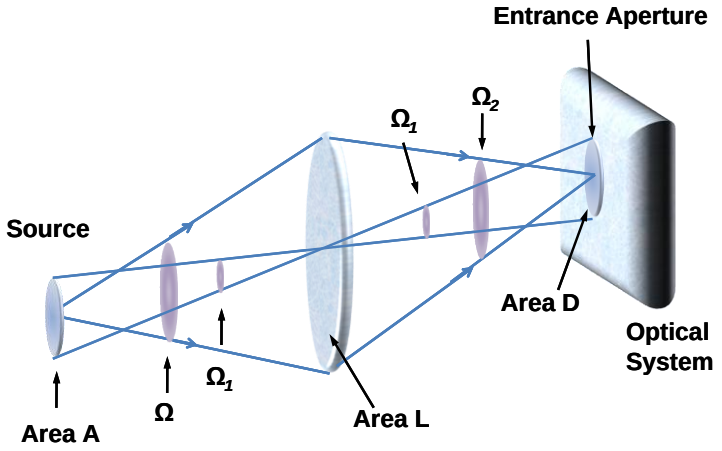

Figure 1.1 | *Etendue*, the light-gathering power of an optical system, showing the source, collecting lens and optical system (spectral filter in our case).

Suppose that, in UOT detection application, there is a stand-off distance x (geometric limitation by instruments) from the sample surface, the illumination area on the surface is estimated to be A and the filter system *etendue* is E. According to equation (1.1)

$$E = L\Omega_1 = \frac{LA}{x^2} \tag{1.2}$$

Therefore the collecting-lens system of the filter should have an area of aperture

$$L = \frac{E}{\Omega_1} = \frac{Ex^2}{A} \tag{1.3}$$

As an example, if we use a Pr:YSO crystal with effective surface area of (6 mm diameter = 28 mm^2) and crystal length of 12mm, *etendue* E for this SHB filter is ~8 sr mm^2. The illuminated area on the sample surface A = 310 mm^2 (corresponding to diameter 2 cm diffused area) and a stand-off distance x of 30 mm, then the area of the front lens of the telescope L is 65 mm^2, corresponding to a 10 mm-diameter lens. This estimation clearly shows that currently the bottle neck for light collection efficiency is not the lens system, but rather the optical filter side. Considering the commercial available lens size (~100mm), the biggest etendue can be ~1000 sr mm^2. Compared with 8 sr mm^2 etendue in our current filter system, there is plenty of room for improvement.

D. Dissertation Outline

In chapter II. nonlinear optics approach for UOT applications will be presented. The material we used is photorefractive (PR) crystal (BSO) and PR polymer. The nonlinear process is two-wave mixing and four-wave mixing. Because of its real time holography property, we can get UOT signal with several cycles of ultrasound pulse. Another obvious advantage is its much bigger *etendue* than single element detection

(which is limited by heterodyne antenna receiver property[42]). The major drawback is that SNR is low because of shot noise limitation from un-modulated background light, though four-wave mixing approach solves this problem to some extent. Interestingly, with TWM approach, optical contrast and mechanical contrast can be imaged by time gating UOT signal. This justifies UOT as an attractive multi-purpose imaging method. With FWM method, background "untagged" light has been suppressed because only frequency matching part will give phase conjugate signal. A novelty filter has been cascaded with FWM system to further decrease scatter noise.

Chapter III gives a brief introduction to rare-earth-ion doped materials and their application for spectral-hole burning. Discussion starts with rare-earth materials chemistry. The key point for its long optical coherence time is spatial shielding from outer full sub-shell to its inner partially filled sub-shell. Frozen gas of ions can model these materials well for quantum optics applications. Energy level diagrams have been given. Homogenous and inhomogeneous linewidth will be carefully discussed for their importance to understand spectral-hole burning. Details about Tm:YAG and Pr:YSO are presented because they are the most important materials used in Chapter IV, V and VI.

In Chapter IV, the basic idea using spectral hole burned inside rare-earth ion doped crystal as a spectral filter for UOT application is introduced. Performance of this quantum filter is calculated from a two-level quantum system first. Later experiments agree with this prediction and considered as quite good for "untagged" photons suppression. Experimental methods with Tm:YAG for UOT are given in details. Filtering characteristics are analyzed. 1D and 2D images are reconstructed after

frequency filtering. Resolution up to half mm has been achieved with 10 mm imaging depth.

Chapter V starts with the discussion of challenges or problems of UOT. A brief overview of prior work in UOT is given for the specific topic of “untagged” light suppression. Immediately after this discussion, Pr:YSO optical properties are discussed again with an emphasis of persistent spectral-hole burning advantages. In experimental methods part, system setup is described. Hole burning pulse sequence is given with explanation for sequence design consideration. Spectral hole performance is measured: more than 40 dB frequency discrimination capability for collimated light and 30 dB for highly scattered light. 2D images with PSHB UOT are given and discussed. A comparison for this technique with other leading techniques for UOT is shown. The key conclusion is that if equipped with a safety limitation allowed laser and straightforward modification of current experimental setup, PSHB UOT is able to achieve 18 cm imaging depth with single shot readout and video rate imaging speed.

Chapter IV is talking about time-domain filtering with slow light built on top of PSHB UOT. Because of the polarization sensitivity of Pr:YSO, incorrect polarization leakage results in the major part of residual un-filtered “untagged” background. Slow light only delays the “tagged” photons sitting within the spectral hole frequency and separates the interesting information from background, which is tuned out of spectral hole by an amount equal to the ultrasound frequency. Both theory and experiments show that we have enough time-delay bandwidth product to get enough delay for good background separation with acceptable signal distortion. Slow light experiments verify

this point by clearly resolving mm size optical absorbers inside 4.5 cm tissue phantom. Signal extraction is also successful in 9 cm tissue phantom and thick real chicken breast tissue *ex vivo*.

Chapter VI is a summary of my thesis work.

CHAPTER II

POTOREFRACTIVE TWO-WAVE MIXING AND FOUR-WAVE MIXING FOR ULTRASOUND-MODULATED OPTICAL TOMOGRAPHY

A. Review for Photorefractive (PR) Materials Based UOT

First time PR materials (inside BSO crystal and ac high voltage is applied) are used for UOT purpose is from Murray *et al*.[21] In that approach, ultrasound pulses are applied to modulate photons so that sudden wavefront changes will be induced (different from the wavefront of scattered unmodulated light). This suddenly changed light will pass through a hologram built up in the PR crystal by interfering the un-modulated light and reference beam. Without the sudden change, the PR crystal would diffract the reference beam into the direction of the scattered light. In other words, the unmodulated light actually works as a local oscillator. Diffracted reference beam and the sudden transmitted signal (modulated plus un-modulated light) beam interfere at the photodetector where any phase modulation encoded on the signal beam is converted to an intensity modulation. In this case (with pulsed ultrasound modulation). The sudden wavefront mismatch results in an intensity decrease on photodetector, which is used as UOT signal[21,22,43-45]. Advantage of this approach is its ability to detect fast changes like in pulsed ultrasound UOT. This change is usually three magnitude of order faster than photorefractive response time (hologram build up time). The penalty of this technique is its white background, which means a small signal stands on top of huge background plus noise. Even with stable lasers, shot-noise eventually will limit its application to short

ultrasound pulse UOT, because of small modulation depth in this scenario. Thermal noise or digitization noise can also be potential reasons deteriorating signals. These different types of noise prevents us from extracting UOT signal with only several ultrasound pulses (modulation depth much smaller than 1%, as shown in Fig. 2.1a, 2 cycles of ultrasound pulses), though longer burst gives better signal strength as in Fig. 2.1b. However, fewer ultrasound cycles modulate smaller volume, which gives better axial (ultrasound propagation direction) resolution. To take full advantage of resolution capability of UOT, smaller modulation volume and higher resolution is important figure of merit and requires further investigation.

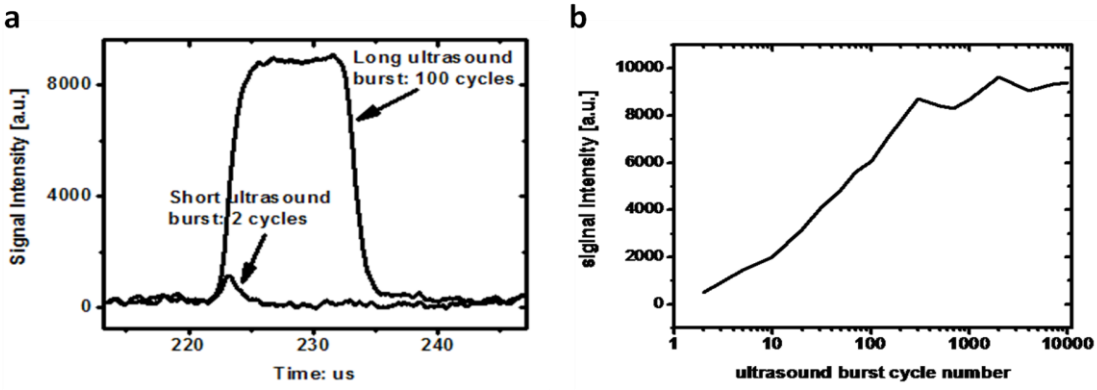

Figure 2.1 | UOT signal intensity change versus ultrasound pulse cycle number. **a**, Signal intensity comparison between the short ultrasound burst (2 cycles) and the long burst (100 cycles). **b**, Signal intensity changes as the burst length increases.

Almost at the same time, another approach of PR based UOT has been developed by Ramaz *et al*[46]: GaAs is used as the PR material and also 1064 nm high power laser improves the available UOT signal for collection. Both experiments and theory[20,47] reveal that the modulation signals obtained from both 'tagged' and 'un-tagged photon'

detection have almost the same order of magnitude. The detection of the untagged photons corresponds to a small change on a large signal (white background detection with big shot-noise limited level), while the detection of the tagged photons, which corresponds to roughly the same absolute value change, ideally yields on the contrary about 100% change on a small signal (black background detection with small shot-noise limited level). Tagged photon detection is thus expected to give less technical noise. Also photorefractive cross-polarization technique[47,48] in an anisotropic diffraction configuration has been employed to reduce parasitic light from reference beam scattering, though spurious pump scatter still cannot be totally removed this way.

With strong pump scatter and low ultrasound modulation depth, like in pulsed UOT, a good estimation of the ratio between scattered reference light, un-modulated light and modulated light is 10^4:100:1[47]. Thus detecting 'tagged' photons with PR TWM cannot easily achieve "black background detection". It has been proposed to extract ultrasound axial resolution by pulse ultrasound though random phase jumps on ultrasound and light [47], but this obviously requires more time and signal processing procedures. Even though it is claimed that GaAs pumped by high intensity laser has fast response time (τ_{PR} = 0.25 ms, monitored in-situ condition[49]), difficulties still remain about real applications into thick soft biological tissue because of its more than 10 kHz speckle de-correlation speed[47] due to Brownian motion of the scatters, and to the breast inner motions (for example, blood flow).

B. PR Two-Wave Mixing and Four-Wave Mixing Working Mechanism

Before going to the details of experiments for PR based UOT, photorefractive TWM and FWM, mechanism will be discussed first as follows.

1. PR Two-Wave Mixing (TWM)

The photorefractive effect happens when the refractive index changes according to the spatial distribution of the incident light intensity. The PR material exhibits both photoconductive and electro-optic behavior[50]. The electro-optic effect is defined as a change in the dielectric constant (or index of refraction) of a material responding to an electrical field (externally applied or generated by the material itself). Photo-induced charges create a space-charge distribution that produces an internal electrical field, which in turn, modifies the index of refraction by electro-optics effect. For a better understanding of the physics of the photorefractive behavior, brief description and illustration is given as the following. A simplified case of two plane waves interfering inside PR material is considered[51].

When two plane wave mix inside the PR materials (Fig. 2.2), a sinusoidal intensity pattern is produced as a result of light interference. Light is absorbed inside the crystal and free carriers (electrons or holes) are generated in the bright regions of the intensity pattern (constructive interference). These carriers diffuse and/or drift from the bright regions, leaving fixed charges behind. It is worth mentioning that this process can be enhanced by the application of an external electrical field, which will enhance the formation of the photorefractive grating. Without the application of the external field the

movement of the electrons is assisted only by diffusion and that state is called diffusion regime, whereas the state where electrons are forced to drift using an external field is called drift regime[50] The carriers are trapped at deep levels in the dark regions (destructive interference) resulting in a periodic space-charge distribution. The periodic space-charge field alters the refractive index of the PR material through the electro-optic effect and forms a grating of refractive index inside the material. In all, periodic intensity pattern leads to a periodic space charge distribution and finally to a periodic refractive index distribution inside the PR material.

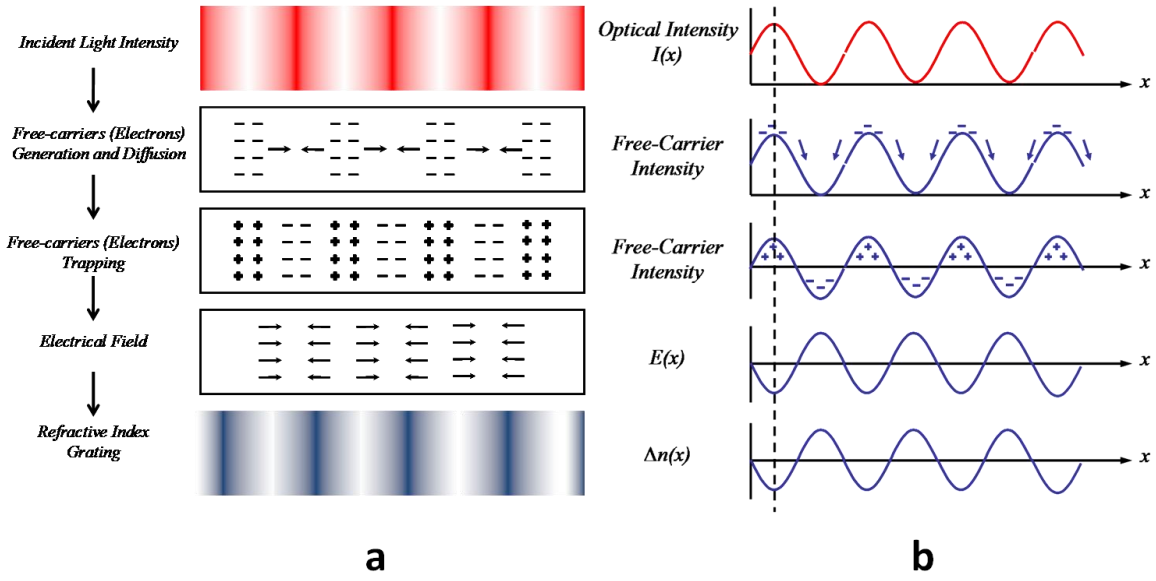

Figure 2.2 | Photorefractive procedure where incident light spatial distribution modifies the material refractive index (illustration is slightly modified from book by Saleh and Tiech[52]). **a**, Photorefractive 2D illustration illuminated by two plane waves. **b**, 1D illustration.

A simplified 1D steady-state expression for the position dependent change of the

refractive index as a function of the light intensity *I(x)*, in the absence of the application of an external electrical field can be written as [52]:

$$\Delta n(x) = -\frac{1}{2} n_0^3 r \frac{k_B T}{e} \frac{1}{I(x)} \frac{dI}{dx}, \tag{2.1}$$

where n_o is the normal refractive index of the crystal, r is the Pockels coefficient or linear electro-optic coefficient, k_B is Boltzmann's constant, T is the temperature and e is the electron charge. From Eq 2.1, it can be readily seen that, first, the change in refractive index inside PR material is proportional to both the spatial intensity gradient and the linear electro-optic coefficient; and second, the photorefractive grating will be spatially shifted by a quarter period with respect to the space intensity distribution, due to the spatial derivative of the intensity in equation 2.1. The spatial shift of a quarter wavelength (or period) is optimal to the TWM process, where the two incident beams travel together in the PR material and exchange energy only one way via diffraction from the created grating.

Though it has been assumed that both beams are plane waves, this is not true if the beams carry images or if they are diffuse light in which case they have corrugated wavefronts as in our UOT detection situation. Nevertheless, in order to get the insight for the physics of PR materials, this assumption is justified and moreover, any arbitrary wavefront can always be treated as a superposition of plane waves. Regardless of the complexity of the incident beam wavefront, the refractive index grating inside the PR material "stores" both the phase and amplitude information of the incident beam. In this sense, the PR material can work as an adaptive hologram, so that the stored information

can be read out or reconstructed by diffracting a third beam or one of the incident beams itself, depending on the polarization of the writing beams, crystal orientation, spatial phase of the grating and *etc*.[53] Many applications have been developed based on the unique features of the PR materials, such as coherent signal detection (for example, adaptive interferometers), optical image processing, read time holography and so on. In our work to detect both optical and mechanical properties with PR material based UOT, we are particularly motivated by the PR interferometer, which can compensate for the complex wavefront of the incident signal beam[54].

2. PR Four-Wave Mixing (FWM)

Based on the understanding of photorefractive TWM, FWM can be expressed as the read-out (of the refractive index grating built by interference between signal and reference beams) by a third beam, which exactly counter-propagates from the reference beam. The read-out beam counter propagates and also time reverses from the signal beam, and quite often this read-out beam is called the phase conjugate of the signal beam. Microscopic theories of the photorefractive effect generally treat photoionization of charge carriers from impurity levels. These carriers are subject to drift and diffusion in the spatially varying intensity of the recording beams and the electric field associated with the resultant space charge operates through the electro-optic effect to modulate the index of refraction. Photorefractive effect is nonlocal, with one manifestation being that the index grating is not in phase with the interference pattern ($\lambda_{grating}/4$ is the optimal situation, as mentioned in TWM process). For this reason, phase conjugation by

degenerate four-wave mixing in PR crystals is different than phase conjugation in other media and we cannot characterize the medium response by a simple constitutive third-order nonlinear constant $\chi^{(3)}$ [55]. Coupled wave equations with the associated effective third-order nonlinearities have to be employed to give a full picture of the FWM in PR material, which is well beyond the scope of this thesis.

Our experiments for UOT with FWM employ the transmission grating holography approach. The roles of reference and object (signal beam) are exchanged among the four waves, so that there are two types of gratings as illustrated in Fig. 2.3.

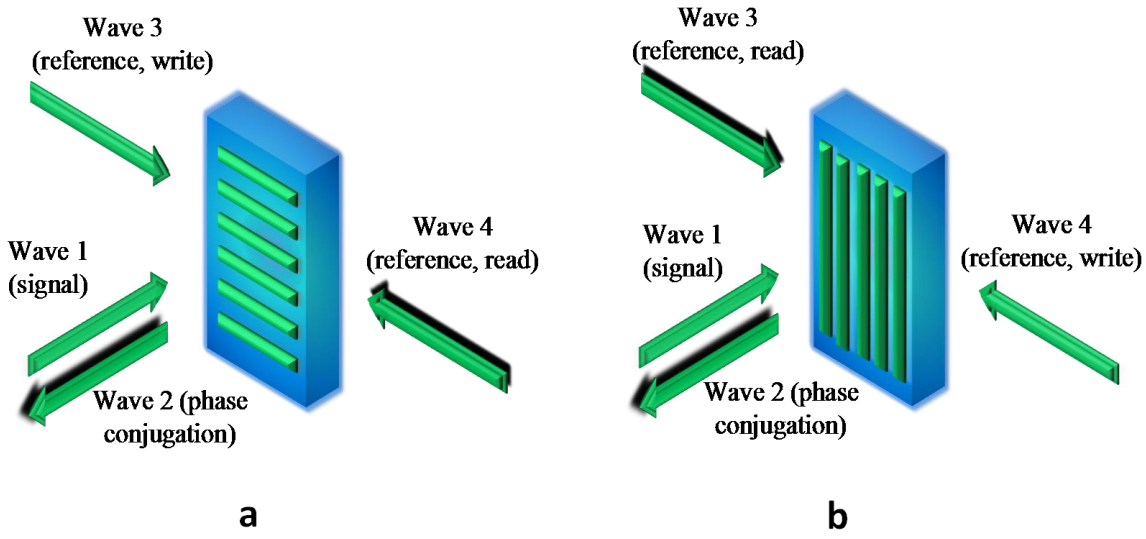

Figure 2.3 | Four-wave mixing in a nonlinear medium. A reference and object wave interfere and create a grating from which the second reference wave reflects and produces a conjugate wave. There are two possibilities corresponding to **a,** Transmission and **b**, Reflection gratings.

Assume that the two reference waves (denoted as waves 3 and 4) are counter-propagating plane waves. In Fig 2.3a, the signal wave 1 is added to the reference wave 3

and the intensity of their sum is recorded in the medium in the form of a volume grating (hologram). The reconstruction reference wave 4 is Bragg reflected from the grating to create the conjugate wave (wave 2). This grating is called the transmission grating.

The second possibility, illustrated in Fig. 2.3b, is for the reference wave 4 to interfere with the signal wave 1 and create a grating, called the reflection grating, from which the second reference wave 3 is reflected to create the conjugate wave 2. These two gratings can exist together but they usually have different efficiencies. For optimized diffraction efficiency, following experiments with FWM in PR polymer are performed with transmission grating geometry[56].

C. PR TWM Interferometer Theory and Experiments for UOT

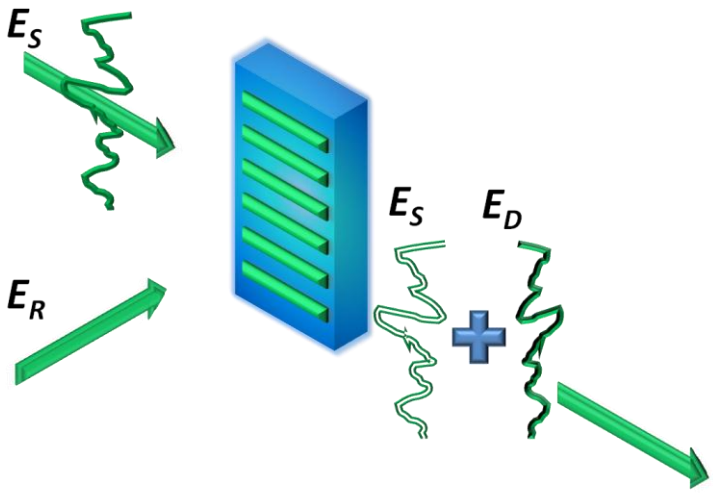

Figure 2.4 | Illustration of PR TWM interferometer. Es, signal beam; ER, reference beam; ED, diffracted beam.

1. Understanding Photorefractive TWM Interferometer for UOT (Fig. 2.4)

For a better understanding of PR TWM for UOT application, light intensity analytical expression on one point of photo detector is derived as:

$$I = \left[E_D + m\sum_i E_{S,i} \exp\left(jA_i \sin\left(\omega_a t + \phi_i\right)\right) + \left(1-m\right)E_S \right] \times \left[E_D + m\sum_i E_{S,i} \exp\left(jA_i \sin\left(\omega_a t + \phi_i\right)\right) + \left(1-m\right)E_S \right]^* \quad (2.2)$$

E_D is the diffracted light from pump through two wave mixing process. $E_{S,i}$ is the light amplitude for one specific photon path. $E_S = \sum_i E_{S,i}$, is total transmitted diffusive light on one specific point of photo detector. m is the probability of photon modulation. A_i is the phase amplitude caused by modulation of ultrasound. ω_a is the ultrasound frequency. ϕ_i is the random phase for the ultrasound interaction with photons. Here we also assume that the heterodyne efficiency is 1. This is true for pure photorefractive detection scheme, because the diffracted light matches the wavefront of the signal light. But it still remains unclear whether this assumption still holds in the situation where part of the photons are modulated by the ultrasound. We know that the speckle pattern will be changed because the ultrasound will change the phase of the transmitted photons. But let us go on with this assumption first.

$$
\begin{aligned}
I &= |E_D|^2 + (m-1)^2 |E_S|^2 + 2(1-m)\,\mathrm{Re}\left(E_D E_S^*\right) + \\
&2m(1-m)\,\mathrm{Re}\left(E_S^* \sum_i E_{S,i} \exp\left(jA_i \sin\left(\omega_a t + \phi_i\right)\right)\right) \\
&+2m\,\mathrm{Re}\left(E_D^* \sum_i E_{S,i} \exp\left(jA_i \sin\left(\omega_a t + \phi_i\right)\right)\right) \\
&+m^2 \left(\sum_i E_{S,i} \exp\left(jA_i \sin\left(\omega_a t + \phi_i\right)\right)\right)\left(\sum_i E_{S,i} \exp\left(jA_i \sin\left(\omega_a t + \phi_i\right)\right)\right)^*
\end{aligned}
\tag{2.3}
$$

For a robust approximation, magnitude order of *m* has to be considered. From reference[57], we know m ~ 2% for single coherence area (L/l_s >20, L sample thickness, l_s scattering length), and $m^2 \sim 0.0004 \ll 1$. Use the following relation when dealing with photorefractive gain medium: $E_D = \exp(-\alpha x/2)\left[\exp(\gamma x) - 1\right] E_s$; α, absorption coefficient in PR materials; γ, gain coefficient. This expression can be simplified as $E_D = \Gamma E_s, \Gamma = \exp(-\alpha x/2)\left[\exp(\gamma x) - 1\right]$ as in the work by de Montmorillon and Delaye[58]. Also assume that $\Gamma \gg$ m, we get

$$
I \approx |\Gamma E_S|^2 + 2(1-m)|E_S|^2\,\mathrm{Re}(\Gamma) + 2m\,\mathrm{Re}\left\{\Gamma^* E_S^* \sum_i E_{S,i} \exp\left[jA_i \sin\left(\omega_a t + \phi_i\right)\right]\right\}
\tag{2.4}
$$

Write the formula for scattered light without ultrasound modulation situation

$$
\begin{aligned}
I_0 &= \left[E_D + E_S\right]\left[E_D + E_S\right]^* \\
&= |E_D|^2 + |E_S|^2 + 2\,\mathrm{Re}\left(E_D E_S^*\right) \approx |E_D|^2 + 2\,\mathrm{Re}\left(E_D E_S^*\right) = |\Gamma E_S|^2 + 2|E_S|^2\,\mathrm{Re}(\Gamma)
\end{aligned}
\tag{2.5}
$$

Assume that Γ is real, which means that the PR TWM process is optimized and the wavefront of the diffracted beam and the signal beam totally match with each other.

But usually this is not the real situation. So if Γ is not real, then the heterodyne efficiency will be lower, since *Re(Γ) < abs(Γ)*.

$$I \approx \left|\Gamma E_S\right|^2 + 2\Gamma\left|E_S\right|^2 + 2m\Gamma\left[\mathrm{Re}\left\{E_S^* \sum_i E_{S,i} \exp\left[jA_i \sin\left(\omega_a t + \phi_i\right)\right]\right\} - \left|E_S\right|^2\right] \quad (2.6)$$

$$\begin{aligned}
&\exp\left[jA_i \sin\left(\omega_a t + \phi_i\right)\right] = \exp\left[-jA_i \cos\left(\omega_a t + \phi_i + \frac{\pi}{2}\right)\right] \\
&= \sum_{n=-\infty}^{\infty} J_n\left(-A_i\right) j^n \exp\left[jn\left(\omega_a t + \phi_i + \frac{\pi}{2}\right)\right] \\
&= \sum_{n=-\infty}^{\infty} J_n\left(-A_i\right) \exp\left[jn\left(\omega_a t + \phi_i + \pi\right)\right]
\end{aligned} \quad (2.7)$$

When n = 0, we have

$$\begin{aligned}
I_{DC} &\approx \left|\Gamma E_S\right|^2 + 2\Gamma\left|E_S\right|^2 + 2m\Gamma\left[\mathrm{Re}\left(E_S^* \sum_i J_0\left(A_i\right) E_{S,i}\right) - \left|E_S\right|^2\right] \\
&= \left|\Gamma E_S\right|^2 + 2\Gamma\left|E_S\right|^2 + 2m\Gamma\left[\mathrm{Re}\left(\sum_{i,j} J_0\left(A_{i,j}\right) E_{S,i}^* E_{S,j}\right) - \sum_{i,j} E_{S,i}^* E_{S,j}\right] \\
&= \left|\Gamma E_S\right|^2 + 2\Gamma\left|E_S\right|^2 + 2m\Gamma \times \mathrm{Re}\left\{\sum_{i,j}\left[J_0\left(A_{i,j}\right) - 1\right] E_{S,i}^* E_{S,j}\right\}
\end{aligned} \quad (2.8)$$

When $A_{i,j}$ is small (it is true when ultrasound pressure amplitude is small, so that small phase shift for modulated photons),

$$J_0\left(A_{i,j}\right) - 1 = -J_1^2\left(A_{i,j}\right) \approx -A_{i,j}^2 / 4 \quad (2.9)$$

$$I_{DC} \approx \left|\Gamma E_S\right|^2 + 2\Gamma\left|E_S\right|^2 - \frac{m\Gamma}{2} \times \mathrm{Re}\left(\sum_{i,j} A_{i,j}^2 E_{S,i}^* E_{S,j}\right) \quad (2.10)$$

Compared with Eq. (2.4), we find that

$$\Delta I_{DC} = -\frac{m\Gamma}{2} \times \mathrm{Re}\left(\sum_{i,j} A_{i,j}^2 E_{S,i}^* E_{S,j} \right) \tag{2.11}$$

Further simplify $A_{i,j}$ as a constant for different j, then integration over the whole photo detector surface area becomes straight forward.

$$\Delta I_{DC}^{total} = \int_{Sd} \Delta I_{DC} dS = -\frac{m\Gamma}{2} \int_{Sd} A^2 \left| E_S \right|^2 dS \tag{2.12}$$

We can find that at last we add the intensity not the electric field amplitude together. Because of this incoherent addition, the DC change is obvious. Certainly, the assumption of constant $A_{i,j}$ is not so necessary, but we can get more physics intuition from results based on this assumption.

When n = 1, we have

$$I_{+\omega_a} \approx 2m\Gamma \,\mathrm{Re}\left\{ E_S^* \sum_i E_{S,i} J_1\left(A_i\right) \exp\left[j\left(\omega_a t + \phi_i\right) \right] \right\} \tag{2.13}$$

When n = -1, we have

$$I_{-\omega_a} \approx 2m\Gamma \,\mathrm{Re}\left\{ E_S^* \sum_i E_{S,i} J_1\left(A_i\right) \exp\left[-j\left(\omega_a t + \phi_i\right) \right] \right\} \tag{2.14}$$

Obviously for the total AC component, we get

$$\begin{aligned} I_{AC} &\approx 4m\Gamma \,\mathrm{Re}\left(E_S^* \sum_i E_{S,i} J_1\left(A_i\right) \cos\left(\omega_a t + \phi_i\right) \right) \\ &= 4m\Gamma \,\mathrm{Re}\left(\sum_{i,j} E_{S,i}^* E_{S,j} J_1\left(A_{i,j}\right) \cos\left(\omega_a t + \phi_j\right) \right) \end{aligned} \tag{2.15}$$

Again, for simplicity, we assume that A_j and ϕ_j is constant for different j. Integrate over the whole detector area.

$$I_{AC}^{total} = \int_{Sd} I_{AC} dS = 4m\Gamma \int_{Sd} J_1(A)\cos(\omega_a t + \phi)\left|E_S\right|^2 dS \tag{2.16}$$

Since A and ϕ is function of the position, and ϕ can usually be thought of as evenly distributed from $0 \sim 2\pi$, (coming from Brownian motion and phase randomness between ultrasound field and photons), and follow the method by Kempe *et al*.[57]. We have

$$I_{AC}^{total} = S_d \langle I \rangle = 4m\Gamma S_d \langle J_1(A) \rangle \langle \cos(\omega_a t + \phi) \rangle \langle E_S^2 \rangle \tag{2.17}$$

$\langle \cos(\omega_a t + \phi) \rangle = \cos(\omega_a t + \phi')/\sqrt{N}$, N is the number of coherence area

In our experiment, large area detection approach is implemented and big N number is expected, which means I_{AC} is small. But we still detect the AC part for UOT signal with clear gel phantom (without any scattering emulsion) as shown in (Fig. 2.5). This phenomenon is justified considering the big coherence area (inside little scattering phantom) and so small N number.

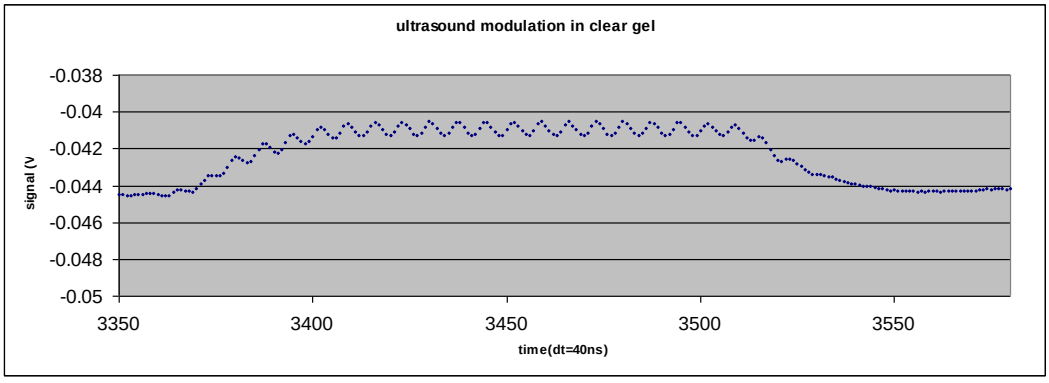

Figure 2.5 | PR TWM interferometer based UOT signal inside clear gel phantom to show the beating between "tagged" and "untagged" light.

One issue to mention is the confusion about energy conservation when the DC intensity changes. Basically where does the energy go when phase mismatch happens (because of the change of signal beam wavefront)? One possible explanation is as follows: Diffracted signal beam follows the sudden change of signal beam wavefront (even though the grating is static) and this change will induce (partial) phase match between pump beam and diffracted signal beam. So there must be an intensity increase in the direction of pump beam and amount of this increase should be equal to the decrease in the signal beam direction. More discussion can be found at the end of this chapter.

To complete the discussion for principles of PR TWM based UOT, tagged photon detection approach will be analyzed (assuming photorefractive response time is fast enough so that hologram built inside has been adapted to the wave-front change after ultrasound is applied):

To detect intensity change: $\Delta I_{DC} = |E_D|^2 = |\Gamma(mE_S)|^2$ (2.18)

For PR BSO crystal, Γ~2, modulation depth m~1%, then $\Delta I_{DC} \sim 0.0004|E_s|^2$. Compared with Eq. 2.12, $\Delta I_{DC} \sim -\frac{m\Gamma}{2}\int_{Sd} A^2 |E_S|^2 dS \sim 0.01|E_S|^2$

or for lock-in detection[46]

$$\Delta I_{DC} = |E_D + E_S|^2_{\phi=0} - |E_D + E_S|^2_{\phi=\pi} \sim 4m\Gamma|E_S|^2 \sim 0.08|E_S|^2 \quad (2.19)$$

This comparison tells us: a, direct detection of diffracted reference is not a reasonable detection method; b, TWM interferometer approach of “untagged photons”

and PR lock-in detection of "tagged photons" may have the same signal level. Then the question is which method is the better in practice. More knowledge about noise will be necessary to answer this question.

2. Shot Noise and "Black Background Detection"

The most fundamental source of noise is associated with the random arrivals of the photons themselves, which are usually described by Poisson statistics. Photocurrent is the quantity for real measurements. To begin with, We now examine the properties of the electric current *i(t)* induced in a circuit by a random photoelectron flux with mean $\eta\Phi$ (η quantum efficiency, Φ photon flux or photon numbers incident onto detector in unit time). Every photoelectron-hole pair generates a pulse of electric current with charge (area) e and time duration τ_p in the external circuit of the photodetector (Fig 2.6). A photon stream incident on a photo detector therefore results in a stream of current pulses which add together to constitute the photocurrent *i(t)*. The randomness of the photon stream is transformed into a fluctuating electric current. If the incident photons are Poisson distributed, these fluctuations are known as shot noise. More generally, for detectors with gain G, the generated charge in each pulse is $q = Ge$.

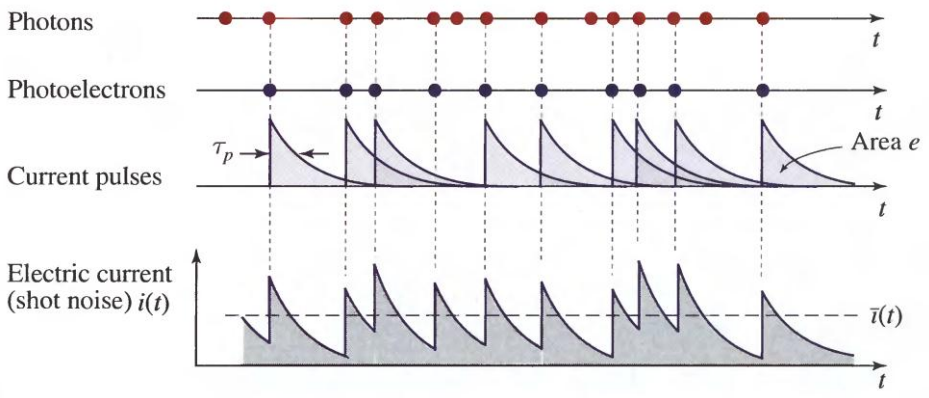

Figure 2.6 | The photocurrent induced in a photodetector circuit comprises a superposition of current pulses, each associated with a detected photon.

The individual pulses illustrated are exponentially decaying step functions but they can assume an arbitrary shape.

$$\bar{i} = e\eta\Phi$$
$$\sigma_i^2 = 2e\bar{i}B \qquad (2.20)$$
$$SNR = \frac{\bar{i}^2}{\sigma_i^2} = \frac{\eta\Phi}{2B}$$

Here $\bar{i}$ is photocurrent mean, σ_i^2 is photocurrent variance. B is defined as: Let the random number m of photoelectrons counted within a characteristic time interval T = 1/(2B) (the resolution time of the circuit) generate a photo current *i(t)*, where t is the instant of time immediately following the interval T.

For a specific detection system, i.e. arbitrary detection bandwidth, we will have more noise when averaged photocurrent begins to increase. This is the heart for black background detection, in which situation, signal stands on top of small background and there is less worry about shot noise from this small background. An immediate example in UOT may clarify this problem even better. A good estimation for total light ("tagged"

+ "untagged") that can be collected in UOT is around 10 nW. Consider $\sigma = \sqrt{2(h\upsilon)\bar{I}B}$, here σ is standard deviation for light intensity fluctuation; $h\upsilon$ is photon energy, for 532nm laser, around $4x10^{-19}$ J; B is the detection bandwidth, 1 MHz for example. So the light intensity fluctuation for 10nW laser is around 0.09nW, which is also around 1% of averaged intensity. For CW ultrasound modulation situation, the efficiency can be ~ 10%[59], then we have shot noise limited SNR of $(1\ nW/0.1\ nW)^2 \sim 100$. But for pulse ultrasound modulation situation, the efficiency is usually below 1%, then we will have shot noise limited SNR < 1, which is beyond detection limit. However, if we can block the un-tagged light, that is, $\bar{I}$ = tagged light intensity (only tagged photons, no other sources), smaller fluctuation of light intensity can be expected. Assuming the same conditions as mentioned above, for 0.1 nW tagged light, we have fluctuation of 0.009 nW, then SNR ~ 100. From this example, we have seen the obvious advantage of "black background detection" over "white background detection"

3. PR (BSO Crystal) TWM Interferometer Based UOT with Optical and Mechanical Contrasts

Based on photorefractive interferometer approach proposed by Murray group as mentioned in section 1 of this chapter, here we propose a PRC-based UOT system with a quasi-continuous-wave (CW) ultrasound-modulation scheme, where a 1 ms long focused ultrasound burst was applied to the tissue mimicking phantom and the time dependent change of the detected optical signal was recorded to image both the optical and the mechanical properties of the sample. The benefits of using a millisecond long ultrasound

burst are twofold: it improves the SNR, and also allows the detection of the effects of the acoustic radiation force, which happens on a millisecond time scale and can be related to the mechanical properties of the sample. Compared with the method reported by F. Ramaz *et al*[46] (the tagged photon detection approach) this technique takes advantage of the DC shift of the signal, which is associated with un-modulated light or "un-tagged photons". From the perspective of energy conservation, the decrease in the energy of the un-modulated light is equal to the increase of the energy in all modulated components[60,61]. Because of this broadband response, we have the opportunity to detect the low frequency components induced by the acoustic radiation force.

It is quite necessary to introduce briefly here about what is acoustic radiation force and its history of application for biological tissue imaging. Acoustic radiation force impulse imaging (ARFI)[62,63] is a developing method for imaging the elastic (one type of mechanical) properties of biological tissue. Though acoustic radiation force has been known for a century (see Torr's paper[64] for a good review), it has not been applied to the assessment of the properties of bio-materials until recently[65]. The quantum jump to real application of acoustic radiation force was the emergence of 'Ultrasound-Stimulated Vibro-Acoustic Spectrography'[66], where tissue responses to an oscillatory radiation force were produced by interference between frequency shifted focused beams of ultrasound. The first results of ARFI *in vivo* are presented by Nightingale *et al*.[63]. Compared with normal ultrasound imaging like, for example, B-mode, acoustic radiation force is particularly suitable for the noninvasive detection of hard tissue inclusions. The stiffness of soft tissues, however, is related to their composition and stiffness changes are

often related to pathology or therapy. Because ARFI uses high acoustic intensities within quite a short time span, unlike the continuous ultrasound in work by Fatemi and Greenleaf[66], there are no obvious increases of tissue temperature. Also, ARFI has the advantage of simple alignment because the same transducer is used for both pulse generation and pulse tracking.

Experimental setup (Fig. 2.7) will be described first then followed by results and discussion. The light from a Coherent Verdi laser (532 nm) was split into two paths: one (signal) for illuminating the sample and the other for pumping in TWM in PR material (BSO crystal in this experiment). The sample was insonified by a focusing ultrasonic transducer (Ultran Lab VHP 100-1-R38) with a central frequency of 1 MHz, focal length of 37.5 mm, focal zone length of 23 mm, and focal spot diameter of 2.2 mm. The peak acoustic pressure at the focus was 1.5 MPa. The high amplitude of the ultrasound burst was compensated by its low duty cycle (burst rate was 100 Hz) so that the ultrasound safety limit was still satisfied[67]. An alternating electric field (1 kHz, 4 kV) was applied to the BSO crystal to enhance the TWM gain. The pump light intensity incident on the BSO was kept around 10mW/cm^2. Under this condition, we measured that the crystal response time was at least 100 ms, which was comparable with the speckle decorrelation time of 2cm *ex vivo* chicken breast tissue[38]. The system was enclosed in an acrylic enclosure to prevent the real-time holography from undergoing perturbations.

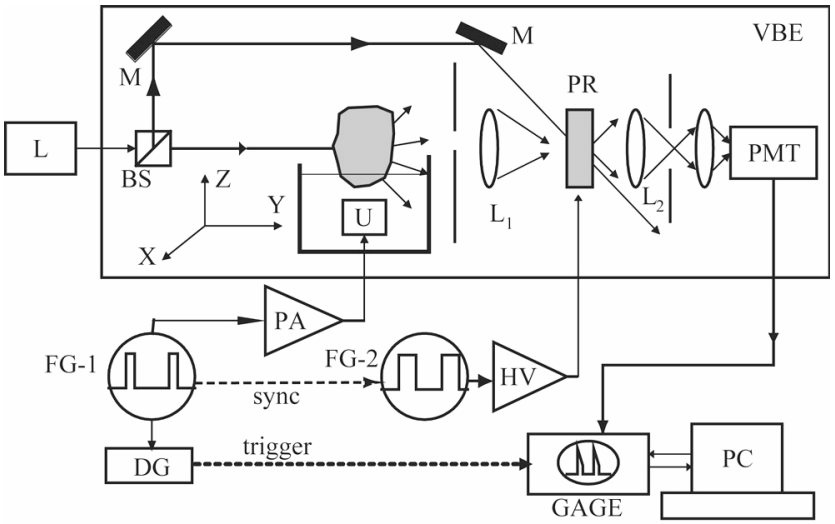

Figure 2.7 | Schematic of the experiment setup: L, laser; BS, beam splitter; M, mirror; L1, L2, lens; PR, photorefractive crystal BSO; PMT, photomultiplier; FG-1, FG-2, function generators; PA, power amplifier; DG, pulse-delay generator; HV, high voltage amplifier; PC, personal computer; U, 1 MHz ultrasound transducer; T, study sample; VBE, vibration block enclosure; GAGE, CompuScope 14200 14 bit waveform digitizer.

A longer ultrasound burst should give us more opportunity to observe the acoustic radiation force effect, which happens on the time order of a millisecond[63]. To verify this expectation, we buried a plastic bead, as shown in (Fig. 2.7), inside the phantom. When the ultrasound beam was not incident on, or around, the plastic bead, the signal (line A in Fig. 2.8) did not show any difference from the ordinary situation. But when the ultrasound beam was incident on, or around, the plastic bead, the signal (line B in (Fig. 2.8)) was broadened and significantly increased. The time duration of the signal in line A corresponded to the ultrasound burst length. This indicates that we can still observe the signal for line B even after the ultrasound was turned off. One straightforward reasoning of this phenomenon is that photons have been modulated by the acoustic radiation force, which is caused by the transfer of acoustic wave

momentum[64], and it takes time for this momentum transfer to accumulate and also to die down. This delay in time domain enables us to separate the ultrasound radiation force signal from normal UOT signal. Information about optical (absorption) properties can be obtained by averaging the output signal during the time when ultrasound is turned on. On the other hand, information about mechanical stiffness can be obtained from averaging or accumulating the output signal after the ultrasound is off within tens of milliseconds. In this way, we get two-dimensional (2D) images as shown in (Fig. 2.9). There is not much optical contrast between the plastic bead and background so (Fig. 2.9a) does not show any obvious image. However, we do find a clear image for the plastic bead in (Fig. 2.9b). Here the plastic bead has a big acoustic impedance mismatch with the background phantom. When the ultrasound is incident on, or around, the plastic bead, a large momentum transfer occurs because of the impedance mismatch. The acoustic radiation force tries to push the particles from their original positions and these moving particles modulate the photons passing through.

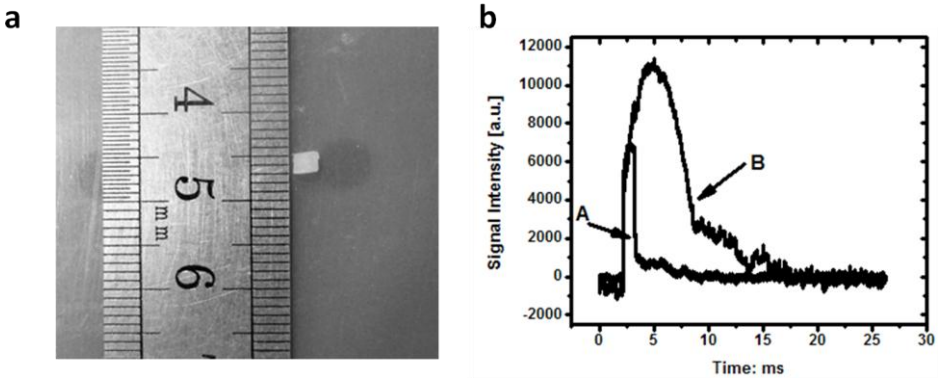

Figure 2.8 | Mechanical contrast in UOT. **a**, Plastic bead, which is buried in a phantom as the imaging object. **b**, Signal intensity when ultrasound is incident or not on the plastic bead.

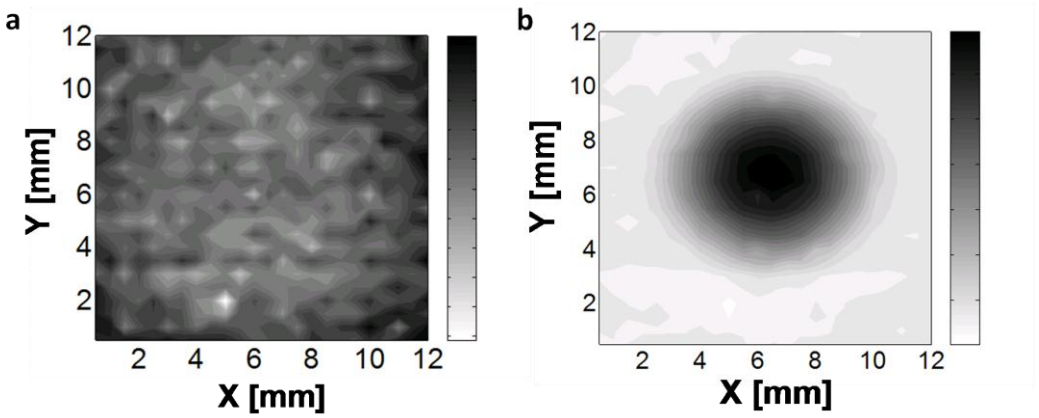

Figure 2.9 | UOT of plastic bead buried inside tissue phantom. **a**, Optical information weighted 2D image. **b**, Mechanical information weighted 2D image.

Another experiment was also performed to demonstrate imaging based on mechanical properties, rather than optical properties. This time, a phantom sample was prepared with 10% porcine gelatin and 1% Intralipid concentration, resulting in a reduced scattering coefficient μ_s'=10 cm^{-1}, and 10cm×4cm×10 cm ($X \times Y \times Z$) outer dimensions. The buried objects are two 6 mm cubic volumes enhanced with 20% corn starch with a 12 mm separation. The two inclusions had minimal differences in optical properties but a higher mechanical contrast than the background. As a result, the inclusions were barely discernible on the UOT image acquired 0.1 ms after the onset of the ultrasound burst (Fig. 2.10, upper plot) but were markedly visible on the image acquired 0.1 ms after the passage of the ultrasound burst, or expressed in another manner, 1.1ms after the start of ultrasound burst (Fig. 2.10, lower plot), because the mechanical property differences gave rise to the acoustic radiation force effect that happened on a time scale of several milliseconds.[62]

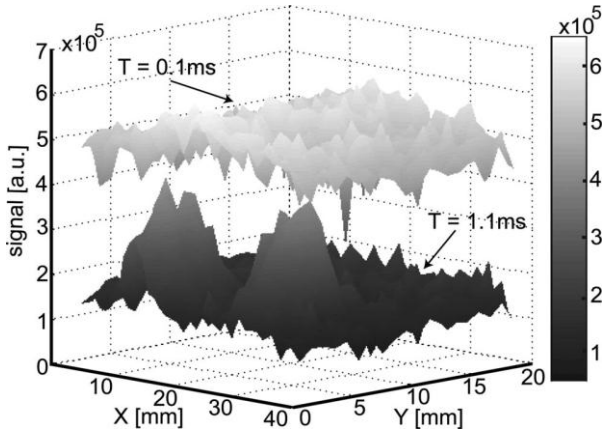

Figure 2.10 | UOT surface maps of two buried cubic volumes enhanced with corn starch. Date were taken at T=0.1 ms and 1.1 ms after the start of a 1 ms long ultrasound burst.

We next demonstrate UOT imaging based on both optical and mechanical properties by imaging two segments of nude mouse tail, with 3mm×10mm (diameter × *Z*) in dimension and 8 mm separation, embedded in a gelatin sample with the same composition and outer dimension as previous mentioned sample. The UOT image (Fig. 2.11b) acquired at *T*=0.1 ms after the onset of the ultrasound was based mainly on optical absorption contrast. Owing to the higher absorption of the mouse tails, they appear dark, but the contrast is low. The image quality is much better for ultrasound light modulation produced by the radiation force effect, because of the large acoustic impedance mismatch between the bone structures of the nude mouse tail and the background gelatin phantom. This is shown in (Fig. 2.11c), where the image was acquired 0.1 ms after the end of the 1 ms ultrasound. Here the mouse tails appear bright owing to strong acoustic modulation. The 1D scans (Fig. 2.11a) across the sample at the

two different times show the different effects of optical and mechanical contrasts on the UOT signal. Details of the mechanical properties of the object, such as the acoustic impedance mismatch, can be characterized from the time-evolution curves of the UOT signal. To demonstrate this, a comparison of time-evolution curves from the nude mouse tail, the corn starch inclusion, and their background gelatin phantoms are shown in (Fig. 2.11d). For the nude mouse tail, the radiation force effect kept increasing long after the ultrasound was turned off, while for the corn starch inclusion it started decay 0.5 ms after the end of the ultrasound burst. For both samples the background gelatin curves showed little radiation force effect, as expected. Separation of the sample's mechanical and optical contrast is possible once the acoustic impedance can be derived from the time-resolved UOT imaging.

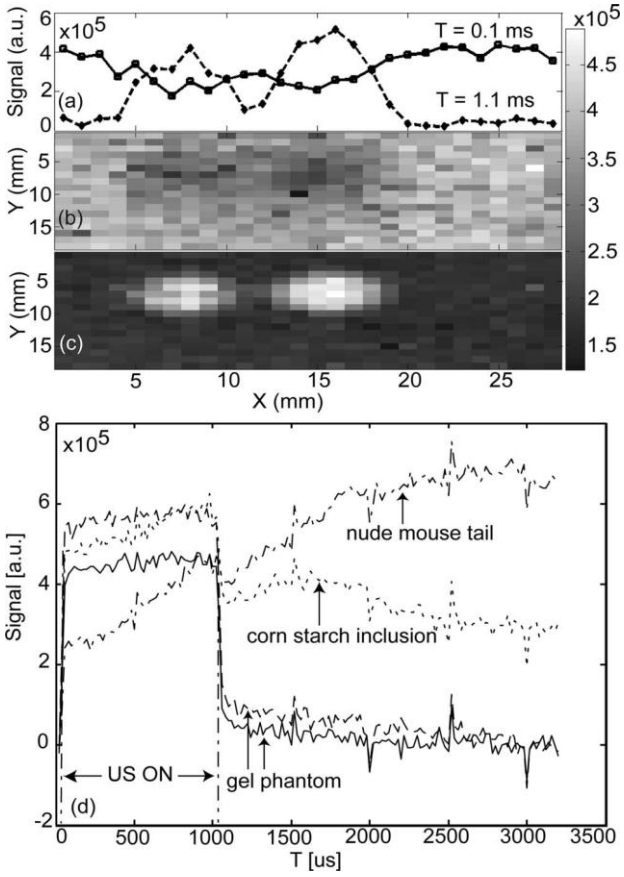

Figure 2.11 | UOT for optical and mechanical contrast separation in time domain. **a**, 1D scan at y=7 mm. 2D density map at **b**, T=0.1 ms and **c**, T=1.1 ms. **d**, Comparison of time-resolved UOT signal for various objects.

D. FWM in PR Polymer UOT and Scatter Noise Reduction Method

1. Introduction to PR FWM Based UOT

From discussion above, we know that PR TWM interferometer method can give us both optical and mechanical properties at the same time, but UOT SNR is still not satisfactory and more efforts will be necessary for real applications. PR TWM with "black background detection" developed by Ramaz *et al.*[46], has partly solved the problem of background noise by making use of diffracted light only for "tagged

photons", but unmodulated light is still mixed with modulated light in signal beam direction. The part of diffusive light modulated by localized ultrasound inside the medium is overwhelmed by un-modulated, background diffuse light. For example in work by Wang and Zhao[59], the dc value (background) is 30 times larger than ac amplitude (signal), so that a lot of averaging is needed to improve the SNR for imaging purpose. Therefore filtering out the background is extremely necessary for further improvement of UOT modality.

By use of the four-wave mixing (FWM) frequency filtering technique, it is possible to remove the "untagged photons" and extract out only the "tagged photons". As mentioned previously, FWM is implemented to generate phase conjugation waves. In this method, a nonlinear medium is pumped by a pair of counter-propagating laser beams with the same optical frequency. When a signal beam is incident into the medium, a fourth beam is generated. The fourth beam is propagating opposite to the signal beam and is a time-reversed replica of the signal beam. When the PR polymer is illuminated with a monochromatic reference wave, for example, $A_1(\omega)$ and a polychromatic signal wave $A_2 = A_2(\omega) + A_2'(\omega') + A_2''(\omega'') + \ldots$, only the component $A_2(\omega)$ will contribute to the formation of stable fringes. The components of A_2 whose frequency differs from ω will produce fringes having a rate of travel which is too high for the material to respond to. The counter-propagating laser beam (probe beam) only reads out the component $A_2(\omega)$.

Though FWM for frequency filtering purpose in diffuse media looks straight-forward, this approach has never been demonstrated yet for UOT. A similar method with

low frequency vibration, instead of high frequency ultrasound modulation, has been studied by Khoury *et al* [68] but by making use of un-modulated light. However this method only applies to weakly scattering media such as diluted milk-water solution. A related FWM technique, laser-based ultrasound for defect detection which involves reflection from vibrating surface[69], has been used to improve SNR by reducing bandwidth of the measurement compared with the time-domain method (for example TWM in ref [21]). Considering the low SNR feature in UOT, FWM is quite a promising method for real application, because only ultrasound modulated signal photons will be collected in the form of phase conjugation light.

One difficulty we contend with is to find proper PR materials which have the proper phase conjugate reflectivity (defined as the ratio between the phase conjugate light and incoming signal light) and fast response time to catch the speed of speckle de-correlation. PR polymers represent a relatively new class of PR materials. These devices can offer very high internal diffraction efficiencies and have been demonstrated to exhibit response time on the order of milliseconds[56]. Furthermore, the fabrication procedures for these devices are significantly simpler than for PR crystals and can be done at low cost in a small-scale chemical laboratory.

2. PR FWM Based UOT Experiments

Experimental setup for FWM is sketched in (Fig. 2.12). Light from a 90-mW frequency-doubled Nd:YAG laser source was sent to a variable beam splitter, which was composed of a half wave plate and a polarizing beam splitter. The imaging was

performed in a degenerate forward FWM geometry with the two writing beams (Fig. 2.12), that is reference and signal light beam subtending an angle around 40° and interfering in the polymer to generate a hologram by the PR process. The polymer sample was tilted around 50° with respect to the bisector of the two writing beams and was subject to an applied voltage of 7.5 kV. The hologram was read out by the probe beam, which was counter-propagating with the reference beam. To optimize the reflectivity of phase conjugation, both writing and reading beams were *p* polarized. Our phase conjugate detection system employed a PR polymer (from Nitto Denko Technical) with 100 um in thickness. In this experiment, the polymer composition was TPD:CBz:DCST 5:5:1 copolymer 50/FDCST 30/ECz 20. Under our experimental conditions, the response time of the PR polymer was approximately 300 ms. The phase conjugate signal of modulated scattered light (tagged photons) was collected by lenses 1 and 2, and fed in to a photodiode. The sound source was a spherically focused piezoelectric transducer (Ultran Lab VHP100-1-R38), with a 37.5-mm focal length and a center frequency of 1 MHz. The ultrasonic axis was perpendicular to the phantom illumination direction.

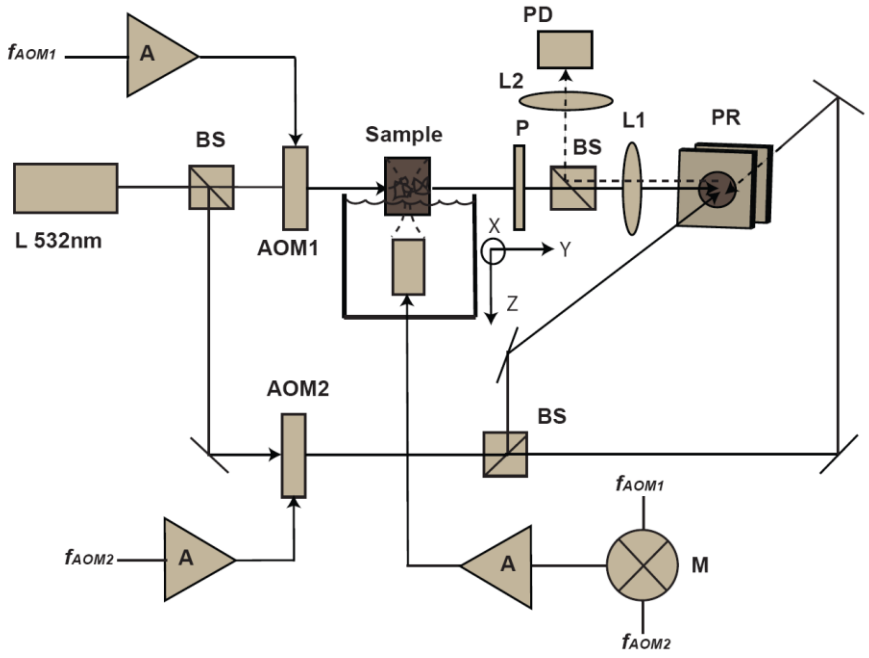

Figure 2.12 | Schematic of the experimental setup: BS, beam-splitter; AOM, acoustic-optics modulator; L1, L2 lens; PD, photo-diode; P, polarizer; PR polymer, photorefractive polymer; A, power amplifier; M frequency mixer.

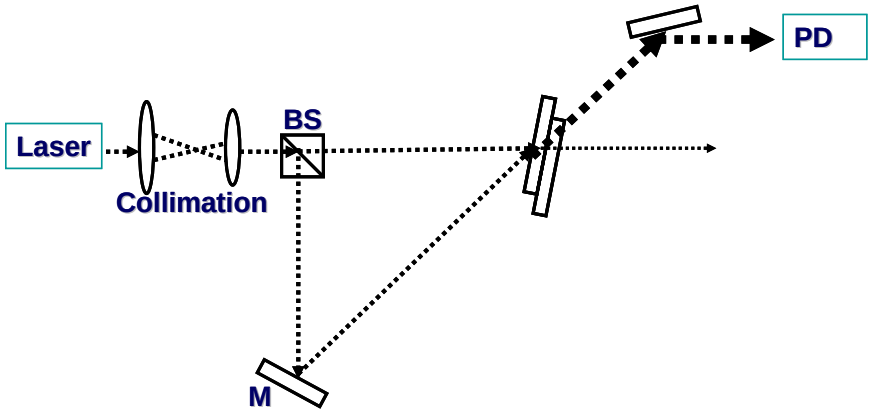

Figure 2.13 | Schematic of the TWM experimental setup: BS, beam-splitter; PD, photo-diode.

To clarify the issue of angle acceptance, we designed an experiment with two wave mixing (TWM) arrangement, which helped us to observe the PR TWM gain change along with the angle difference. Setup is shown in as (Fig. 2.13). Light from laser is splitted into two parts: one part woks as the pump, the other works as the probe. Through TWM coupling effect, the energy of the pump will be transferred to the probe beam. We call the ratio between amplifier probe intensity to original probe intensity as the gain. The gain change reflects the angle acceptance (limited by photorefractive effect) of the material. We recorded the data and plotted the relationship as shown in (Fig. 2.14). From this figure, it is confirmed that our material has angle acceptance as big as ~50 degrees. This value is usually much better than photorefractive crystals in the condition of the same response time. Fig. 2.15 shows the signal intensity changes when ultrasound (with peak pressure around 0.7 MPa) is turned on and turned off. When ultrasound is off, no phase conjugate signal can be collected because the frequency of reference beams is different from that of signal beams, although there is still some residual light coming from scattering of the two reference beams. When ultrasound is turned on, a small component of the signal beam has the same frequency as the reference beam and phase conjugate light is generated. Because it takes time (PR response time) to write the holograph, the phase conjugation light increases gradually at first. After hundreds of milliseconds, the signal begins to saturate, then UOT signal can be collected. The typical ratio between phase conjugation signal and background noise is around 1. Compared with heterodyne method[59] and TWM interferometer method[46], this approach has the obvious advantage of dark background noise (at least one order of magnitude better). In

our case, the reflectivity can be close to or even a little more than unity. With a higher reflectivity polymer, better signal to background ratio could be achieved.

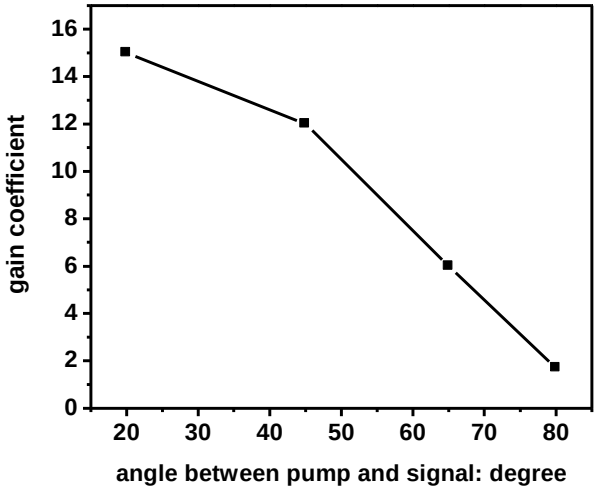

Figure 2.14 | Relationship between TWM gain coefficient and suspension angle.

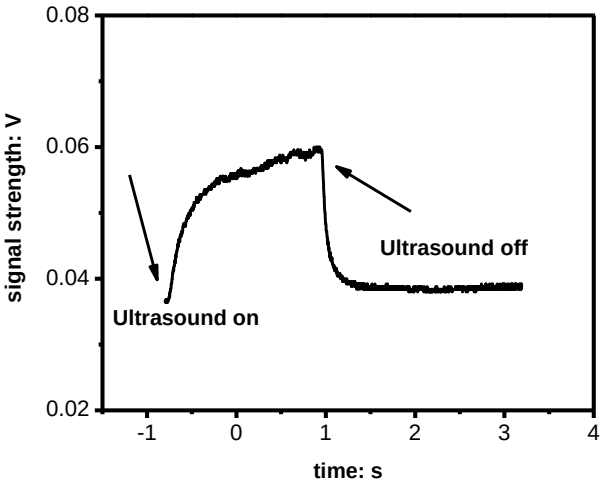

Figure 2.15 | Typical signal for PR FWM based UOT.

A one dimension scan was performed (Fig. 2.16a) to demonstrate the ability of FWM technique to detect a buried optical inhomogeneity (based on optical absorption). The tissue phantom consist of 10% porcine gelatin and 1% Intralipid concentration, resulting in a reduced scattering coefficient $\mu_s' = 10\ cm^{-1}$. The outside dimension of the phantom sample was 6 cm×6 cm×1.5 cm and the phantom was oriented such that the laser passed through the 1.5-cm thickness. One 0.2-cm thick (in the light propagation direction) Trypan-blue dyed object was buried in the phantom. In the scan direction, the objects are 0.3-cm wide. The phantom was scanned in 0.5-mm steps perpendicular to the light-propagation direction and the ultrasound propagation direction. In another experiment, tissue phantom consist of 10% porcine gelatin and 0.6% Intralipid concentration, resulting in a reduced scattering coefficient $\mu_s' = 6\ cm^{-1}$. The outside dimension of the phantom sample was 6 cm×6 cm×2 cm and the phantom was oriented such that the laser passed through the 2-cm thickness. Two 0.3-cm thick (in the light propagation direction) Trypan-blue dyed objects were buried in the phantom. In the scan direction, the two objects are 0.4-cm wide and around 0.5-cm separated, as shown in (Fig. 2.16b). To achieve steady state for data collection, we took data after several seconds waiting time. In this case, we used low pass filter (25 Hz cut off frequency) to smooth out the high frequency noise.

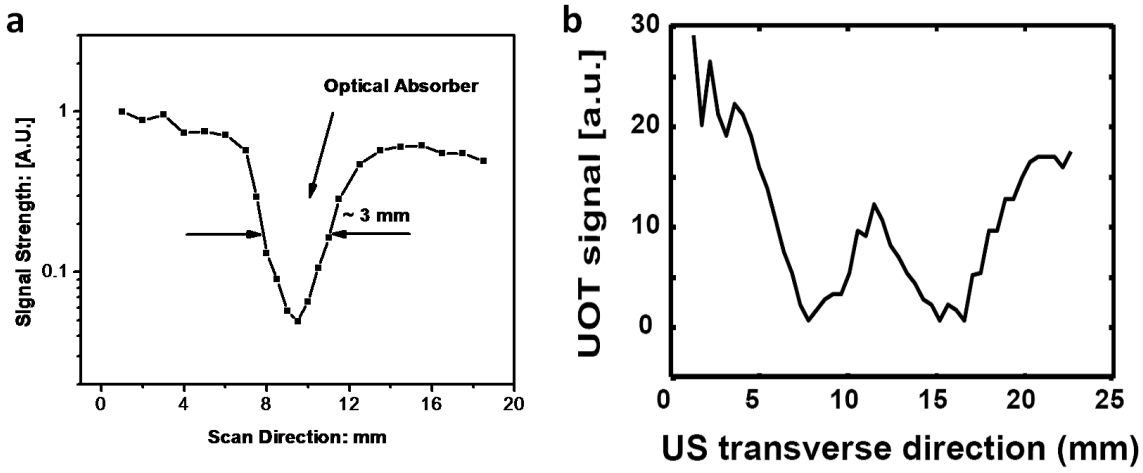

Figure 2.16 | FWM based UOT 1D image. **a**, Signal observed as the transducer is scanned across the tissue mimicking phantom, one optical absorber is buried inside. **b**, two optical absorbers buried.

SNR issue is the greatest challenge for UOT (actually also the most critical problem for almost all the imaging techniques). To increase SNR, we can either improve signal strength or decrease background (un-modulated photons) noise. For the point view of FWM, it has the obvious advantage of low background noise level. Again assume total UOT signal can be collected is 10nW, modulation depth is 1%. After FWM filtering, 0.1 nW signal and 0.1 nW background noise is left. For this amount of light, we have signal fluctuation (from shot noise, and assume 1 MHz detection bandwidth. Certainly we need fast PR response for this purpose) of 0.01 nW, which corresponds to shot noise limited SNR of 100. This is 100 times better than TWM situation. To further improve the SNR, one possible approach is to use PR materials with better performance. We had the experience of much better FWM reflectivity (~400%), for He-Ne (632 nm) laser. The sensitizer of the polymer is C60. Also it is better to use longer wavelength

laser for deeper penetration in biological tissues[6,70] The difficulty here is to get the proper red or near infrared laser which can supply enough optical power for imaging purpose. More research with this method is still under investigation.

Another difficulty dealing with PR materials comes from beam fanning. Beam fanning is an amplified scattering effect that occurs in high-gain PR materials (both in inorganic crystals and organic polymers). Fanning manifests itself through an intensity loss as a single beam is transmitted through a sample with an electric field applied. Fanning is in a random direction because of its scattering nature. This will hurt our signal collection, because both the phase conjugation light and beam fanning are on the same order of magnitude. It was found that to minimize the beam fanning, a negative high voltage has to be applied to the sample electrode at which the writing beams are incident[71].Also, reducing the beam diameter helps to minimize beam fanning[72] However, at higher electric fields, even these measures are not sufficient to suppress the fanning[56] In our case, usually we use voltage across the polymer for around 7~8 kV. For 100 μm thickness polymer, the electrical field is around 80 V/μm, which is close to limit of the materials.

3. Scatter Noise Suppression Cascaded with FWM UOT

To solve the problem of pump scatter noise including beam fanning, mixed with FWM UOT signal, a hybrid, cascaded technique was tested to suppress this noise. Pump noise from FWM setup is static light while the UOT signal intensity keeps changing during the scanning procedure when ultrasound is turned on/off. Optical novelty filters [73]

have been developed to extract dynamic signal from static noise. The idea is to make use of optical novelty filter for the purpose of getting rid of static noise (pump scatter) while still keeping the dynamic signal (UOT signal) transmitted through for detection. In photorefractive two wave mixing (or two-beam coupling) approach for optical novelty filter[74,75], a weak signal is mixed with a relatively strong pump and the photorefractive material is oriented so that the grating written by the interference of these two beams results in energy transfer from the signal beam to the pump beam, yielding a strongly deamplified signal. More specifically, for the steady-state or unvarying input condition, the signal will suffer nearly complete deamplification owing to destructive interference. This phenomenon occurs because the optical field diffracted by the hologram from the pump into the direction of the signal beam is 180° out of phase with the directly transmitted signal beam. However in the situation of varying input signal, the diffracted pump beam lags behind the transmitted signal by the photorefractive response time T of the material used, that is, optical novel signal will go through the material undisturbed. In principle, contrast ratio C ($\equiv \frac{I_{novel}}{I_{static}}$) could be as high as two-wave mixing gain ($e^{\Gamma l}$). Realistically, the reported value of C is 20~50[74,76] even in high gain material such as $BaTiO_3$. However, in more recent report[77], much better performance has been achieved to deamplify the static beam, which has been suppressed by 70 dB. It is worth noting that carrier or static signal suppression has to be optimized only in quite strict experimental conditions, such as perfect polarization, specific intensity ratio between

carrier, modulation and pump, specific angle between pump and signal and *etc*. These conditions work as guidelines for following experiment.

As illustrated in (Fig. 2.17), phase conjugate of UOT signal is immersed in scatter noise from Pump1 and probe beams. TWM optical novelty filter has been set up to remove this static scatter noise. A Ce:$BaTiO_3$[78] crystal (7.73×7.04×4.8 mm, Photox. Opt. Sys.) was used in this experiment and its c-axis (energy transfer direction) was aligned to take away the energy from mixed signal beam. Sheet polarizer between collection lens and $BaTiO_3$ was added to select the *p* polarization, which favors $BaTiO_3$ coupling efficiency. Pump2 and signal beams intersected at around 40 degrees. This intersection angle was a rough estimation because the collected scattered light extended to 15°~20°.

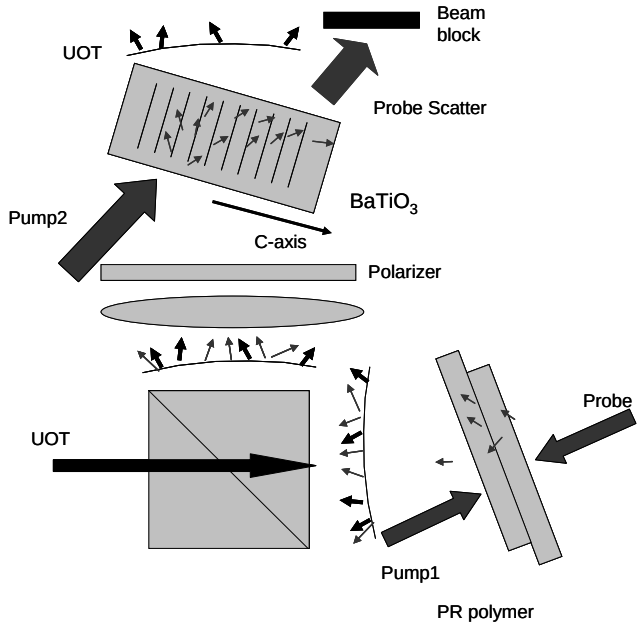

Figure 2.17 | Optical novelty filter for scatter noise suppression. Bold dark color small arrows represent diffuse tagged photons, whereas the regular size light color small arrows represent un-tagged photons. After optical novelty filter (BaTiO3 in our experiment), only tagged photons (bold small arrows) are left.

Approximately 2 μW diffusive light can be collected from ground glass then into FWM system. Phase conjugate signal went to 50/50 beam splitter, lens and polarizer. At last approximately half μW could be incident onto $BaTiO_3$ for optical novelty filtering. This amount of light was close to the real situation for UOT experiments. Because of the absorption of $BaTiO_3$, 170 nW went through the crystal with pump2 closed. In this situation, AOM1 shifted to 81 MHz and 1 MHz frequency mismatch occurred between signal beam and both pump beams. 60 nW scattered light remained, i.e. signal to background ratio (or contrast ratio C) is around 3:1. With pump2 (5 mW) turned on, in previously mentioned two conditions, we got 60 nW and 3 nW respectively, that is 20:1 signal to background ratio, one order of magnitude higher than results in simple FWM approach. Though this filtering efficiency is the way lower than the reported performance in [77], it still could be considered a significant improvement in signal to background ratio for UOT application and more efforts are being explored with this method. High gain and bigger angular bandwidth materials for novelty filtering are still being searched. Polymeric materials could be a good candidate [79-81].

4. More on Optical Novelty Filter

One possibility to make use of the PR optical novelty filter is to orient UOT signal beam in the direction where the energy will be taken away into pump beam direction, that is an obtuse angle (bigger than 90°) between signal beam and *c*-axis. When ultrasound is suddenly turned on, the dynamic part of signal will be transmitted through and kept in its original direction instead of diffraction into pump beam. For the

point of view of energy conservation, there will be equal amount of intensity decrease in the pump beam arm, because of less diffraction from signal beam. In principle, the method is an even better one because of its inherent “black background detection”. In practice, performance is limited by available contrast ratio and, again, pump scattering noise. Tentative experiments have been performed with BSO crystal, but more systematic work will be necessary to prove its advantage.

PR interferometer can also be considered as an optical novelty filter in some sense. In that situation, the angle between signal beam and *c*-axis is acute (smaller than 90°), so that energy is transferred from pump to signal. When ultrasound is suddenly turned on, the dynamic part of signal will be diffracted toward pump beam direction, because of the phase conditions between static grating and dynamic signal beam, which otherwise will support signal beam diffracted into its own direction. Or on the other hand, before ultrasound is turned on, signal and diffracted pump beams have the same wavefront or phase match between each other. After ultrasound modulation begins, phase matching condition breaks down and destructive interference between dynamic part of signal and diffracted pump happens. Intensity decreases in signal beam direction and at the same time, equal amount of intensity increase will happen in pump direction to obey the law of energy conservation.

CHAPTER III

RARE-EARTH-ION-DOPED INORGANIC CRYSTALS FOR SPECTRAL-HOLE BURNING (SHB) BASED UOT

In this chapter, we introduce the central features of rare-earth-ion doped crystals from SHB application point of view. The main goal is to establish and motivate the simple model of the system which we will use in the following chapters. Rare-earth ions, embedded in a variety of solid state host materials, are the central part of many active optical applications, including laser crystals[82], amplifying waveguides in glasses[83], polymers[84] and so on. Common to these applications is the fact that the optical properties are very well described by a frozen-gas model, in which the optical properties are ascribed to the individual rare-earth ions, which behave almost as free ions, and are only mildly perturbed by the field of the host material[85].

To motivate the frozen gas model, we will in the first section of this chapter study the electron structure of the rare-earth elements (with a review of quantum numbers in chemistry): Inside the chemically active *6s* and *5d* electrons, the rare-earths have a full $5s^2 5p^6$ shell shielding a partially filled *4f*-subshell. The rich optical spectrum of the rare-earth ions can be attributed to transitions between different $4f^n$ states, and the second section discusses how these states are influenced by the crystal field, both with respect to inhomogeneous effects, in particular inhomogeneous broadening, which are constant in time but differ between ions, and with respect to homogeneous effects: line broadening and decoherence mechanisms affecting all ions equally.

In the last two sections of the chapter, we will give a review of material properties of Tm:YAG and Pr:YSO. Information listed there will be the basics for SHB based UOT, not only theoretical analysis foundation, but also an experiment guideline.

A. Rare-Earth-Ion Chemical Properties

1. Quantum Numbers

To completely describe an electron in an atom, four quantum numbers are needed, these are conventionally known as:

a. Principle Quantum Number, **n**: 1, 2, 3, 4, 5, 6 .... This number therefore has a dependence only on the distance between the electron and the nucleus (i.e., the radial coordinate, **r**).. The average distance increases with **n**, and hence quantum states with different principal quantum numbers are said to belong to different shells: K, L, M, N, O, P ... . Corresponding energy is $E_n = \frac{E_1}{n^2} = \frac{-13.6eV}{n^2}, n = 1, 2, 3, \ldots .$

b. The azimuthal quantum number ($\ell = 0, 1 \ldots n-1$) (also known as the angular quantum number or orbital quantum number) gives the orbital angular momentum through the relation: $L^2 = \hbar^2 \ell(\ell+1)$. In chemistry, this quantum number is very important, since it specifies the shape of an atomic orbital and strongly influences chemical bonds and bond angles. Orbital quantum number, (ℓ: 0 1 2 3 4 5 ...) corresponds to Subshell: (*s, p, d, f, g, h* ...). Max. electrons in every subshell is $2(2\ell+1)$: 2 6 10 14 18 22 ...

c. The magnetic quantum number $\left(m_\ell = -\ell, -\ell+1, ..., 0, ..., \ell-1, \ell\right)$ is the eigenvalue, $L_z = m_\ell \hbar$. This is the projection of the orbital angular momentum along a specified axis.

d. The spin projection quantum number (m_s = −1/2 or +1/2), is the intrinsic angular momentum of the electron. This is the projection of the spin s=1/2 along the specified axis.

However, when one takes the spin-orbit interaction into consideration, also consider the situation of multiple electrons (in most situation for rare earth doped ions), we will have

$$\boldsymbol{L} = \sum_{i=1}^{n} \boldsymbol{l}_i \text{ and } \boldsymbol{S} = \sum_{i=1}^{n} \boldsymbol{s}_i \tag{3.1}$$

They are the total orbit and total spin momentum operators respectively, and

$$\boldsymbol{J} = \boldsymbol{L} + \boldsymbol{S}, \tag{3.2}$$

is the total angular momentum operator which has 2*J*+1 eigenstates represented by the magnetic quantum number *M = -J, -J+1, ..., 0, ... J-1, J*

In the *LS* coupling scheme, the electronic states of an RE ion may be specified completely by writing the basis states as

$$\boldsymbol{\Psi} = \left| nl\tau LSJM \right\rangle \tag{3.3}$$

where *nl,* which is *4f*, or *5d* for RE ions, represents the radial part of the basis states. Usually, the symbol ${}^{2S+1}L_J$ is used for naming a free ion state or multiplet. Whereas *S* and *J* are specified with numbers (0, 1/2, 1, …), *L* is traditionally specified with letters *S, P, D, F, G, H,* ... respectively, for L = 0, 1, 2, 3, 4, 5, ….

For example, for Pr^{3+} ions, there are two *4f* electrons so written as $4f^2$. In this situation, we have $S = 1$. The interesting level is H, that is L = 5. Then the corresponding *J* manifold can be expressed as $^3H_4$ or $^3H_6$. More importantly, $^3H_4$ is the ground state and its $J= L-S =4$

2. Rare-Earth-Ion Chemistry

The rare-earth elements, also known as the Lanthanides, are characterized by a partially filled 4*f* subshell inside filled 5*s* and 5*p* subshells: During the iterative construction (aufbau) of the periodic table, see (Fig. 3.1) for the relevant part, the strong spin-orbit coupling of the 4*f* electrons makes it energetically favorable to defer the filling of the 4*f* subshell until the 6*s*, 5*s* and 5*p* subshells, with lower spin orbit coupling energies, have been filled[86]. As illustrated by (Fig. 3.2) the 4*f* orbitals are spatially located within the 5*s* and 5*p* orbitals, a fact which is vividly illustrated by an effect known as the Lanthanide contraction: due to the increased screening of the core as the 4*f* shell is gradually filled, the diameter of the Lanthanide atoms, which is defined by the filled 5*s*, *p* subshells, decreases through the Lanthanide series. Here, we will only consider the case of trivalent rare-earth ions (such as Pr^{3+} and Tm^{3+}) embedded in mono-crystalline inorganic crystals, substituting for chemically similar ions such as Yttrium (but in Tm:YAG, Tm^{3+} replaces Y or Lu). Typical doping levels will be on the order of 0.01~1% of the possible substitution sites being populated by rare-earth ions, so that the host crystal structure is only mildly perturbed. Electronic configurations of Pr and Tm are illustrated in Fig. 3.3a and Fig. 3.3b respectively.

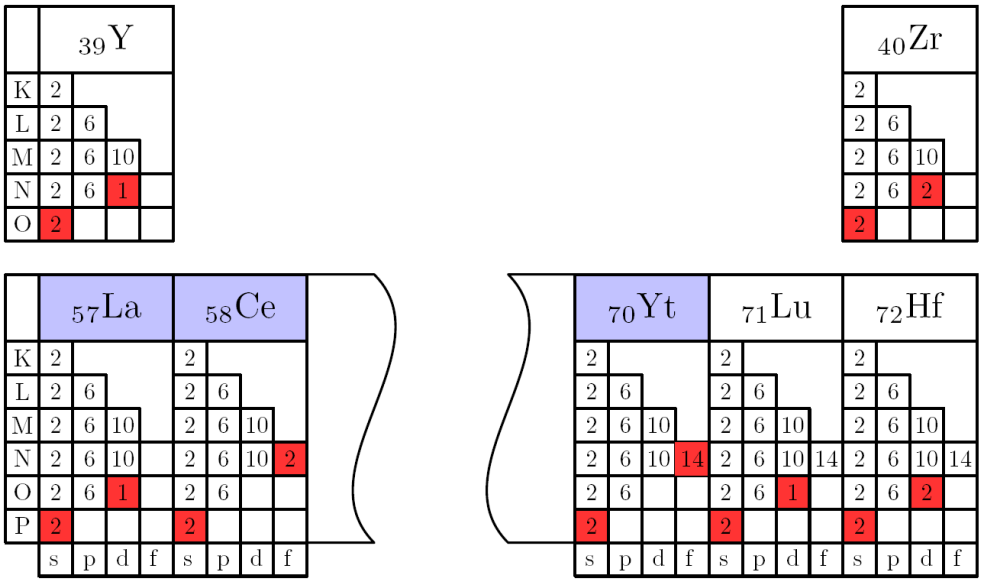

Figure 3.1 | Electron configurations of the Lanthanides (marked with blue background) and surrounding elements. Numbers indicate the number of electrons in a given subshell. The Lanthanides are characterized as having a partially filled 4f subshell inside full 5s and 5p subshells. The 4f shell is filled in close competition with the 5d subshell leading to some disagreement as to which elements should be considered Lanthanides. The figure adheres to what appears to be the most common point of view, that the Lanthanides are the elements between Lanthanum (Z = 57) and Ytterbium (Z = 70), both included.

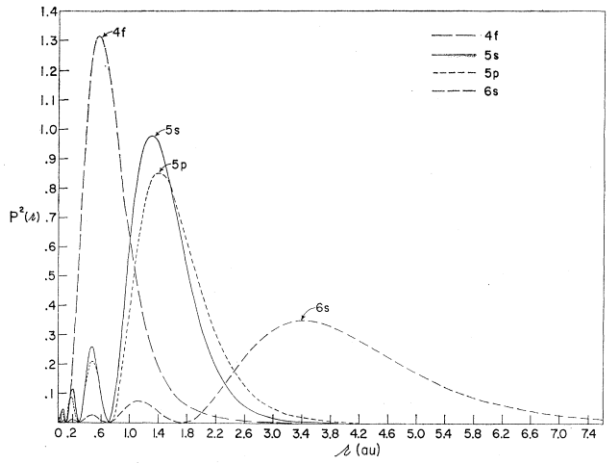

Figure 3.2 | A theoretical prediction of the radial distribution of the orbitals of a rare earth ion (Gd^+). The 4f orbital is seen to lie inside the 5s and 5p orbitals. This figure is from work by Freeman and Watson[86].

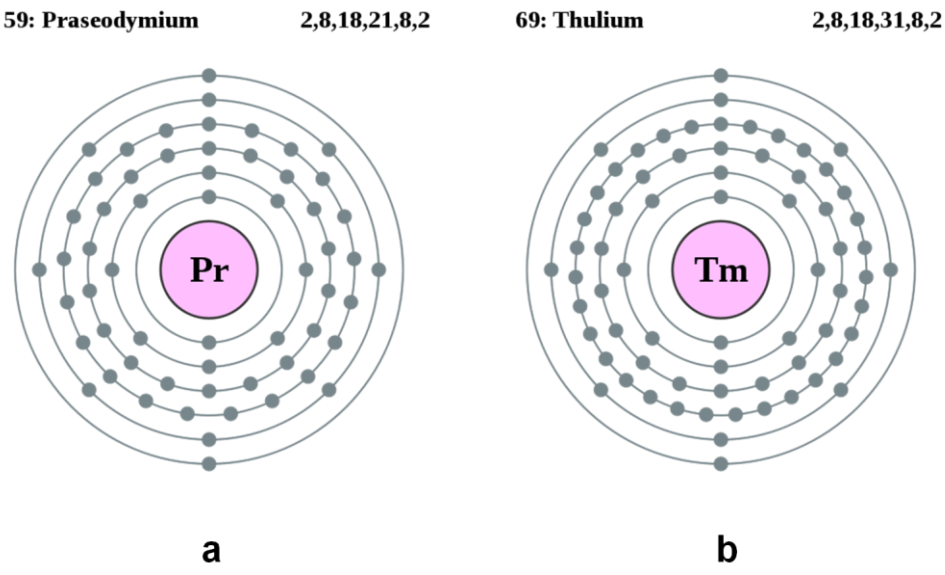

Figure 3.3 | Electronics configuration for Pr and Tm. **a**, Pr: most outside shell [Xe]4f36s2. **b**, most outside shell [Xe]4f136s2.

B. Rare-Earth-Ion-Doped Inorganic Crystals Optical Properties

The optical properties of trivalent rare-earth ions are dominated by transitions between $4f^n$ states. The overall level structure of rare-earth ions embedded in a solid host is similar to that of the corresponding free ions, a fact traditionally attributed to the screening effect of the filled $5s^2$ $5p^6$ shell surrounding the active $4f$ electrons, as discussed in the previous section. When the host material is not itself optically active, as is the case for the inorganic crystals considered here, this fact allows us to consider the system to be a frozen gas of ions. One important exception to this picture is the presence of inhomogeneous broadening: apparent broadening of homogeneous spectral features due to random but constant shifts of the individual ions being observed

1. Typical Energy Level Structure

The gem of rare-earth spectroscopy are the so-called lowest-to-lowest transitions: The splitting between the different J-manifolds, as shown in Fig. 3.4, caused by the spin-orbit interaction, is often larger than the maximal phonon frequency in the crystal, requiring the lowest state of each manifold to decay by multi-phonon decays, leading to life times of up to several ms. In general, the observed linewidths of the lowest to lowest transitions are slightly larger than the limit set by the life time of the excited state. The dominant remaining contributions to the line broadening are spin-fluctuations in the host crystal and ion-ion dipole interactions.

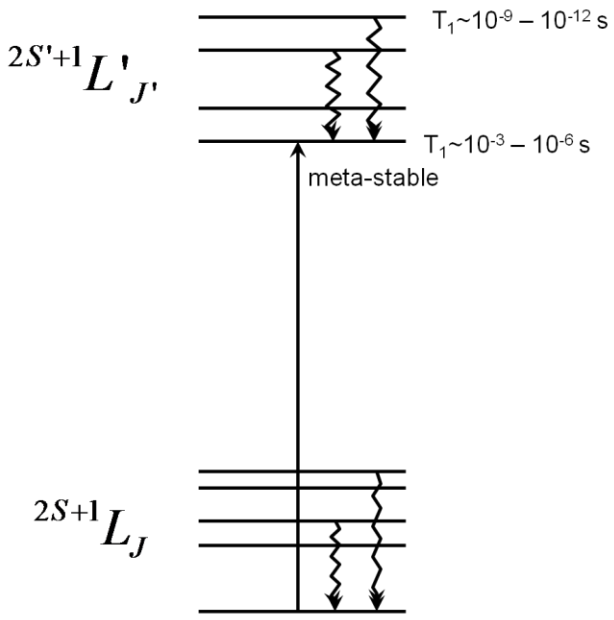

Figure 3.4 | Schematic energy level diagram for trivalent rare earth ions in crystals showing ground and exctied state J-manifolds split by the crystal field. At low temperatures, the upper levels of a manifold relax quickly by spontaneous phonon emission, and the metastable level is usually fluorescent.

The general picture then is that each *J*-manifold in the spectrum of trivalent rare earth ions at liquid helium temperatures is split into a maximum of 2*J*+1 electronic levels lifted by the crystal field (Stark shift). These *J*-manifold separations are typically 10-100 THz. In liquid Helium temperature, this is well above the thermal phonon spectrum (1-100 GHz) so that the transitions are not broadened by thermal phonons. Multi phonon relaxation results in population decay times (T_1) of the lowest crystal field component of a *J*-manifold of $10^{-8} \sim 10^{-3}$ s, which is inhomogeneously broadened by several GHz. In contrast, the upper levels of *J*-manifold will be homogeneously broadened by ~1-100 GHz because of the spontaneous phonon emission. Fig. 3.5 illustrates the electronic energy levels for rear earth doped into $LaCl_3$, measured by *Dieke et al.*[87]. This picture is reproduced from[85]. In our work afterwards, only the transition from the lowest Stark level of the ground state to the lowest level of an optically excited state has been used. The transitions of interest do not involve the absorption or emission of phonons and are therefore known as *zero-phonon lines*. And these transitions are in range of visible or near-infrared.

are similar, since the main contribution is from spin-orbit interaction and not crystal-field interactions.

Before going to finer energy structures, we need to address one issue: The crystal field will also cause mixing of the electronic states, which can cause transitions that would be forbidden in a free ion to become weakly allowed[88]. The conventional labelling of states using the labels of free ion states ($^3H_4$, $^7F_0$ etc.) is therefore slightly

misleading, since quantities such as J are in general only approximately good quantum numbers.

In the RE materials that this work has focused on, hyperfine splitting is caused by second order hyperfine interaction and electric quadrupole interaction. As the electronic magnetic moment is quenched by the crystal field, there is no first-order hyperfine interaction (I-J coupling). As the second-order hyperfine interaction has the form of a pseudo-quadrupole interaction[89] it can be combined with the electric quadrupole interaction into an effective quadrupole Hamiltonian, describing the interaction:

$$H_Q = D\left[I_z^2 - I(I+1)/3\right] + E\left(I_x^2 - I_y^2\right) \tag{3.4}$$

where D and E are coupling constants. From this, the separation between the hyperfine levels can be calculated. In the absence of a magnetic field, the levels are doubly degenerate and for ions with nuclear spin I<1, e.g. Tm^{3+}, there will be no zero-field hyperfine splitting. The levels are conventionally labelled using the quantum number Iz (e.g. $|\pm 1/2\rangle$, $|\pm 3/2\rangle$ and $|\pm 5/2\rangle$ for Pr^{3+} with I=5/2), although the wavefunctions are mixed and may be far from angular momentum eigenstates. These hyperfine levels can have splitting of several MHz (i.e. in Pr:YSO) to several hundred MHz (i.e. in Eu:YSO). Ions can be transferred between hyperfine levels by optical pumping so that PSHB or by applying radio-frequency (RF) pulses, resonant with the hyperfine transition.

Analogous to the optical transitions, hyperfine transitions can exhibit an inhomogeneous broadening, $\Gamma_{inh}^{(hfs)}$, if the hyperfine splittings are slightly different for different ions, due to differences in their surroundings. The inhomogeneous width of the

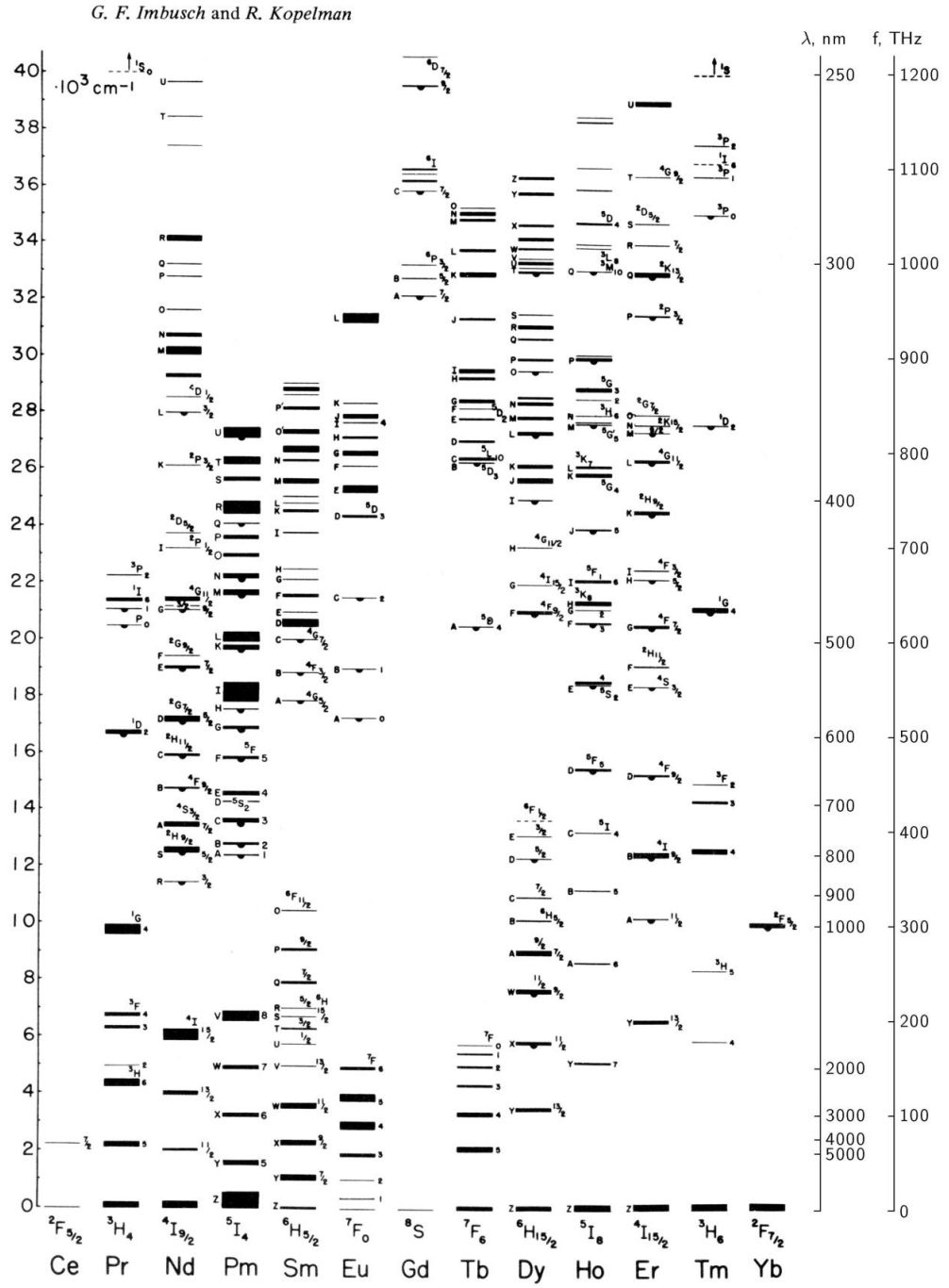

Figure 3.5 | Energy levels for triply ionised rare-earth elements doped into LaCl3 crystals, measured by Deike *et al*.[87] The positions of the energy levels for other hosts

hyperfine transitions in RE materials is typically a few tens of kHz, e.g. 30-80 kHz for the 10 and 17 MHz splittings of the ground state in Pr:YSO[90].

The energy and structure of the quantum states also depend strongly on the host material and the symmetry properties of the *site* in which the rare-earth ion has substituted a host material atom, i.e. its position within a unit cell.

2. Homogeneous Linewidth

The *homogeneous linewidth*, Γ_h, is the width of the spectral region within which a particular ion will absorb or emit radiation. Homogeneous broadening of the resonance frequency is due to dynamic processes and relaxation, and is the same for all ions. The *homogeneous linewidth*, Γ_h, can be written as a sum of contributions from several mechanisms:

$$\Gamma_h = \Gamma_{pop} + \Gamma_{ion-spin} + \Gamma_{ion-ion} + \Gamma_{phonon} \tag{3.5}$$

where Γ_{pop} is the contribution from the excited-state population lifetime T_1, $\Gamma_{ion\text{-}spin}$ is the contribution due to nuclear and electron-spin fluctuations of the host lattice, $\Gamma_{ion\text{-}ion}$ is the contribution from changes in the local environment due to the optical excitation or population relaxation of other ions (instantaneous spectral diffusion), and Γ_{phonon} includes pure dephasing contributions from temperature-dependent phonon scattering. We will give a brief discussion about these mechanisms for decoherence or homogeneous linewidth broadening:

a, fluctuation fields due to spin flipping in neighboring atoms cause decoherence. For ions with and odd number of *4f* electrons, static magnetic field can be used to inhibit

spin flipping, thus the optical transition coherence time will be increased[91-93]. For ions with an even number of electrons, they have non-magnetic electronic levels, which is an important reason for their relatively long optical coherence time[94,95].

b, homogeneous linewidth broadening could be also caused by the coupling of levels, e.g. emission, absorption or scattering of lattice phonons [96]. At low temperatures the number of available phonons is small, but if the temperature is increased above a few K, the density of lattice phonons increases and the phonon contribution to the homogeneous linewidth will dominate, limiting coherence times to ns or ps timescales[97]. c, Interaction between the rare-earth ions and other impurities in the material will contribute to linewidth broadening. Higher dopant density, e.g. shorter distance between ions, will cause excess dephasing through ion-ion interaction. The resulting effect is known as instantaneous spectral diffusion[98-100] . Some experimental studies are included in Fig. 3.6 from thesis by Nilsson[101], which shows neighboring excited ions will broaden the homogeneous linewidth so that the spectral hole as measured in experiments.

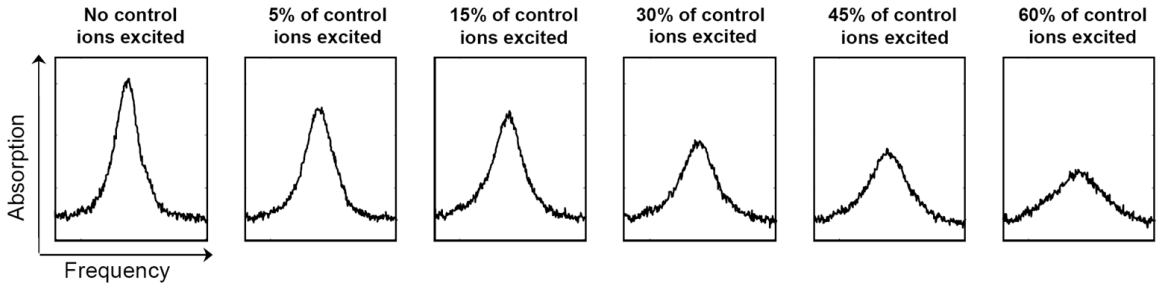

Figure 3.6 | Instantaneous spectral diffusion due to ion-ion interaction, studied in Pr:YSO. The resonance frequencies of a group of ions, originally absorbing within a 100 kHz wide interval, are shifted as an increasing number of neighbouring ions are excited. The ions that are excited (the control ions) absorb within a wide spectral region, elsewhere in the inhomogeneous absorption profile, i.e. outside the frequency region shown in the figures.

3. Inhomogeneous Linewidth

We have considered only homogeneous effects: that is effects which affect all ions equally. What really sets the crystal-embedded ions apart from a gas of free ions (or atoms) is that the ions in a crystal will all have slightly different surroundings due to impurities, defects, or crystal strains caused by the crystal solidifying at finite temperatures. The shifts of the energy levels of the ions caused by these environmental differences are referred to as inhomogeneous shifts: they affect each ion in a constant but random way. When we consider the ensemble of ions in a crystal, such random shifts of the optical transition frequencies of the ions will appear as a broadening of the spectral lines. For the materials considered here, the inhomogeneous broadening of the optical transitions can be as high as several tens of GHz. Pr:YSO (@0.05% doping) has inhomogeneous linewidth of ~5 GHz[102]and Tm:YAG has that of ~20 GHz (@0.1% doping) The hyperfine splittings are much less affected by inhomogeneous effects, and typical inhomogeneous broadenings of the hyperfine transitions are on the order of tens of kHz. The ratio Γ_{ih}/Γ_h gives the number of addressable frequency channels, which determines the capability for processing or storing information in the frequency domain.(Fig. 3.7) Much work has been devoted to increasing this figure of merit, and materials with $\Gamma_{ih}/\Gamma_h \approx 10^8$ have been found[103].

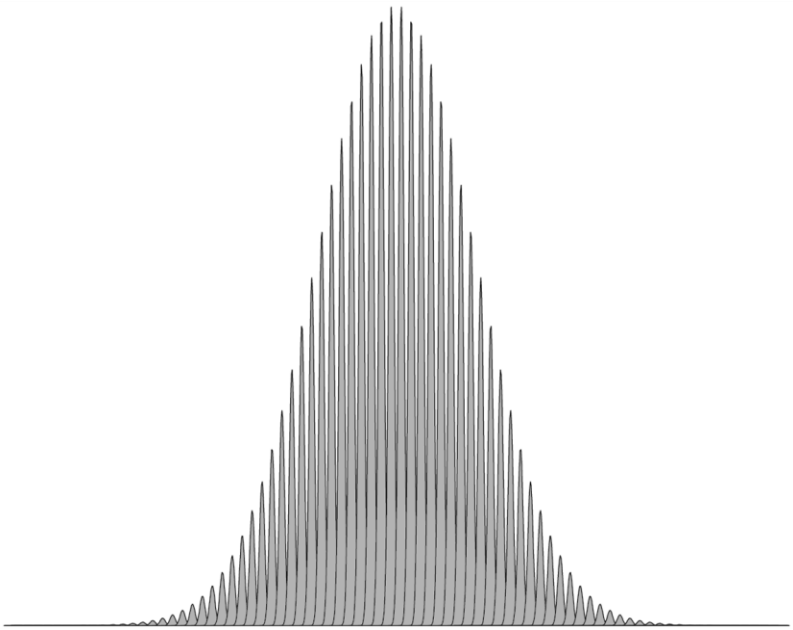

Figure 3.7 | Relationship between inhomogeneous and homogeneous broadening. The inhomogeneous line is made up of a continuum of homogeneously broadened packets. The diagram is not to scale, the ratio of inhomogeneous to homogeneous broadening is much smaller than the ratio encountered in physical systems where it can be as high as 10^7 or even better

C. Properties of Tm^{3+}:$Y_3Al_5O_{12}$ (Tm:YAG)

The Tm^{3+} ion, like all trivalent rare-earth ions with an even number of 4f electrons, has nonmagnetic singlet electronic states when doped into low symmetry crystalline sites, and it is thus relatively insensitive to the homogeneous line broadening induced by fluctuating local magnetic fields arising from mutual nuclear spin flips of host lattice nuclei or electron spin flips of other ions. The lowest levels are the $^3H_6$ multiplet, shown in Fig. 3.8. We are interested in transitions from the $^3H_6$ to the $^3H_4$ levels for which the lowest component to lowest component transitions fall between 790 ~ 800 nm in most hosts. There are two multiplets between $^3H_6$ and $^3H_4$, the $^3H_5$ and the

$^3F_4$ multiplets, but the energy gaps are large enough that the multiphonon decay that broadens Γ_h can be minimized. The $^3H_4$ level relaxes to the metastable $^3F_4$ level, which typically has a lifetime of ~ 10 ms[104]. Although the lifetime of the $^3H_4$(l) level is usually in the ms range or less, spectral hole lifetimes can be as long as 10 ms due to the presence of this third level $^3F_4$. Optical pumping from the ground state to the bottleneck state $^3F_4$ via the upper state $^3H_6$ offers a convenient way to accumulate engraving or hole-burning in another word[105]. Owing to the 500 μs lifetime (optical T_1) of the upper level, an optical pumping cycle lasts about 1 ms. Several cycles can take place during the 10 ms lifetime of $^3F_4$. Experiments verify that a large fraction of the ground-state population can actually be transferred to $^3F_4$. This procedure has an obvious benefit: optimal engraving can be reached without saturating the $^3H_6$ to $^3H_4$ transition, which means lower laser intensity requirements.

Tm^{3+} is also interesting because of its lack of zero-field hyperfine structure due to the $I= 1/2$ nuclear spin. It thus does not have the complication of the hyperfine structure in coherent transient applications [106] or for our SHB UOT. On the other hand, to increase the spectral hole life time (or storage time in quantum information terminology) lifting the nuclear spin degeneracy with an external magnetic field may offer a way for building a Λ system (Fig. 3.9a), provided one is able to relax the nuclear spin Δm_I=0 selection rule. Indeed electronic excitation cannot flip the nuclear spin and this can forbid optical transition along one Λ leg. Observation of long lifetime spectral hole burning in Tm^{3+}:YAG under applied magnetic field proved the nuclear spin

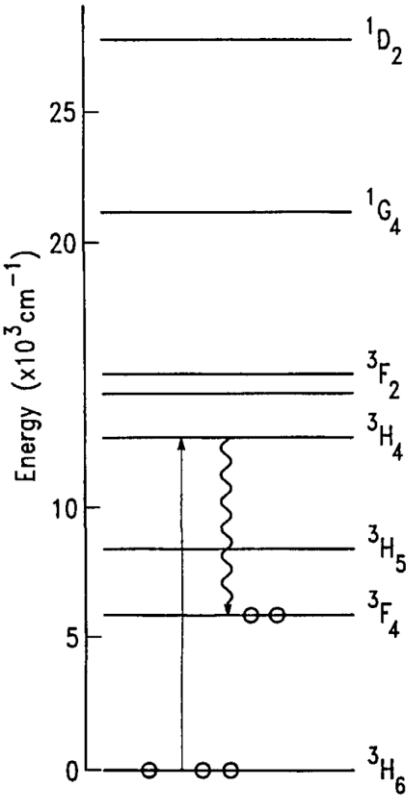

Figure 3.8 | Energy-level diagram for Tm^{3+} showing population storage in the $^3F_4$ metastable level, which is responsible for hole burning.

selection rule can indeed be relaxed[107] and shown in Fig. 3.9b. Theoretical work[108] shows that the nuclear state mixing induced by an external magnetic field and determined the best field orientation for optimizing the relative strength of the optical transitions along the two Λ legs. Later on, the transition probability ratio is also measured[109] and show that Tm^{3+}:YAG can actually operate as a Λ system.

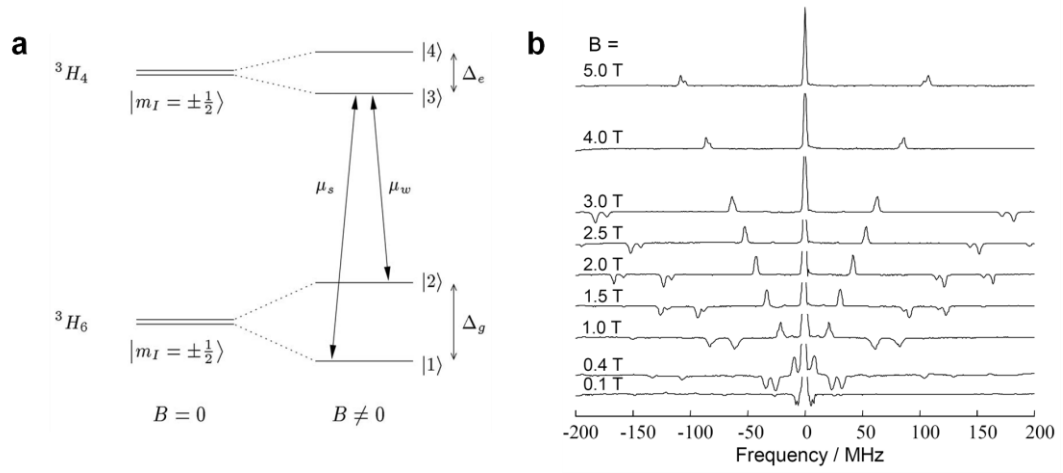

Figure 3.9 | The doubly degenerate nuclear spin states in Tm:YAG (I=1/2) split into Zeeman levels as a magnetic field is applied. **a**, Energy levels for Tm:YAG in magnetic field. **b**, The splitting can be seen in a spectral hole transmission.

Building a three-level system with nuclear spin levels in Tm:YAG, spectral structure that arises as a result of hole burning at magnetic field strengths of 0.1–5.0 T, as illustrated in Fig. 3.9b. The traces are single-shot transmission measurements for which the laser frequency has been scanned over 400 MHz in 190 μs. For clarity, the traces have been offset by an amount proportional to the applied magnetic fields.

YAG ($Y_3Al_5O_{12}$) garnets have the cubic structure with space group O_h^{10}. The Tm^{3+} ions substitute for Y or Lu that occupies local D_2 sites. All of our experiments were carried out on crystals with polished (111) surfaces, with the light propagating along the <111> direction. The $^3H_6$ ground state energy gap Δ_g is 27 cm^{-1} ($\Delta_g = E\left[{}^3H_6(2)\right] - E\left[{}^3H_6(1)\right]$. Since only the first levels above the levels involved in the optical transition are important for understanding dephasing, only energy gaps in the ground and excited states are included). The $^3H_4$ excited state energy gap Δ_e

($\Delta_e = E\left[{}^3H_4(2)\right] - E\left[{}^3H_4(1)\right]$) could be 37cm^{-1} or 72cm^{-1} and needs further discussion. It has been noted that Δ_e is quite large, so there should be no phonon-induced dephasing at the temperatures of interest.

The $^3H_6(1)$ to $^3H_4(1)$ transition of 0.1% Tm^{3+}:YAG occurred at 793.156 nm. The linewidth was Γ_{inh}=20 GHz (0. 7 cm^{-1}) for full width half maximum (FWHM), measured by laser absorption, with a peak absorption coefficient of α = 1.9 cm^{-1}. More concentrated Tm^{3+}:YAG samples have similar linewidths, and the absorption coefficients scale with the concentration. For 2% doping concentration, we measured absorption coefficient of $\alpha \sim 27$ cm^{-1} . This number is smaller than, but still comparable to projected from 0.1% doping, which should be ~ 38 cm^{-1} . The transition dipole for $^3H_6(1)$ to $^3H_4(1)$ was measured by Sun et al. [110] where the optical nutation was measured when the light polarization was rotated relative to the crystal axis <111>. It was determined that the transition dipole is along the <110> direction of the crystal and has an oscillator strength of 8 x 10^{-8}.

Echoes were measured at temperatures varying from 1.4 K to 4.2 K to determine the coherence properties, T_2. Photon echo decay can be fit by the expression:

$$I = I_0 e^{-(4\tau/T_M)^x} \tag{3.6}$$

From experiments, virtually no difference was observed in the echo decay up to 3.5 K. A slight decrease of the dephasing time, from T^M = 105 μs to T^M = 94 μs at 4.2 K, was observed, with T^M obtained by fixing the exponent at 1.9. Because of this relative insensitivity of the echo decay to temperature below 4,2 K, all measurements of the field

and intensity dependencies of Tm:YAG were carried out in superfluid helium (T<1.2 K).

The thermal line broadening of this material was also measured[111] up to 20 K using holebuming and free induction decay, with the result that the direct phonon process dominated the line broadening due to the coupling of the ground state level to the 27cm^{-1} crystal field level (Δ_g). The homogeneous line broadened to 1 MHz at 6 K and 3.5 MHz at 8 K [111]. Using the direct process formalism,

$$\Gamma_h \sim \left(\exp\left(\Delta_{e,g} / kT\right) - 1\right)^{-1} \tag{3.7}$$

This corresponds to a contribution of ~ 10 kHz at 3 K. This linewidth is slightly wider than that observed by the photon echo measurement, since the hole width was measured by hole burning and probably has a contribution from spectral diffusion.

A small magnetic field dramatically lengthens the echo decay time. In a magnetic field on the order of tens of Gauss, strong modulations arise from the Zeeman splitting of superhyperfine sublevels. In fields above 100 G, the lengthening of the decay essentially saturates, although the echo decay shape continues to change due to the field-dependent modulations. The 100 G decay curve gives approximately T_M= 130 μs and x = 1.3 corresponding to Γ_h =2.45 kHz. Although the increase of T_M from 103 μs to 130 μs does not seem very large, when combined with a much smaller exponent x, the decays in a field are dramatically longer. One thing to mention is about magnitude order difference between the magnetic field applied here (to increase the coherence time) and the field to lift the nuclear spin degeneracy (for hyperfine structures). In the former situation, 100 G

(that is 0.01 T) is enough for saturation, but in the latter situation, at least 0.1 T is necessary to resolve the features.

No instantaneous spectral diffusion was observed for the 0.1% sample with Rabi frequencies of a few MHz. However, for the more concentrated crystals, instantaneous spectral diffusion became more pronounced since the active ions were closer to each other. To investigate instantaneous diffusion for these crystals, excitation density was varied over two orders of magnitude. It was observed that as the excitation intensity varied from low to high in these samples, not only the decay time but also the echo decay shape (thereby *x)* changed. As excitation intensity increases, decay times shorten and decay becomes more exponential. There seems to be a correlation between the exponent x and T^M derived from fits to equation 3.6. For example, when T^M =75 μs, x = 1. 55; when T^M =45 μs. x = 1.2; and when T^M is shorter than 30 μs, x = 1.0. This is because, as the decay becomes shorter, the spin flip rate is slow compared to the dephasing time, and the frozen core thawing effect is not important before the coherence is dephased. Fig. 3.10 shows the instantaneous diffusion properties of all of these crystals. As can be seen, at extremely low excitation densities, even the more concentrated samples reach the low excitation limit and give the true decay time. Samples with over 2% concentration were not measured to the lowest intensity, but the same behavior was expected. This is quite interesting, since it demonstrates that Tm – Tm interaction does not determine the ultimate limit of the echo decay or dephasing, while that of Tm - Al does, in direct contrast to the Er^{3+} system, where Er –Er dominates the coherent transient behavior.

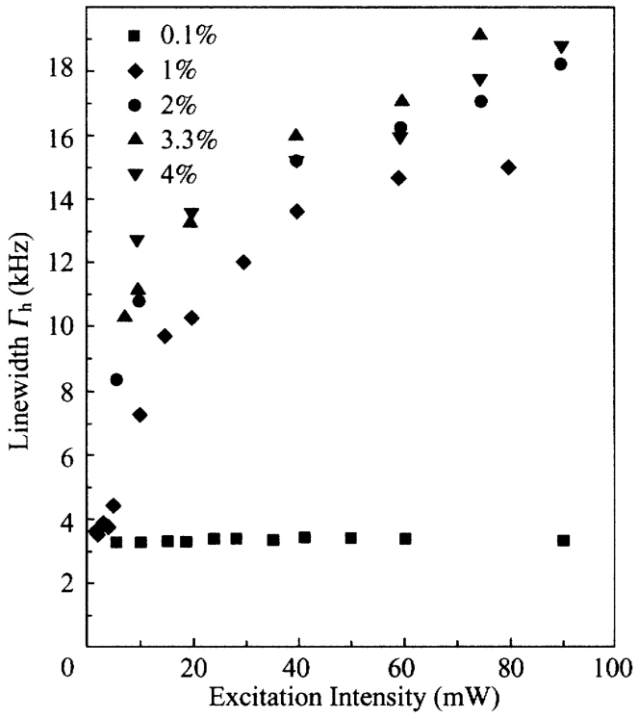

Figure 3.10 | Instantaneous spectral diffusion in Tm:YAG at various concentrations. Instantaneous diffusion was not observed in the 0.1% sample, but it is more dramatic in the higher concentration samples. The low excitation limits for all samples converge.

D. Pr^{3+}:Y_2SiO_5 (Pr:YSO) Material Properties

Because of the importance of Y_2SiO_5 as a crystal host, it is necessary to summarize properties of this material first. Also it is critical to follow the correct definition for purchasing. The Y_2SiO_5 host has low nuclear magnetic moments, since Si and O have no nuclear magnetic moment and yttrium only has a small moment of -0.13μ_N. Y_2SiO_5 crystallizes in a monoclinic cell (C_{2h}^6) described by a = 1. 041 nm, b=0.6726nm, c = 1.249nm, and β= 102.65°. Because this is a monoclinic and thus biaxial crystal, the principal axes of the optical indicatrix do not always coincide with the crystal axes. By symmetry, the C_2 b axis has to be one of the principal axis and the

other principal axes lie in the *a*-*c* plane. These two axes were labeled as D_1 and D2 in [112] with D_1 being 79° from the *a* axis and 24° from the *c* axis; D_2 is in the *a*-*c* plane and perpendicular to D_1 and b. This geometry is shown in Fig. 3.11. The Y ions occupy two crystallographically inequivalent sites each with a distinct C_1 symmetry. Rare earth ions substitute yttrium ions at both sites.

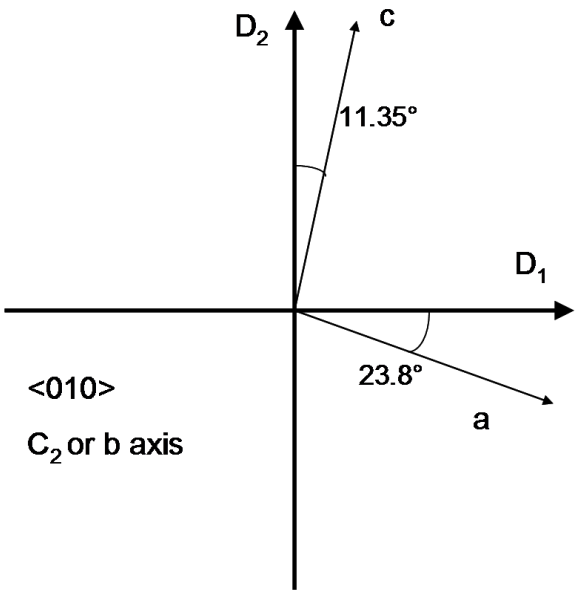

Figure 3.11 | YSO crystallography.

The Pr^{3+}: $^3H_4(l) \leftrightarrow {}^1D_2(l)$ transition occurs at 605.977 nm for site 1 and at 607.934 nm for site 2 at T = 2 K. Very different absorption coefficients were reported for the two site[113]. Recent absorption experiments on an oriented sample determined the very anisotropic absorption coefficients of the two sites, listed in Table 3.1. It can be seen from the table that the total absorption strengths of the two sites are very different.

These differences were also determined to be caused mostly by the very different occupancies of Pr^{3+} ions at the two crystallographic sites, while the oscillator strengths for the two sites are similar.

Table 3.1 | Anisotropic absorption coefficients for the two sites of a nominally 0.05% Pr:YSO crystal. Wavelengths given for the two sites are for the $^3H_4(l) \leftrightarrow {}^1D_2(l)$ transition. Absorption coefficients are given in units of 1/cm. The absorption linewidth for site 1 is 6.2 GHz and that for site 2 is 3.0 GHz, independent of polarization when fitted to a Lorentzian lineshape.

Polarization	Site 1 (605.977 nm)	Site 2 (607.934 nm)
D_1	3.6±0.5	6.0±0.5
D_2	47±5	2.1±0.2
b	<0.1	0.6±0.1

The lifetime and coherence properties were measured with T_1 =164 ±5 μs for site 1 and T_1= 222 ±5 μs for site 2. The $^1D_2$ levels and the lower $^3H_4$ levels are shown in (Fig. 3.12c). Hyperfine structure in this crystal was also studied by hole burning and PENDOR experiments[90,113]. Results (hyperfine splitting and level ordering) are shown as in (Fig. 3.12a,b)

The coherence properties were reported in[113] and extrapolated to a of 2400 Hz for site 1 and 1250 Hz for site 2 at zero intensity excitation in zero field. These linewidths narrowed down to 1800 Hz and 850 Hz respectively in a magnetic field of 77 G. The T_2 for site 1 was also measured in [114] to be 1650 Hz as the zero intensity limit in

zero field. The lifetime-limited linewidth is expected to be 970 Hz and 717 Hz respectively for the two sites. The remaining dephasing, larger than that of Eu:YSO, was attributed to remaining Y - Y spin flips and the higher sensitivity of Pr^{3+} ions due to the larger nuclear gyromagnetic ratio of Pr^{3+} relative to Eu^{3+}. For this unoriented sample, the instantaneous spectral diffusion is 1.2×10^{-11} Hz • cm^3 for site 1 and 1.4×10^{11} Hz • cm^3

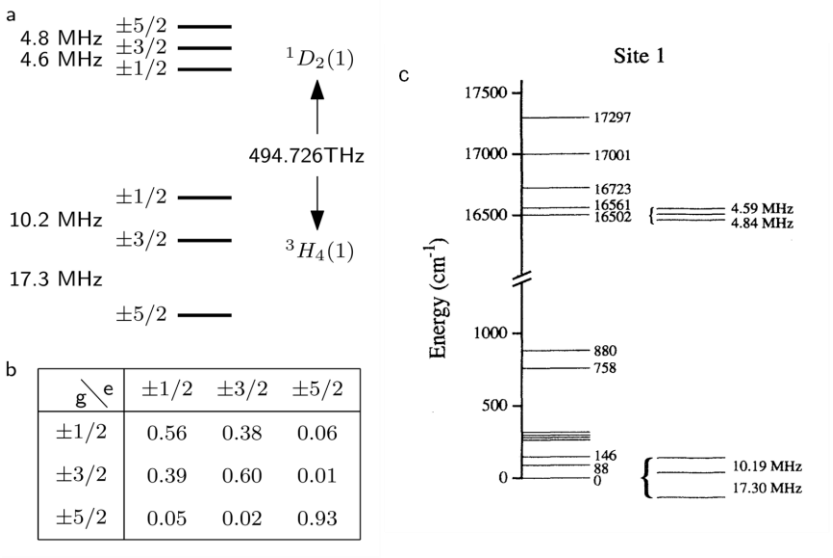

g \ e	±1/2	±3/2	±5/2
±1/2	0.56	0.38	0.06
±3/2	0.39	0.60	0.01
±5/2	0.05	0.02	0.93

Figure 3.12 | Energy levels for Pr:YSO. **a**, Level structure and ordering of Pr:YSO. **b**, Relative oscillator strengths (branching ratio) for all 9 possible transitions. **c**, Energy levels for the $^3H_4$ ground state multiplets and $^1D_2$ excited state multiplets for site 1.

for site 2. The stark coefficients of both sites in this crystal have been measured by Graf et al. to be 111.6 kHz/(V • cm^{-1}) for site 1 and 92.9 kHz/(V • cm^{-1}) for site 2 [115,116]. Graf et al. also investigated a co-doped Eu: Pr: Nd:YSO system and found that the Pr:YSO system's extra dephasing involves non-equilibrium phonons generated by nonradiative relaxation of the excitation. Because of the seemingly larger oscillator strength of this material, it has been used in the study of electromagnetically induced transparency

[117,118]. Combinations of both laser fields and RF fields were used. Optical probe field gain was observed when the RF pulse area was 2π[119]. Later, the probe laser beam was observed to increase by a factor of exp (1.4) at 12 K when a coupling laser of 1.2 kW/cm^2 was applied to the system[120].

E. Summary

Properties of Tm:YAG and Pr:YSO are summarized as in the Table 3.2. It is obvious that Pr:YSO has much longer spectral hole lifetime, higher absorption Coefficient and stronger oscillation strength than those of Tm:YAG. However Tm:YAG works within therapeutic window for tissue imaging purpose.

Table 3.2 | Related optical properties for Tm:YAG and Pr:YSO.

Material	Conc.	λ (nm)	T_1 (μs)	T_2 (μs)	T_{hole}	Γ_{inh} (GHz)	Δ_g (cm^{-1})	Δ_e (cm^{-1})	α (cm^{-1})	f (10^{-9})
Tm:YAG	0.10%	793.156	800	100	~10ms	20	27	70 or 37	1.9	63
Pr:YSO	0.05%	605.977	164	152	~100s	~5	88	59	20	~300

CHAPTER IV

SHB WITH TWO LEVEL QUANTUM SYSTEM IN TM:YAG FOR UOT

A. Introduction to SHB Based UOT

As discussed in last several chapters, we know that the detection of the US-modulated photons in UOT is a demanding task. Challenges come from two sides: first, the modulated photons are usually weak (~1% compared with un-modulated photons and much worse when high frequency short US pulses are used to obtain submillimeter resolution); Second, the modulated photons are also spatially incoherent (time-varying speckles, with small coherence areas). Correspondingly, an ideal detection system for UOT not only should have a big etendue ($G=S\bullet\Omega$, where S is the detector active area, and Ω is the acceptance solid angle) to collect as much as photons, but also needs to be immune to speckle decorrelation.

Both these two requirements can be realized by the narrowband absorptive filter created by the spectral-hole burning (SHB) technique. This technique is capable of selecting one or more sideband(s) of the UOT signal while suppressing the strong dc speckles and the other sideband(s). This system offers UOT the potential for a large *etendue* as well as the capability of spectrally filtering in parallel many speckles with submegahertz spectral resolution. Since our system is based on transmitting the US modulated optical speckles through a frequency-dependent absorptive filter constructed from an SHB crystal, it is inherently immune to speckle decorrelation, potentially allowing *in vivo* imaging.

Not all SHB materials can achieve sufficiently narrowband spectral holes to be useful for UOT. However, certain rare-earth doped crystals operating at cryogenic temperatures can support spectral holes with frequency widths below 100 kHz. These materials can be viewed as ensembles of isolated atoms in a crystal with each atom having a unique optical transition frequency due to its unique local crystal environment. Fig. 4.1 illustrates an SHB material consisting of an ensemble of two-level atoms. The absorption of a two-level atom can be bleached by exciting with a strong enough laser pulse to equalize the ground and excited state populations, as shown. Only atoms resonant with the laser pulse are bleached, thereby creating a spectral hole that can be as narrow as the homogeneous optical absorption linewidth of an individual atom. Once the spectral hole is created, it persists until the excited state decays and can be used to filter out UT light as illustrated in Fig. 4.2.

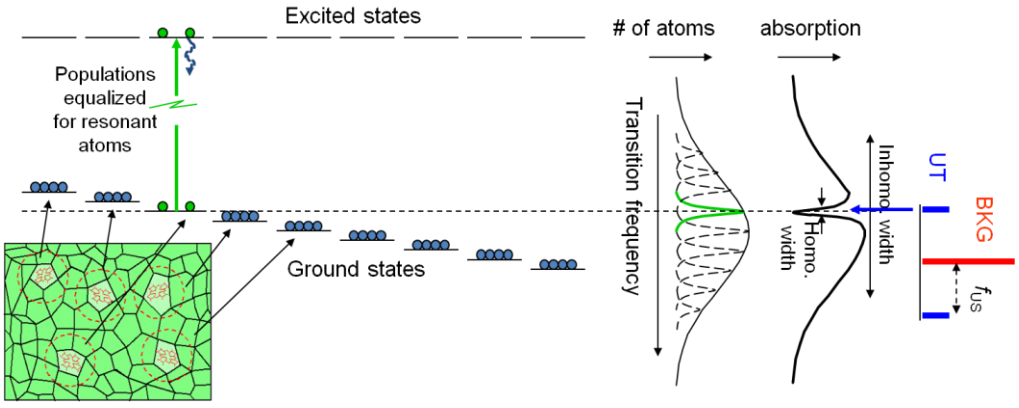

Figure 4.1 | Mechanism of spectral hole burning in a material composed of an ensemble of two-level atoms. Each atom in the SHB crystal has a unique transition frequency based on its local environment. A strong laser beam will saturate resonant atoms, equalizing ground and excited state populations. This creates transparency, or a spectral hole, at the laser frequency.

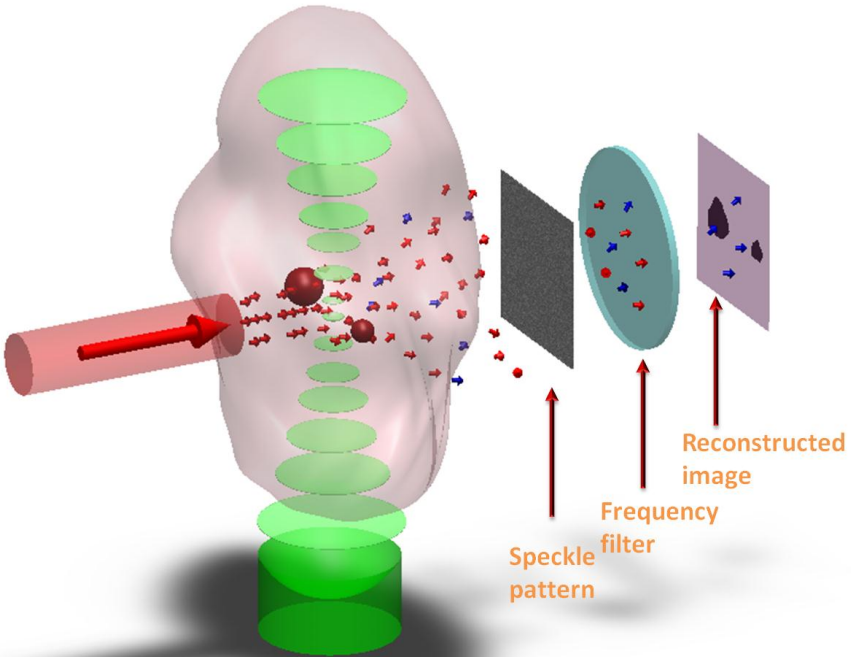

Figure 4.2 | Ultrasound-modulated optical tomography illustration. Small red arrows, diffuse light inside biological tissue; small blue arrows, ultrasound frequency 'tagged' light; a special designed optical frequency filter is used to attenuate or block 'untagged' photons (red color) and extract ultrasound 'tagged' photons (blue color) for image reconstruction.

Our first experiments with SHB UOT are done with Tm:YAG. One reason to start with this material is the availability of the stabilized laser system (Ti:Sapphire) in resonance wavelength (793nm). Also Tm:YAG spectral hole lifetime ~10ms[104,111] is long enough time window for us to detect the UOT signal.

B. Theory of Two-Level Quantum System SHB Based UOT

Before studying SHB UOT experiments, it is better to have a clear picture of the hole burning dynamics with derivations from Maxwell and Bloch (or density matrix) equations. Although Tm^{3+}:YAG is a three-level system (ground state $^3H_6$, excited state

$^3H_4$ and metastable state $^3F_4$), its absorption as measured by the frequency chirp beam is primarily a function of the ground-state population. The excited state $^3H_4$ has a short lifetime, it decays to a bottleneck (metastable) state, so the change in absorption persists until the bottleneck lifetime elapses and the excited ions decay all the way back down to the ground state. This allows us to model Tm^{3+} as a two-level system. But effective T_1 in the following model is ~10 *ms* (metastable state lifetime) instead of real optical T_1 ~ 500 μs. Coherence time T_2 is shorter than or on the order of 10 μs considering our relatively high doping concentration (2%) because of instantaneous spectral diffusion. When a monochromatic laser source (called a pump beam) at frequency ν_P with intensity I_P illuminates a cryogenically cooled SHB crystal, ions at frequency ω that are nearly resonant with the pump beam absorb the photons and are then excited from their ground states, yielding a spectral hole in the crystal's absorption band. As a consequence, the corresponding absorption coefficient $\alpha(\nu_P , z)$ is reduced. We start from 1D slowly varying Maxwell equation[121]

$$d\mathrm{E}(\nu_P, z)/dz = i(K/2\varepsilon)\mathrm{P}(\nu_P, z) = -\alpha(\omega, z)\mathrm{E}(\nu_P, z) \tag{4.1}$$

where $\mathrm{E}(\nu_P, z)$ and $\mathrm{P}(\nu_P, z)$ are the slowly varying amplitudes of the pump beam and the resultant polarization of the medium, ν_P pump laser frequency, z position of interest, $i = \sqrt{-1}$, K is the wave vector, and ε is the permittivity of the host medium. Accordingly, the complex absorption coefficient is given as

$$\alpha(\nu_P, z) = -i(K/2\varepsilon)\frac{\mathrm{P}(\nu_P, z)}{\mathrm{E}(\nu_P, z)} \tag{4.2}$$

As a result, the intensity of the pump beam evolves as

$$dI(\nu_P, z)/dz = -2\,\mathrm{Re}\left[\alpha(\nu_P, z)\right] I(\nu_P, z) \tag{4.3}$$

where $I(\nu_P, z) = (c\varepsilon/2)\left|\mathrm{E}\right|^2$ (4.4)

and c is the speed of light. To understand how the absorption coefficient changes as a pump beam is turned on, we need to solve the polarization of the medium in terms of the pump beam field and single atom (two level system) density matrix formula will be included to get the results.

$$\rho = |\psi\rangle\langle\psi| \tag{4.5}$$

where $|\psi\rangle$ is the wave function with the Shcrödinger picture for two-level single atom system.

$$\rho = \begin{pmatrix} c_a c_a^* & c_a c_b^* \\ c_b c_a^* & c_b c_b^* \end{pmatrix} = \begin{pmatrix} \rho_{aa} & \rho_{ab} \\ \rho_{ba} & \rho_{bb} \end{pmatrix} \tag{4.6}$$

for two level system, we have

$$\dot{\rho}_{ab} = (i\omega + \gamma)\rho_{ab} + i\hbar^{-1}\mathrm{V}_{ab}(z,t)(\rho_{aa} - \rho_{bb}), \tag{4.7}$$

$$\dot{\rho}_{aa} = \lambda_a - \gamma_a \rho_{aa} - \left(i\hbar^{-1}\mathrm{V}_{ab}\rho_{ba} + c.c.\right), \tag{4.8}$$

$$\dot{\rho}_{bb} = \lambda_b - \gamma_b \rho_{bb} + \left(i\hbar^{-1}\mathrm{V}_{ab}\rho_{ba} + c.c.\right), \tag{4.9}$$

$$\rho_{aa} + \rho_{bb} = 1, \tag{4.10}$$

$$\mathrm{V}_{ab} = -\frac{1}{2}\wp\,\mathrm{E}(z)e^{i(Kz-\nu t)} \tag{4.11}$$

$\wp$ is the reduced dipole matrix element (dipole moment) between the excited and ground level transition.In rate equation approximation, coherence time or dipole decay time ($T_2 \equiv 1/\gamma$) is much shorter than times for which the population difference or the field

envelope can change. In the steady state situation, rate equation approximation is exact since the population difference and field envelope are constant. So with rate equation (assume derivative equal to 0) and rotating wave approximation, we have

$$\rho_{ab}(z,t) = -i(\tilde{A}E/2\hbar)e^{i(Kz-\nu t)}\frac{\rho_{aa}-\rho_{bb}}{\gamma+i(\omega-\nu)} \tag{4.12}$$

The polarization can be written in terms of the frequency-dependent population difference $\Delta N = \rho_{aa} - \rho_{bb}$

$$P(z) = 2\tilde{A}e^{-i(Kz-\nu t)}\rho_{ab} \tag{4.13}$$

$$P(\nu_P, z) = -i(\wp^2/\hbar)E(\nu_P, z)D(\omega-\nu_P)\Delta N \tag{4.14}$$

where $$D = \frac{1}{\gamma+i(\omega-\nu_P)} \tag{4.15}$$

Then we will need to work out

$$\Delta N = N_e - N_g = N_0 W(z) \tag{4.16}$$

which is the excited level population N_e minus the ground level population N_g , $W(z)$ is fractional population inversion of ions at frequency ω and position z, $\wp$ is the reduced dipole matrix element (dipole moment) between the excited and ground level transition. Note that $N_e + N_g = N_0$, which is a constant. For an SHB crystal with an inhomogeneous absorption profile given as,

$$G(\omega) = \frac{1}{\Gamma_{inh}\sqrt{\pi}}\exp\left(-\frac{\omega^2}{\Gamma_{inh}^2}\right), \tag{4.17}$$

the number of absorbers resonant with the pump beam is $N_0(\nu_P) = G(\nu_P)N_{inh}$, where N_{inh} is the total number of inhomogeneously broadened absorbers. Next we solve for the fractional inversion $W(z)$ using the optical Bloch equations[121]

$$\dot{U} + U/T_2 = -(\omega - \nu_P)V \tag{4.18}$$

$$\dot{V} + V/T_2 = (\omega - \nu_P)U + (\wp/\hbar)\mathrm{E}(\nu_P, z)W \tag{4.19}$$

$$\dot{W} + (W - W_{eq})/T_1 = -(\wp/\hbar)\mathrm{E}(\nu_P, z)V \tag{4.20}$$

where the dot denotes the time derivatives, U, V, and W are the Bloch vectors and should be normalized according to

$$U^2 + V^2 + W^2 = 1 \tag{4.21}$$

The Bloch sphere is actually geometrically a sphere and the correspondence between elements of the Bloch sphere (Fig. 4.3) and pure states can be explicitly given in the form of Bloch vectors

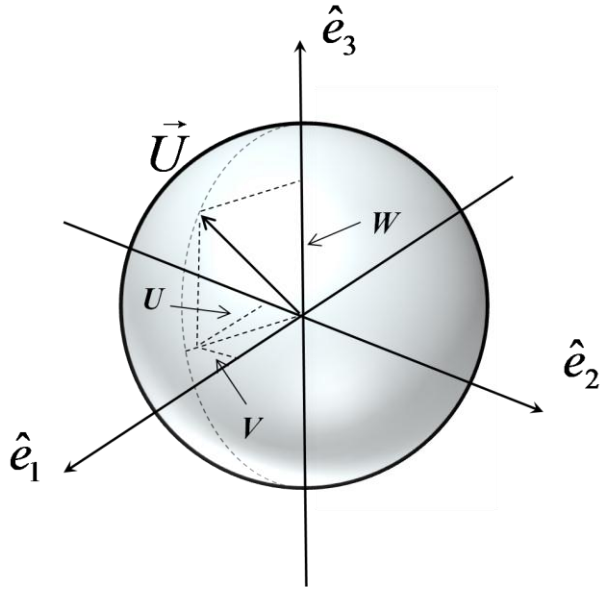

Figure 4.3 | Bloch sphere and Bloch vector.

$$\boldsymbol{U} = U\hat{e}_1 + V\hat{e}_2 + W\hat{e}_3 \tag{4.22}$$

T_1 is the effective excited level decay time including any metastable states. T_2 is the dephasing time or induced dipole decay time. (Note:, in principle, density matrix and Bloch equation will give the same results. Here Bloch equation is arbitrarily included to give a better physics insight about two level system.) Solving equation (4.18-4.21) at the steady state, meaning the time derivatives on the left side are taken as zeros, we can obtain the fractional inversion W as

$$W(\omega', z) = \frac{W_{eq}}{1 + \left[I_P(\nu_P, z)/I_{sat}\right] \mathrm{L}(\omega' - \nu_P)}, \tag{4.23}$$

where W_{eq} is the equilibrium inversion and equals to -1 when no pump beam is present,

$$I_{sat} = (c\varepsilon / 2)\left|\hbar / \wp\right|^2 / T_1 T_2 , \tag{4.24}$$

is the material's saturation intensity, and $\mathrm{L}(\omega' - \nu_P)$ is a real Lorentzian given by

$$\mathrm{L}(\omega' - \nu_P) = 1 \Big/ \left[1 + T_2^2 (\omega' - \nu_P)^2\right] \tag{4.25}$$

So the population difference induced by the pump beam is

$$\Delta N = -\frac{G(\nu_P) N_{inh}}{1 + \left[I_P(\nu_P, z) / I_{sat}\right] \mathrm{L}(\omega' - \nu_P)}, \tag{4.26}$$

Equation (4.26) indeed shows that a monochromatic pump beam engraves a Lorentzian spectral hole in the inhomogeneous bandwidth given by equation (4.17), which reduces the absorption of the crystal at the corresponding frequency. The spectral hole depth is a function of the intensity of the pump beam. And the 3-dB power broadened hole width at each position z in the crystal is given by

$$\delta_{3dB}\left(\nu_P, z\right) = \frac{1}{T_2}\sqrt{1 + I_P\left(\nu_P, z\right)/I_{sat}} \tag{4.27}$$

After the pump beam creates the spectral hole in the SHB crystal, we probe the same spot of the crystal with a weak signal $E_s(\nu_s)$. The signal induced macroscopic polarization in the SHB crystal is contributed by all the absorbers at z regardless their frequencies, therefore it is an integral over the frequency ω, that is,

$$\mathrm{P}\left(z\right) = \int_{-\infty}^{\infty} d\omega' \mathrm{P}\left(\omega', z\right), \tag{4.28}$$

where

$$\mathrm{P}\left(\omega', z\right) = -j\left(\wp^2/\hbar\right)\mathrm{E}\left(\nu_S, z\right)\mathrm{D}\left(\omega' - \nu_S\right)\Delta N \tag{4.29}$$

Because the probe signa[89]l is weak, its contribution to the population inversion is negligible. As a result, the population difference ΔN inside the crystal is the same as the one induced by the pump beam. So substituting equation (4.15) and (4.25) into equation (4.29), and solving equation (4.2) for the complex absorption coefficient of the signal beam, one obtains

$$\alpha\left(\nu_S, \nu_P, z\right) = \frac{\alpha_0}{T_2}\int_{-\infty}^{\infty} d\omega' \frac{G\left(\omega'\right)\mathrm{D}\left(\omega' - \nu_S\right)}{1 + \left[I_P\left(\nu_P, z\right)/I_{sat}\right]\mathrm{L}\left(\omega' - \nu_P\right)} \tag{4.30}$$

where α_0 is the small-signal-intensity absorption coefficient of the SHB crystal given as

$$\alpha_0 = -\frac{N_{inh} K \wp^2 T_2}{2\varepsilon\hbar} \tag{4.31}$$

For the SHB medium considered here, $\Delta\Gamma_h << \Delta\Gamma_{inh}$ (so called inhomogeneously-broadened limit) so we can evaluate $G(\omega')$ in equation (4.30) at ν_S , and take it out of the integral. So equation (4.30) represents a convolution of the probe Lorentzian with the

pump broadened spectral hole. To solve the integral in equation (4.30), first we assume the situation where the pump frequency is the same as read-out frequency ($\nu_S = \nu_P$), then the integration procedure is as Appendix A. Equation (A.4) is called linear inhomogeneous-broadening coefficient. This expression (A.3) tells us when the frequency of signal beam is the same as the pump beam, how deep will be the burned hole. In a more general situation when $\nu_S \neq \nu_P$, let $\delta' = \omega' - \nu_S$ and $\Delta = \nu_P - \nu_S$, $I_2 = \left[I_P(\nu_P, z) / I_{sat} \right]$ (dimensionless intensity)

$$\alpha(\nu_S, \nu_P, z) = \frac{\alpha'_0(\nu_S)}{\pi\gamma} \int_{-\infty}^{\infty} d\omega' \frac{\gamma \mathrm{D}(\omega' - \nu_S)}{1 + I_2 \mathrm{L}(\omega' - \nu_P)}$$

$$= \frac{\alpha'_0(\nu_S)}{\pi} \int_{-\infty}^{\infty} d\delta' \frac{-i}{\delta' - i\gamma} \left[1 - \frac{I_2\gamma^2}{\gamma^2 + (\delta' - \Delta)^2 + I_2\gamma^2} \right] \tag{4.32}$$

This integral is derived in Appendix A. The transmitted signal intensity is

$$I_{s,out}(\nu_S) \exp\left\{ -2\,\mathrm{Re}\left[\int_0^{L_C} \alpha(\nu_S, \nu_P, z)\, dz \right] \right\}, \tag{4.33}$$

where L_C is the crystal thickness. From equation (4.33), we can see that when a probe signal has the same frequency as the pump beam, the probe beam will be transmitted with a reduced absorption. Yet a probe signal with a frequency detuned far away from the pump frequency will be attenuated by the crystal with its original absorption. A sufficiently intense pump beam ($I_P(\nu_P, z) >> I_{sat}$) excites nearly all of the resonant ions in its pathway, and as a consequence, a deep spectral hole at ν_P is engraved into the absorption spectrum of the crystal, resulting in a narrowband spectral transparency at ν_P. For an optically dense SHB crystal ($\alpha(\omega \neq \nu_P) L_C >> 1$), the crystal can thus be nearly

transparent at v_P yet highly absorptive at optical frequencies other than v_P. So the signal with frequency v_P can be filtered through the crystal while other frequency components detuned by more than a hole linewidth given by equation (4.27) are attenuated exponentially. Before going into the discussion in next section, two issues should be addressed: a. Because of the absorption nature from the crystal, the pump beam will also experience attenuation. Requirements for ($I_P\ (v_P\ ,\ z) >> I_{sat}$) should be satisfied in the position where pump light exits the crystal, otherwise saturation condition would not be met and significant amount of population will remain the ground state (thus high absorption persists, which is a shallow spectral-hole). Also due to the coupled nature between electrical field and polarization (in un-saturation condition) will need more rigorous calculation and/or numerical simulation[122,123]. b. Quantum mechanics tell us that even with a perfect monochromatic pump beam, the induced population difference is not a perfect delta function but broadens with the burning beam power as shown in equation (4.26). On the other hand, when the spectral hole is probed with another perfect single frequency signal beam, this beam not only sees the effect of the population difference at this frequency, but also sees those atoms outside the spectral hole, as illustrated in equation (4.30), which is a convolution of the probe Lorentzian with the

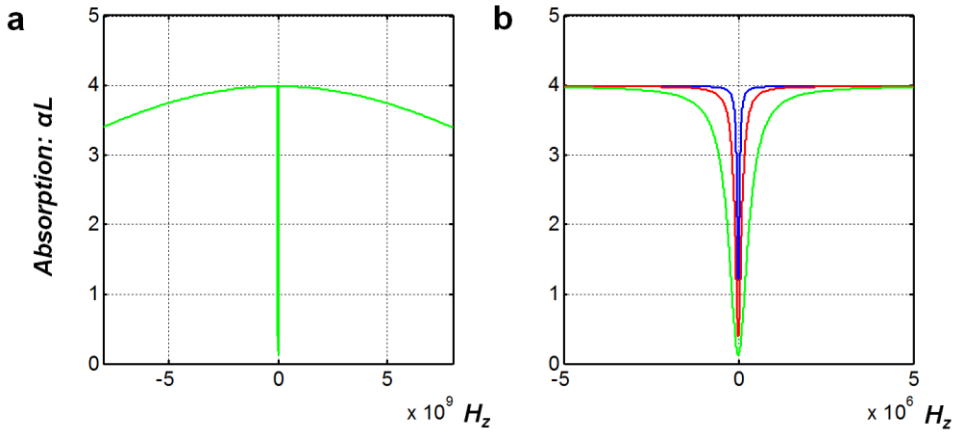

Figure 4.4 | Simulation for hole burning dynamics. **a**, hole burning in inhomogeneous profile. **b**, absorption change due to hole burning varies for different Rabi frequency.

power-broadened Lorentzian. Or from the point of view of atoms, we can think that every atom has an absorption tail (in Lorentzian shape). So even off resonance atoms will affect detuned laser beam. Simulation results with Tm:YAG parameters are shown in Fig. 4.4.

In Fig. 4.4b, green line shows Rabi frequency $\Omega = \sqrt{1000/T_1T_2}$, red line $\Omega = \sqrt{100/T_1T_2}$, blue line $\Omega = \sqrt{10/T_1T_2}$. And $\alpha_0 L$ is assumed to be 4, which corresponds to the experiments in the following section. For 5MHz modulation sideband, this filter can give on/off ratio (defined as $\log_{10}\left\{\frac{\exp\left[-\alpha(\omega_P)L\right]}{\exp\left[-\alpha(\omega_P \pm 5MHz)L\right]}\right\}$) of 15.6dB with burning beam $\Omega = \sqrt{100/T_1T_2}$. This number is consistent with our experiments (~14dB), considering the laser is not a perfect monochromatic wave and has linewidth as broad as ~200KHz.

In UOT, phase modulation model [61] can be used to quantify modulated field or light speckle as:

$$E_n(m,r,t) = A_n \exp\left\{ j\left[\nu_0 t + m\sin(\nu_u t) + \varphi_n(r,t)\right]\right\}, \tag{4.34}$$

where A_n is a constant, m is the modulation depth, and $\phi_n(r,t)$ is a slowly varying random phase characterizing the speckle. For a weak modulation, equation (4.34) can be approximated as

$$E_n(m,r,t) \approx A_n \left\{ \begin{array}{l} \exp\left[j\left(\nu_0 t + \varphi_{n,0}(r,t)\right)\right] \\ \pm\dfrac{m}{2}\exp\left[j(\nu_0 \pm \nu_u)t\right]\exp\left[j\varphi_{n,\pm}(r,t)\right] \end{array} \right\}, \tag{4.35}$$

which represents unmodulated dc light at ν_0 and two modulation sidebands at $\nu_\pm = (\nu_0 \pm \nu_u)$ induced by the ultrasound wave at ν_u. $\phi_{n,0}(r,t)$ and $\phi_{n,\pm}(r,t)$ are random phases associated with the corresponding frequency component. Provided that the frequency of the pump beam coincides with one sideband of the signal given in equation (4.35), say $\nu_P = \nu_- = \nu_0 - \nu_u$, and assuming $\nu_u >> \delta_{3dB}$, substituting equation (4.36) into Eq. (4.34), one obtains

$$\begin{aligned} I_{n,out}(\nu) &= I_n(\nu_0)\exp\left[-2\alpha_0(\nu_0)G(\nu_0)L_c\right] + I_n(\nu_+)\exp\left[-2\alpha_0(\nu_+)L_c\right] \\ &\quad + I_n(\nu_-)\exp\left[-2\alpha_0(\nu)G(\nu_P)\int_0^{L_c}\frac{dz}{\sqrt{1+I_P(\nu_P,z)/I_{sat}}}\right] \end{aligned} \tag{4.36}$$

So for an optically thick crystal with a transparency created by the pump beam, the first two terms can ideally be negligible. Therefore, the lower sideband of the UOT speckle is filtered through. For a practical system, the available pump power is a constant P_0. Provided the beam is expanded uniformly over an area of S, the pump

intensity is $I_P = P_0 / S$. As can be seen from equation (4.26) and (4.27), when the beam area enlarges I_P becomes comparable with the crystal saturation intensity I_{sat} and the spectral hole depth becomes shallower and the hole width reduces. Therefore the filtered UOT signal is a nonlinear function of the pump beam area. Assuming a pump beam illumination disk, the many filtered independent UOT speckles are incoherently integrated with a large area detector, yielding an *m*-dependent photon current of

$$i_{out}(m) \propto \sum_{n=1}^{N} A_n^2 m^2 \exp\left[-2\alpha_0(\nu_P)G(\nu_P)\int_0^{L_C} \frac{dz}{\sqrt{1+\left[P_0(\nu_P,z)/S\right]//I_{sat}}}\right] \tag{4.37}$$

where $S \propto N\sigma_s$, the product of the number N of detected speckles and the average speckle grain area σ_s . So under the shot-noise limited detection condition, the SNR improves by increasing the pump beam area according to

$$\frac{SNR_N}{SNR_1} = \sqrt{N}\exp\left[-\alpha_0(\nu_P)G(\nu_P)\int_0^{L_C} \frac{dz}{\sqrt{1+\left[P_0(\nu_P,z)/S\right]/I_{sat}}}\right] \tag{4.38}$$

where SNR_N and SNR_1 are the *SNR* for N speckles and one speckle, respectively. Ideally, if the pump beam inverts all the resonant ions, resulting in $\alpha(\nu_P = \nu_0 - \nu_u, z) = 0$, the signal SNR grows as $\sqrt{N}$. However in practice, the SNR improvement with increasing pump beam area will be reduced by square-root of the residual absorption of the crystal as shown by equation (4.38), which will eventually cause the SNR to decrease with increasing pump area when the pump intensity falls below the saturation intensity.

For a Gaussian distributed pump beam $I_P(r,\nu_P,z) = I_0(0,\nu_P,z)\exp\left(-r^2/\sigma^2\right)$ with a radius R and the total power P_0, where

$I_0(0,\nu_P,z)=P_0/\left\{\pi\sigma^2\left[1-\exp\left(-R^2/\sigma^2\right)\right]\right\}$ is the peak intensity, σ is a measure of the beam diameter. Equations (4.44) and (4.45) are respectively written as

$$i_{out}(m)\propto A_n^2 m^2\int_0^R dr\,2\pi r\exp\left[-2\alpha_0(\theta_P)G(\nu_P)\int_0^{L_C}\frac{dz}{\sqrt{1+I_0(0,\nu_P,z)}/I_{sat}}\right], \qquad (4.39)$$

$$\frac{SNR_N}{SNR_1}=\sqrt{\int_0^R dr\,2\pi r\exp\left[-2\alpha_0(\nu_P)G(\nu_P)\int_0^{L_C}\frac{dz}{\sqrt{1+I_0(0,\nu_P,z)\exp\left(-r^2/\sigma^2\right)/I_{sat}}}\right]} \qquad (4.40)$$

Clearly if σ is smaller than the crystal size, then it determines the effective *etendue*. From equation (4.39), we see that the UOT signal grows nonlinearly as r becomes bigger. Consequently, the Gaussian profile of the pump beam introduces more complex nonlinearities to the SNR improvement as shown in equation (4.40).

For a focused ultrasound pulse, as it propagates across the focal zone of the transducer, the detected UOT signal has a Gaussian-like profile over its field of view defined along the ultrasound propagation direction, forming the so-called A-line, as verified in our experiments (discussed in the next section) and reported elsewhere[11,20]. A two dimensional tomogram (the so-called B-mode image) of a sample is formed by displaying each A-line at its corresponding lateral spatial position when the sample is scanned. The Gaussian-like background on the A-line degrades the image visibility at the edge of the field of view. This background may be removed as follows: a, If an A-line can be measured in a reference region of the tissue sample with homogeneous optical properties, this A-line can be used as a normalization reference. After the

normalization, a B-mode image with a flat background is produced. b, If such a reference region is not available, digital spectral filtering[124] may be used to demodulate each A-line using a-priori knowledge of the Gaussian-like profile.

C. SHB UOT with Tm:YAG

1. Experimental Setup and Preparation

The present SHB UOT system is schematically shown in Fig. 4.5. The SHB crystal used in our proof-of-concept system is a 10×9×1.5 mm^3 2% at Tm^{3+}:YAG (yttrium aluminum garnet) crystal. Its working wavelength at 793 nm is preferred for biomedical imaging, and solid state laser sources at this wavelength are readily available. The optical absorption length is measured as $\alpha(f)L$=4, yielding a dc background suppression of 18 dB, governed by Beer's law $I_{dc}^{out} = I_{dc}^{in} \exp\left(-\alpha\left(f\right)L\right)$. A cw Ti:sapphire laser (Coherent MBR110), pumped by a frequency-doubled diode laser (Coherent Verdi 10W), is utilized as the source and operates at 793.38 nm with an output of 2W. The laser beam is first frequency shifted by 70 MHz with an IntraAction AOM labeled as AOMRef in Fig. 4.5. (AOM802A1) driven by one channel of an IntraAction dual channel frequency synthesizer (DFE-754A4-16), generating 980 mW, 3.3 ms long optical pulses. These pulses are used as the pump beam, which is beam expanded to cover the 9 mm diameter clear aperture of the crystal. The crystal is cryogenically cooled to ~4 K with a cryostat (Janis, Model: STVP-400). The pump beam burns transparent spectral holes across the crystal's clear aperture [$\alpha(f=70MHz)L=0.9$, and $\alpha(f\neq70MHz)L$=4, corresponding to a 14 dB transmission improvement at this frequency]

forming a number of narrowband bandpass filters, which have a lifetime of about 12 ms. After the narrowband bandpass filters are engraved, the AOMRef is turned off and another AOM of the same model, AOMSam, is turned on with a driven frequency at 75 MHz, equal to the AOMRef driven frequency plus the US frequency of 5 MHz. Light pulse, which is 20 μs in duration and 500 mW in peak power, diffracted off the AOMSam is beam-shaped to a 0.3×8 mm^2 elliptical beam to illuminate the 50×50×10 mm^3 issue mimicking phantom sample. The sample consists of 10% porcine skin gelatine (Sigma G2500) and 1% Intralipid, yielding a reduced scattering coefficient of μ_s' cm^{-1} at the wavelength of 793 nm. A two-cycle 5 MHz US pulse with a peak pressure of 4.3 MPa is simultaneously launched into the sample through water using a focusing transducer Panametrics-NDT, Model: A326S-SU, focal length: 16.2 mm, focal spot size: 0.5 mm). The US pulse has a mechanical index (defined as the ratio of the US peak pressure in megapascal to the square root of its central frequency in megahertz) of 1.9, which is within the US safety limit[125]. The US pulse forms a volumetric ultrasonic field of 0.12 mm^3 (speed of sound in tissue=1.5 mm/μs) in the transducer's focal zone, determining the spatial resolution of the final tomograms. The multiply scattered light distributed along the US propagation direction is sequentially modulated by this US volume as the US pulse propagates through the sample, allowing the creation of a spatial map of the optical properties of the sample along the US path (A-line), as shown in Fig. 4.5 scope trace, where the dip indicates the position of an absorber buried inside the sample. The acousto-optic interaction yields two primary weak sidebands at 70 and 80

MHz in addition to a strong un-modulated dc speckle field. The US-modulated diffused light is passed through the SHB crystal, where

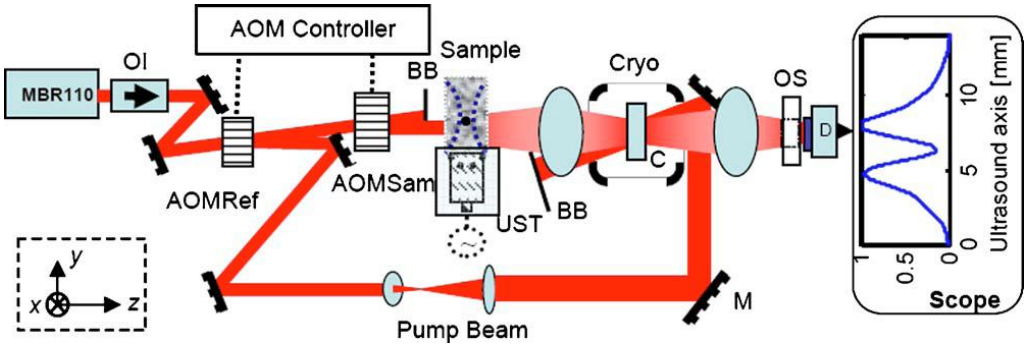

Figure 4.5 | Experimental setup. OI: optical isolator. AOM: acousto-optic modulator. UST: US transducer. Cryo: cryostat. C: crystal. BB: beam block. M: mirror. OS: optical shutter. D: detector. Bottom-left inset: laboratory coordinates: US axis: *y*, light axis: *z*, and sample scanning axis: *x*.

the 70 MHz spectral filters with a bandwidth of 720 kHz (full width at half maximum, FWHM) have been engraved. The spectral filters transmit the sideband of 70 MHz while significantly attenuating the strong unmodulated dc and the other sideband at 80 MHz. The transmitted speckles are detected using a large area Si detector Thorlabs, PDA55. The output of the detector is amplified by 50 times with a low-noise amplifier (Stanford Research, SR 560). An optical shutter (Uniblitz, VS14S2S1) is employed to time gate the pump beam from the detector to avoid detector saturation due to the scattered pump beam.

2. SHB UOT Performance Analysis

I first characterized the spectral filtering capability of the SHB crystal used in our experiments by measuring its absorption, before and after the crystal was cooled. A

frequency-chirped optical waveform (from 50 MHz to 80 MHz, with a chirp rate of 30 MHz/ms) was generated by AOMSam and this was later diffused by the tissue mimicking phantom in the imaging demonstration. The frequency-filtering capability of the SHB crystal is shown in Fig. 4.6a. With the pump beam off, the transmitted light was measured both at room temperature and at a cryogenic temperature of 4.7 K. At room temperature there is no absorption in the SHB crystal, so this data (the blue dot-dashed curve) shows the band shape of the diffraction efficiency versus frequency for AOMSam. At a cryogenic temperature, it can be seen that the majority of light (the black solid line) was absorbed by the crystal. The difference between these two measurements gives the dc suppression as governed by Beer's law $I_{out} = I_{in}\ exp(-\alpha_0 L_C)$ with the pump turned off. For this particular SHB crystal, a dc suppression of 18 dB ($\alpha_0\ L_C$ =4) was measured. A higher dc suppression ratio may be obtained by using an optically thicker crystal ($\alpha_0\ L_C$> 4). The pump beam was then turned on at 4.7 K, and it engraved spectral filters at the desired frequency, 76 MHz in this case. As shown by the red dashed curve, the engraved spectral filters substantially improved the light transmission at the corresponding frequency, while attenuations at other frequencies were unchanged. Transmission improvements of 14 dB were observed at this pump intensity. At the same time, the power-broadened FWHM of the transmission peak, which defines the bandwidth of the spectral filter, was measured to be about 710 kHz.

The acousto-optical interactions in a tissue mimicking phantom with a thickness of 10 mm were also verified by measuring the power spectrum of the UOT signal. The

results are shown in Fig. 4.6a. In this experiment, a 1 MHz ultrasound wave was applied. To observe the ultrasound modulation, a pump beam created the spectral filter at 70

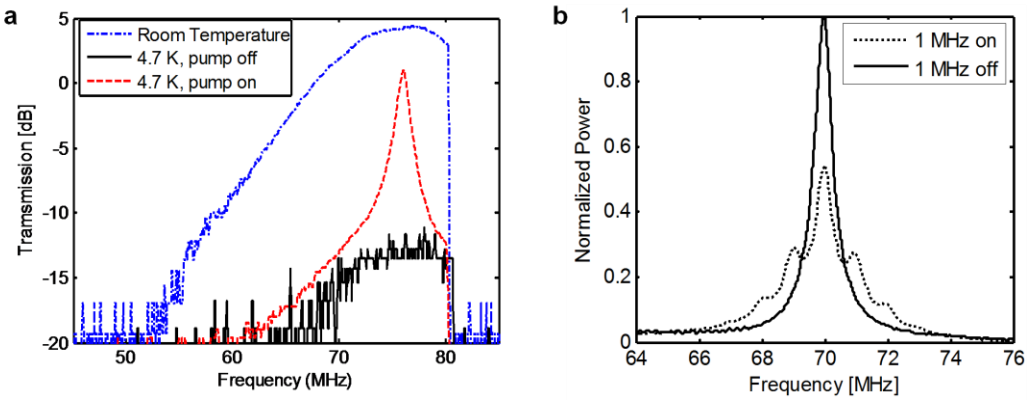

Figure 4.6 | UOT SHB performance. **a**, Spectral-hole shape. **b,** Power spectrum of a UOT signal. Solid line: ultrasound was off. Dotted line: ultrasound was on.

MHz and the sample illumination beam was frequency swept from 60 MHz to 80 MHz.When the illumination light was modulated by the applied 1 MHz acoustic field, UOT signals with 1 MHz modulation sidebands resulted and are shown by the dotted curve in Fig. 4.6b. For comparison, the spectrum of the dc light when the ultrasound field was not applied is shown by the solid curve. Fig. 4.7 shows the diffuse UOT signals transmitted through the SHB crystal as a function of time with the pump beam turned on and off. In this experiment, 2-cycle 5 MHz ultrasound of time with the pump beam turned on and off. In this experiment, 2-cycle 5 MHz ultrasound pulses were used, and the sample illumination light was fixed at 75 MHz. The black trace in Fig. 4.7 is the detected transmission when no spectral filters were created (pump beam off), and the red

trace depicts the transmission when the spectral filters were engraved (pump beam on). It can be seen from the figure that when the pump beam was turned off, both the weak

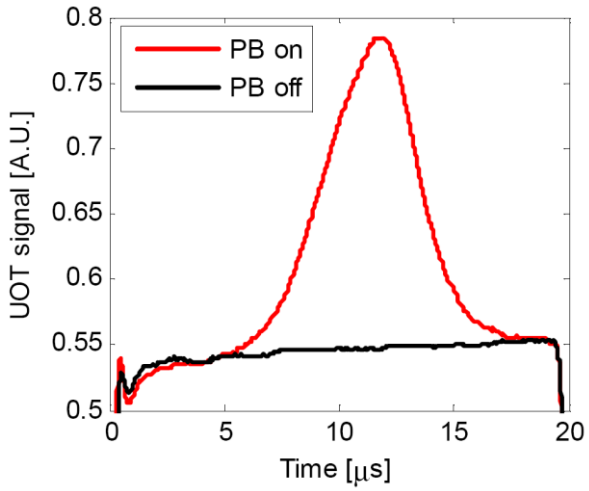

Figure 4.7 | Typical UOT signals with the pump beam on (red) and off (black). PB: pump beam.

ultrasound-modulated sidebands and the strong unmodulated DC speckles experienced the same strong absorption (about 18 dB here), no UOT modulation was detected. This is equivalent to detecting many UOT speckles using a single detector and a neutral density (ND) filter. After the pump beam was turned on to create the spectral filter, the transmission of the UOT modulation sideband at 70 MHz was significantly improved, yet the strong dc and the other sideband at 80 MHz still experienced the same strong attenuation, as governed by equation (4.36). As a result, the weak modulation was detected as shown by the red trace. As a consequence of this spectral filtering and the ultrasound pulse propagation, the optical fluence in the homogeneous scattering medium along the ultrasound propagation path was sequentially mapped as a function of time

(the red trace). This trace is an A-line, and the field of view along the ultrasound axis is primarily determined by the focal depth of the transducer. When an object having a larger μ_a than its surroundings is in the field of view, a portion of the modulated photons generated at the position of the object are absorbed by it, resulting in a dip that indicates the position of the target, as illustrated by the oscilloscope trace in Fig. 4.5.

As predicted by equation (4.37), the detected UOT signal should linearly grow with the number of the processed independent speckles N. By controlling the effective pump beam size, this prediction has been verified experimentally. To demonstrate this point, the pump beam size is varied using an iris, while the US-modulated speckles cover the entire aperture of the crystal. Fig. 4.8a depicts the signal strength as a function of the pump beam size. It can be seen from the figure that the signal strength initially increases nearly linearly as the pump beam size is enlarged, and then the signal growth slows down as the pump beam size is further increased. This is mainly due to two reasons. First, the pump beam obeys a Gaussian distribution as verified in Fig. 4.8b, which burns shallower holes at its edge, yielding weaker signals. Second, the US-modulated light may not be fully diffused since the sample is thin. Otherwise, we may expect that the curve obeys a linear relationship over a larger area.

We also experimentally examined the prediction of the improvements of the SNR by $\sqrt{N}$. Fig. 4.9 shows the measured SNR (stars) as a function of the pump beam area, which is proportional to N. The solid red line is a $\sqrt{N}$ theoretical fitting. It can be seen from Fig. 4.9 that the measured data points at the center agree well with the theoretical fitting. Discrepancy between theory and experiment for the two lowest SNR cases is

likely caused by the digitization error since in this case only a small number of speckles were processed, yielding weak modulated signals and a strong DC background. As a result, the digitization noise dominates the intensity noise (assuming shot-noise limited). The signals became stronger, so the intensity (shot) noise dominated and the measured SNRs coincided with the theoretical predictions. The highest two SNRs falling

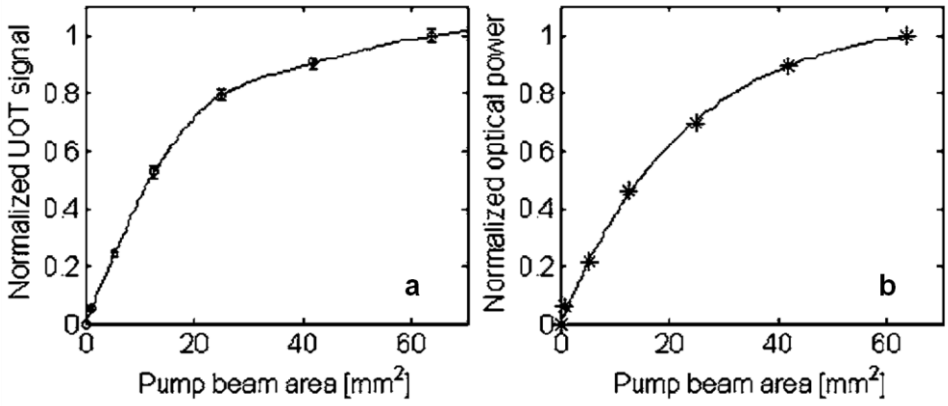

Figure 4.8 | Parallel speckle processing. **a**, UOT signal (circles) as a function of the pump beam size, and the shape preserved fitting (solid line). Error bars: the propagated standard deviations. **b**, Total optical power (stars) vs the pump beam size, and the theoretical fitting (solid line) for the Gaussian distributed pump beam.

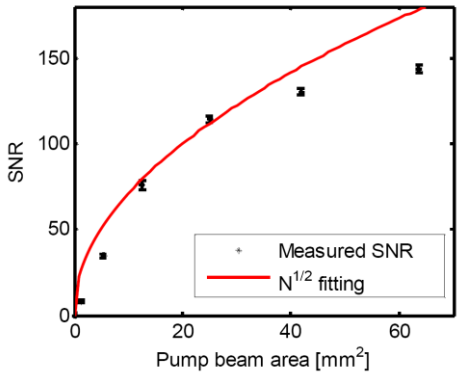

Figure 4.9 | SNR improvement as a function of the pump beam area.

short of the theoretical values are mainly due to the Gaussian distribution of the pump beam, as verified before. Because of the large area of the Gaussian distributed pump beam, the pump intensity at the edge of the pump beam was lower, the spectral holes were burned shallower and the transmitted edge speckles experienced a higher attenuation. Therefore, the transmitted signal broke its linear relationship with N, resulting in smaller SNRs compared to the theoretical values that assumed uniform laser intensity and spatially uniformly processed speckles. Provided a uniform and sufficiently powerful pump beam, one may expect that the measured SNRs will match their theoretical values over a larger pump beam area.

3. Imaging with SHB UOT

The axial resolution of our pulsed SHB UOT is determined by the duration of the ultrasound pulse. This has been qualitatively verified in our experiment. Here, a small absorber (2.8 mm x 1.3 mm x 0.8 mm) dyed by black India ink, photographically shown in the top left inset of Fig. 4.10, was buried inside a 10 mm thick tissue phantom. The absorber was positioned at the focus of the ultrasound transducer. Fig. 4.10 shows A-lines when ultrasound pulses with different durations propagate in the direction of the

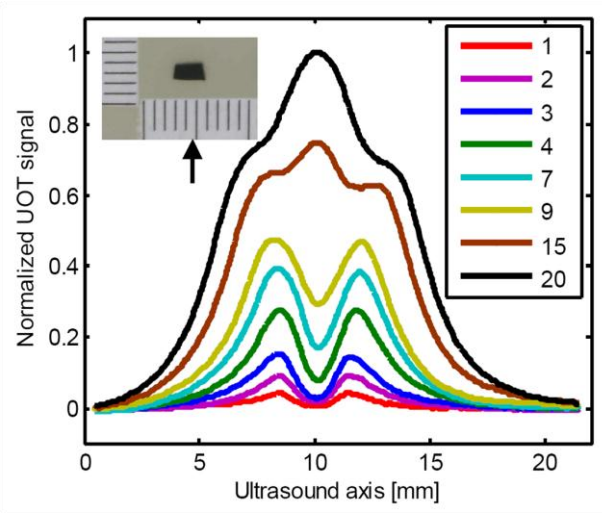

Figure 4.10 | Signal strength and resolution as a function of ultrasound pulse duration. Legend: number of cycles.

black arrow. The dips correspond to the position of the absorber. It can be seen from Fig 4.10 that as the duration of the ultrasound pulse increases, the signal grows. Yet long ultrasound pulses also deteriorate the contrast and resolution of the images. As can be seen from Fig. 4.10, for a 1-cycle short pulse, the image contrast is 88%, whereas the image contrast degrades to only 49% for a 9-cycle pulse. The deterioration of image contrast is due to the degraded resolution. To understand this, let us qualitatively examine the edge spread functions of the image of the absorber. As shown in Fig. 4.10, the bottom edge of the absorber resulted in the falling edge of the image dip, and its top edge induced the rising edge of the dip. When a short pulse, such as the single cycle case, was applied, the two edges were well resolved and separated, so the image contrast is the best. However, when a long pulse, such as the 9-cycle pulse, was applied, because the resolution deteriorated, these two edges consequently spread out to overlap each other, yielding inferior image contrast and distortion. In addition, for very long pulses,

such as those with 15 cycles and 20 cycles, the distortion was so severe that the dip in ultrasound modulated light due to the absorber appears split as if there were two absorbers. The reasons for this split are as follows: since the acoustic pulses extend much longer than the absorber, the dominant signal contribution comes from the region outside the absorber, which has a maximum when the acoustic pulse overlaps with the focal zone. The absorber only slightly suppresses the signal, giving the two shoulders on the central peak.

Fig. 4.11 shows two of our imaging results. A small patterned optical absorber (Black India Ink) was buried in the middle of the tissue phantom, as shown in Fig. 4.11a. The dimensions of the absorber were 0.6 mm along the US propagation direction *y* and 0.9 mm along the light propagation direction *z*. The gap at the bottom of the absorber was about 1.1 mm. It can be seen from Fig. 4.11b that the absorber has been imaged with high fidelity with only 16 times averaging for each A-line, which can potentially be completed within ~320 μs, provided that the spectral filters are engraved and 16 US pulses are fired with a repetition rate of 50 kHz. As will be discussed in the next section, we will see persistent spectral hole burning, especially with Pr:YSO, will enable us to speed up the data acquisition. The repetition rate is so chosen that crosstalk between adjacent pulses is avoided. This speed may enable real time imaging. For this imaging speed, the optical power for each A-line imaging location is 6.7 mJ cm^{-2}, which is well below the ANSI laser safety limit at 793 nm.[23] To explore the imaging speed limit of our technique, we reduced the averaging times. As shown in Fig. 4.11c a fair image can be obtained with only four times averaging, offering a potential for an 80 μs acquisition

time per A-line. The major noise source that limits our current system from performing single-shot imaging might be intensity noise induced by the laser's stabilization system, whose spectrum with a spectral peak at ~85 kHz coincidently overlaps with that of our UOT signals, causing artifacts on our single-shot images. However, it should be pointed out that the imaging speed as well as the overall performance of our system can be significantly improved if an optically thicker crystal is used to further suppress the strong dc (as in the situation of our experiments with Pr:YSO) and/or a balanced detector [126] is employed to reject the laser noise.

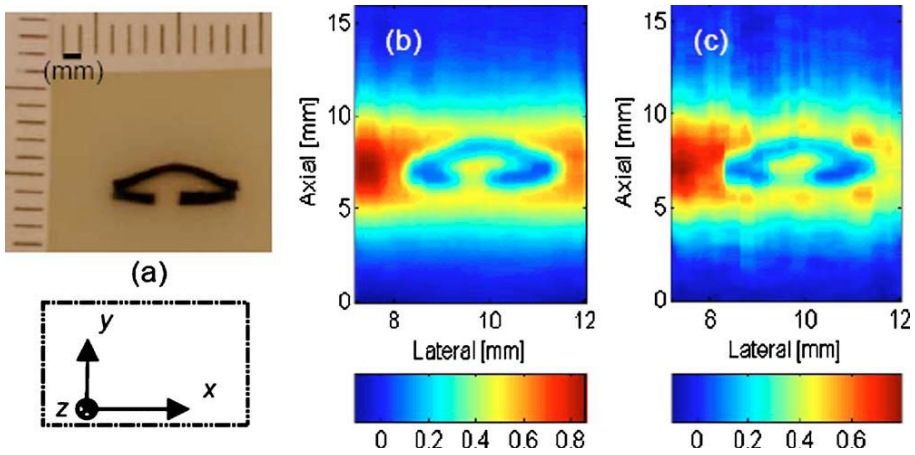

Figure 4.11 | B-mode tomograms. **a**, Photograph of the optical absorber buried inside the tissue phantom. **b**, Tomogram with 16 times averaging. **c**, Tomogram with four times averaging. Tomograms are interpolated and median filtered. Bottom-left inset: lab coordinates.

The large optical *etendue* is one of the major advantages of our system. In principle, the acceptance angle of our absorption-based quantum filters can be nearly 2π, yielding an *etendue* of 1131 sr mm^2 for a 10×9 mm crystal aperture. In our current system, the effective *etendue* for this front-end filter is calculated as 31 sr mm^2, limited

by the cryostat windows and sample holder geometry. Yet this *etendue* is already an order of magnitude improvement over the photorefractive photorefractive crystal based technique (as mentioned in PR UOT chapter) and more than two orders of magnitude improvement over the CFPI.[23] Moreover, the *etendue* of our system may be further improved by proper design of the cryostat, for example learning from microscopy cryostat which is designed for numerical aperture(NA) bigger than 0.7, which corresponds to a solid angle of ~3 sr. With this solid angle, we can get as good *etendue* as 280 sr mm^2 for 10×9 mm crystal aperture.

As pointed out previously, tomograms obtained with our pulsed UOT system have a Gaussian-like background in their axial dimension, and this background degrades the image visibility. Fig. 4.12 shows one of our B-mode tomograms obtained with the present system. In this experiment, a patterned absorber dyed with black India ink,

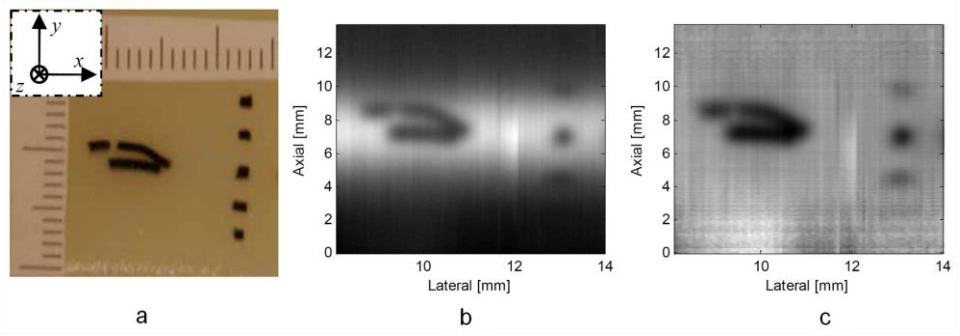

Figure 4.12 | Tomogram obtained with the SHB UOT system. **a**, Photograph of the object. Scale in mm. Left top inset: lab coordinates. **b**, B-mode tomogram with the background. **c**, B-mode tomogram with the background removed by division.

photographically shown at the left side this experiment, a patterned absorber dyed with black India ink, photographically shown at the left side of Fig. 4.12a was buried in the

middle of the 50 × 50 × 10 mm (*x, y, z*) tissue phantom to mimic the optical absorption of a soft biological tissue. The dimensions of the top and bottom lines along the ultrasound axis *y* are 0.6 mm and 0.7 mm, respectively. The gap between these two lines is 0.7 mm. The thickness of the target in the light propagation direction *z* is 0.9 mm. At the right side of this absorber, five cubic absorbers (0.85 × 0.85 × 0.85 mm) were also buried along the ultrasound propagation direction. The separation between adjacent cubes was about 3 mm. In the experiment, the ultrasound transducer and the sample illumination light were fixed. The phantom was scanned along *x* for 14 mm with a step size of 0.2 mm. Each A-line was averaged 64 times and the tomogram was interpolated. The theoretical axial resolution is 0.6 mm. As shown in Fig. 4.12b, the patterned absorber was imaged with high fidelity, and the 0.7 mm gap was well resolved. Fig. 4.12c also shows the limited field of view as well as the undesirable background. It can be seen that only the central three cubic absorbers are visible. The other two, at the top and the bottom, are not detected because they are out of the field of view. Moreover, it is also obvious that the Gaussian-like background deteriorates the visibility of the structure. The Gaussian-like background can be removed by normalizing each A-line to an absorber-free reference A-line. Fig. 4.12c shows the same tomogram as Fig. 4.12a but with the background normalized to a reference A-line. The reference A-line used here is the A-line at the center of the gap between the patterned absorber and the cube absorbers. It can be seen that the visibility has been significantly improved.

CHAPTER V

PERSISTENT SPECTRAL-HOLE BURNING (PSHB) IN PR:YSO FOR UOT

A. Introduction to PSHB UOT

As discussed in previous chapters, ultrasound-modulated optical tomography (UOT) promises to give ultrasound resolution with a high optical contrast[9,11]. Aside from potential applications to manufacturing diagnostics and materials research[41,51] (usually called optical measurement of ultrasound in these areas), UOT is of great interest for medical diagnostics. An example is early cancer detection, where conventional ultrasound does not give adequate contrast, and all-optical techniques cannot probe deep enough, at least with high resolution, due to strong tissue scattering. Unfortunately UOT has not been considered to be widely applicable for medical applications because until recently[127], it has been largely limited to tissue depths of a few centimeters, with a so-called "hard-depth limit" for optical imaging above 5 cm[6]. Here we show that the superior filtering and *etendue* properties of persistent spectral hole burning (PSHB) materials can give a detectable UOT signal in a 9 cm thick tissue phantom. Making straightforward projections to higher laser illumination power and relatively simple improvements in the *etendue* of our experimental apparatus, we expect 18 cm single shot imaging depth. Moreover at this depth, our projections show that UOT is potentially able to achieve a depth-to-resolution ratio (DDR) of >100, which is good enough for many medical diagnostic applications. A related technique photoacoustic tomography (PAT)[128] also gives optical contrast for ultrasound images but detection is of the optically

generated ultrasound pulse, rather than the scattered optical power. In many cases these techniques are complementary[36] giving non-redundant information on tissue properties. However, in PAT the light intensity deep inside the tissue must be high enough to create a significant acoustic pulse and this limits its maximum depth to ~5 cm at high resolution[129,130]. In contrast for UOT, ultrasound is directly input to the tissue and so the optical power deep inside the tissue need only be high enough to generate enough "tagged" light for detection on the outside, and so can potentially image much deeper inside tissue. As a hybrid or sometimes called multiwave imaging modality, UOT is getting more and more interests from different research communities because of its outstanding imaging capabilities[131].

1. Main Challenge of UOT

The main technical challenge for deep tissue imaging with UOT is the relatively low light intensity deep inside the tissue sample[6] and the small focused ultrasound volume, causing the ultrasound tagged light to be many orders of magnitude weaker than background "untagged" light[57]. Thus the success of UOT lies in the development of a superior optical filtering technique, as well as the collection of as large a fraction of the total tagged light as possible. This later requirement places a constraint on the *etendue* (product of solid angle and area) of the optical filter as the light from deep inside the tissue sample emerges with nearly 4π steradian solid angle. If the *etendue* of the filter is too small, not enough tagged photons are collected to produce an image even though the filter discrimination capability may be very high. Since *etnedue* is a quantity that cannot

be improved by geometric optics elements, the optical filter must inherently have a high *etendue* property. This consideration rules out most high-performance optical filtering techniques that have been developed in the past few decades.

As mentioned above, the problem of imaging deeper into tissue is twofold. First, the modulation depth (percent of input light converted into tagged light) decrease as tissue depth increases. However beyond a certain depth this saturates due to the light being fully diffused or sufficiently multiply scattered[57]. Therefore the main problem is the loss of ultrasound tagged light due to absorption or scattering out of the detection path as it leaves the sample. The absorption can be reduced by using laser wavelengths in the optical therapeutic window because of the low level of hemoglobin absorption. However the problem of tagged light attenuation due to multiple scattering can only be solved by using an optical filter having a large *etendue*. Moreover this filter must be very narrowband (compared to typical optical filters) where the maximum bandwidth is determined by the ultrasound frequency, typically several MHz.

2. Prior Work in UOT For Deep Tissue Imaging

UOT has been investigated for almost two decades both in experiments and in theory[61,132,133], but only recently have tissue imaging demonstrations been done with ~mm resolution close to or even beyond 'the hard-depth limit for optical imaging (~5 cm) . One of these uses a high power pulsed laser, as in PAT, to overcome the photon loss problem[127]. This technique images inside 6 cm *ex vivo* tissue samples using a Fabry-Perot (FP) optical filter. However, the technique will not be able to image much deeper

into tissue because of the limited *etendue* of the filter and the proximity to the laser exposure threshold[134]. The next deepest imaging demonstration was done with a high speed photorefractive (PR) filter having a much higher *etendue*. In this work a continuous-wave (CW) UOT signal was detected down to a depth of 4 cm[46], but for pulsed ultrasound only down to ~2.7 cm[22]. Pulsed ultrasound excitation is generally preferred due to its high resolution in the ultrasound propagation direction, faster imaging speed and compatibility with the well-established conventional ultrasound imaging technique[22]. Of these two techniques, the PR filter has the potential for higher *etendue*, but it is an active filter which requires an additional strong pump beam that is also scattered inside the crystal, thereby causing additional background light that must be filtered. By far the largest *etendue* yet reported is with SHB materials[135,136] and therefore versions of these working in the infrared have the best promise of achieving the elusive goal of deep tissue UOT. In this chapter we explore a special class of SHB filters called persistent spectral hole burning (PSHB) which can be prepared to have orders of magnitude better filtering discrimination than non-persistent SHB filters.

3. More on Pr:YSO Properties

For these experiments we use the $^3H_4 \leftrightarrow {}^1D_2$ 605.98 nm optical transition of Praseodymium ions in $Pr^{3+}:Y_2SiO_5$ (Pr:YSO) because of its long hole burning persistence time (T_1~100 s)[90]. This system has been extensively investigated for a variety of applications ranging from high density optical memories to quantum memories with ultralong storage time[137-140]. For these applications the important

properties are a relatively long optical coherence time (152 μs)[113], a long ground state spin coherence time (~0.5 ms to 1 minute using dynamic decoupling pulse sequences), and a long ground state spin population relaxation time[90].

For UOT applications the important parameters are the long optical T_2, the long spectral hole persistence time T_1, a relatively strong optical oscillator strength and a very high *etendue*. The long optical T_2 gives a narrow homogenous linewidth and therefore narrow spectral holes, down to tens of kilohertz widths with stabilized laser[140]. This combined with the strong oscillator strength gives the possibility to make optical filters with unprecedented performance, for example recently it was shown that a 140 dB on/off ratio (ratio of absorption over different frequency inside spectral feature) for a 140 kHz width spectral feature has been achieved[140]. As the optical filtering is done by individual ions in the crystal, there is no *etendue* limit in principle, though in practice polarization selectivity of Pr:YSO absorption does limit *etendue*[114]. Note that this limit does not exist with all SHB filters, a notable example being $Tm^{3+}:Y_3Al_5O_{12}$ (Tm:YAG) which has already been used to demonstrate UOT applications. Tm:YAG also has the advantage of working in the near IR at 798 nm where tissue is minimally absorbing and weakly scattering, whereas Pr:YSO operates in the visible (orange). However Pr:YSO has a significant advantage in spectral hole lifetime compared to the usual holeburning mechanism in Tm:YAG which involves storage in a metastable excited shelving state $^3F_4$, having a 10 ms lifetime[135]. In Pr:YSO the hole lifetime is given by ground state population decay and is on the order of minutes which is so long that it can be essentially ignored on the timescale of UOT imaging. SHB materials with such long hole lifetimes

are known as persistent spectral hole burning (PSHB)[141]. Here we note that Tm:YAG has previously demonstrated hyperfine hole burning[107,109] and hence may eventually replace Pr:YSO because of its friendlier operating wavelength (considering more difficulties of operation with dye laser than solid state or semiconductor lasers), even though it has a smaller optical oscillator strength. Finally we note that Pr:YSO has been used to show coherent optical pumping[117]. In this configuration Pr:YSO has unprecedented efficiency for four-wave mixing[142] making it superior to photorefractive materials that are currently extensively used in UOT.

B. Experiment Details for UOT with Pr:YSO

1. Experimental Setup

We now present a demonstration of UOT using an optically thick Pr:YSO crystal to create a frequency filter with a 1 MHz pass band via optimized sequences of erasing/initialization, burning and probing pulses. Experimental results with thick tissue mimicking phantom and chicken breast tissue will also be shown and discussed.

The experimental setup is shown in Fig. 5.1. A highly stabilized dye laser[143] delivered around 100mW through a polarization maintaining single mode fiber into the UOT portion of the experimental system. A beam sampler picked off roughly 10% of total light after the fiber and directed into a photodiode (Thorlabs, PDA10BS) to serve as a reference (time and intensity) for signal calibration. Different optical subsystems were used to prepare the PSHB optical filter and to perform the UOT measurements. To steer the light between the two subsystems (or operation modes): 1) hole erasing/burning

mode and 2) UOT probing mode, a galvo mirror was used to switch between these two subsystems, which are denoted in Fig. 5.1 by dashed and solid lines respectively. Its scanning speed could be as fast as 10 Kpps (point per second), which is faster than needed to generate a video rate UOT image.

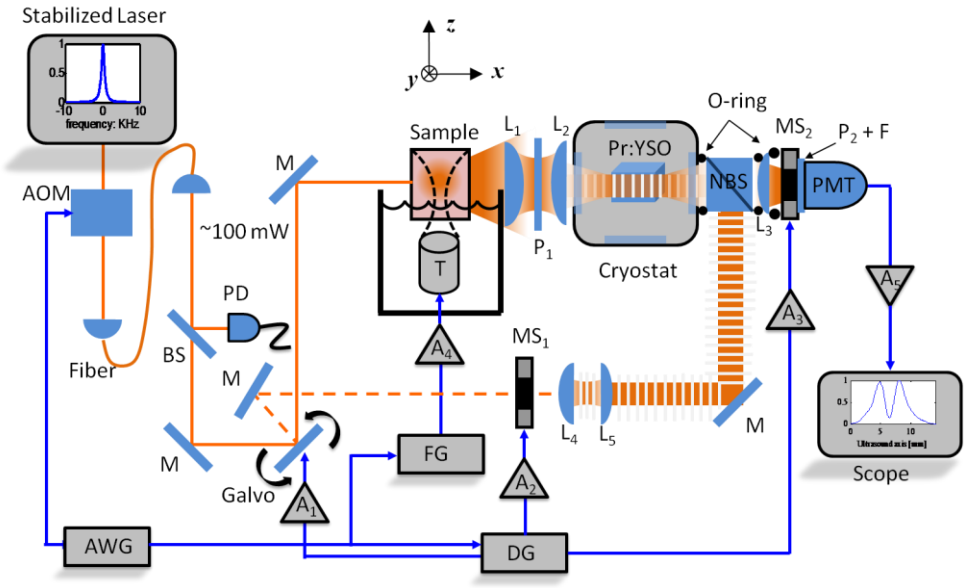

Figure 5.1 | Experimental setup schematics. AOM, double-pass acousto-optical modulator system; BS, beam sampler; M, mirror; PD, photodiode; $L_{1\sim5}$, lens; NBS, non-polarizing beam splitter; $MS_{1\sim2}$, mechanical shutter; $P_{1\sim2}$, polarizer; F, fluorescence filter; PMT, photomultiplier tube; AWG, arbitrary waveform generator, Tektronix AWG520; FG, function generator; DG, delay generator; $A_{1\sim5}$, amplifier or instrument driver; T, US transducer; orange color line, light propagation trace (solid trace for probing, dashed trace for erasing and burning); blue color line, electronic signal.

At the beginning of the erasing and burning pulse sequence, a mechanical shutter (MS_1) was turned on and the laser beam sent through a lens to expand and collimate to 6mm diameter which fills the aperture of the mount used to hold the crystal in the cryostat. A non-polarizing beam splitter, sitting inside a light tight cube mount, delivered

half of the laser power into the Pr(0.05%):YSO crystal for hole erasing and burning. The other half was dumped. The light path for this burning/erasing beam was counterpropagating to the UOT imaging direction to avoid accidental exposure of the sensitive detector (PMT as in the Fig. 5.1) to the full power laser pulse. To protect the detector from the still powerful scattered light during burning/erasing, another shutter, MS_2 was kept closed during erasing/burning mode to keep the PMT in dark before probing the signal. In probing mode, the galvo scanner steered the laser beam onto the phantom sample on the side opposite the Pr:YSO crystal, as shown in Fig. 5.1. Scattered light from the sample was collected by a pair of aspherical lenses L_1 and L_2 with focal length of 40 mm and 25 mm respectively and imaged onto the Pr:YSO crystal aperture. Light spectrally filtered through the Pr:YSO crystal was passed through the beamsplitter, already described above, followed by a collection lens to image the crystal output onto the PMT (photomultiplier) detector.

In the switching from burning/erasing to UOT acquisition mode, enough time (usually several tens of milliseconds) was set aside to make sure that the mechanical shutter MS_1 had time to fully switch off before a second shutter MS_2 was turned on to deliver the UOT signal into the PMT (Hamamatsu R928P with 8×24 mm^2 active detection area, cooled down to -30 °C). This long delay time also ensured that any residual fluorescence of the Pr:YSO at the laser frequency had time to fully decay. Because of the polarization sensitivity of Pr:YSO [114], a 2 inch nanoparticle linear film polarizer (colorPol VISIR, ±20° acceptance angle) was inserted between the input lens pair to purify light polarization. The second same quality polarizer was set just before

the PMT to further suppress polarization components of the untagged UOT light that were not absorbed by the crystal. These and the non-polarizing beamsplitter were the main etendue limits in our setup, as will be discussed in more detail later. Two cascaded bandpass filters (Chroma HQ585/42 and HQ605/10), efficiently blocked non-resonant fluorescence [90,113] and room light noise. Resonant fluorescence was not found to be a problem, presumably because it was largely converted to non-resonance fluorescence before exiting the crystal. This can be explained as due to the large optical depth of the crystal (more than 30 dB) causing fluorescence, most of which was emitted at the input end of the crystal, to be reabsorbed and re-emitted many times before reaching the output end of the crystal. Since each absorption/emission cycle converts an ever larger fraction of the resonant fluorescence to non-resonant fluorescence, (Debye-Waller-Factors[144]), essentially no resonant fluorescence would be expected at the crystal output.

2. Experiment Details: Operation

Each experimental cycle started with a hole erasing/initialization pulse sequence, as shown in Fig. 5.2. Purpose of this part sequence was two-fold. One, to prevent the spectral hole from broadened after a long excitation time, and two, to enhance the on/off ratio of the spectral hole by increasing absorption. Hole broadening in PSHB materials can happen due to laser long-term drift (in our case ~1 kHz/s[143]) or continued off resonance excitation of ions that are far from the central hole that eventually causes them to become transparent. The erasing pulses pump the ions back into an absorbing state at

the frequency of interest. In fact by pumping the ions into particular initial state we maximize the optical absorption.

In a typical experiment we intended to prepare a spectral filter that is transparent from -0.5 MHz to 0.5 MHz, relative to the UOT tagged light frequency. To do this the erasing sequence is as follows: 1) chirp the laser from 16 MHz to 20 MHz for t_{E1}(~300 μs) and wait for t_{E2} (~500 μs, roughly 3 times optical T_1, or long enough for excited state population relaxation); 2) chirp from -16 MHz to -20 MHz, with erasing and waiting time the same as in step 1); 3) repeat 1) and 2) many times, but each time increase the erasing frequency outward away from the central frequency by a step of 4 MHz, so that the there is no spectral overlap between consecutive pulses. For example, the second repetition would chirp from 20 MHz to 24 MHz and -24 MHz to -20 MHz. This was repeated until finally total frequency range spanned by the erasing pulses was -40 MHz to -16 MHz and 16 MHz to 40 MHz. 4) repeat the previous sets of erasing pulses, as described in 1), 2), 3), typically 150 times. During the erasing pulses the laser frequency was not swept linearly with time but instead as a complex hyperbolic secant, or *sechyp* scan. This special type of chirped pulse optimizes population transfer efficiency and keeps unwanted excitations to a minimum[145]. More details about pulse shape in this work can be found in ref [146]. We did not use a continuous chirp from 16 MHz to 40 MHz, because the ions need time to relax from the excited state between excitations cycles in order to achieve efficient ground state population redistribution.

The second step was to burn the hole for spectral filtering of the tagged light. The bandwidth of this optical bandpass filter should be broad enough to cover the bandwidth

of US modulation sideband. For 5 cycles of 2.3 MHz US, this bandwidth is approximately 0.8 MHz. Additionally a broader spectral hole has a higher passband transmission in general, owing to smaller absorption from Lorentzian tails of off-resonance ions[147], and so too narrow a spectral hole is not recommended. At the same time a wide spectral hole, comparable to the US frequency, should be avoided since then the filter would not be able to separate the tagged from untagged light. In this experiment we found the optimum spectral hole width was 1MHz, and this was burned with ~80 μs pulses (t_{B1} in Fig. 5.2), consecutive pulse separations of ~500 μs (t_{B2} in Fig. 5.2), and repeated ~2000 times. During each pulse the laser frequency was scanned ~1 MHz as a *sech* function of time. To make a symmetric spectral hole, the scanning direction was flipped for every other burning pulse, i.e. -0.5 MHz to +0.5 MHz then +0.5 MHz to -0.5 MHz and so on.

The final stage in the experiment was to perform the UOT. Here the laser frequency was shifted to -2.3 MHz so that the tagged light from the upper US modulation sideband was centered inside the spectral hole. The UOT probing pulses were super Gaussian shape (to insure a plateau of optical power for UOT signal probing) in time, of order 3 and full width half maximum (FWHM) 100 μs (t_{P1} in Fig. 5.2). The smooth edge of the Gaussian pulse reduced the amount of unwanted carrier (untagged light) power spilled inside spectral hole. The spacing between probing pulses t_{P1} was 5 ms. Although the spectral hole lifetime was expected to be minutes[90] in the dark at our operating temperature of ~5K, light scattered from the tissue during UOT can gradually fill it in. To estimate this we illuminated a 2.5 cm tissue phantom with laser light tuned

to the spectral hole center and found that after 50 times probing cycles (~300 ms total) the spectral hole decayed to 75% of its initial depth. Of course the tagged light is much weaker and so the hole lifetime would be much longer during the actual UOT experiment. Nonetheless we reset the spectral hole every 1 second.

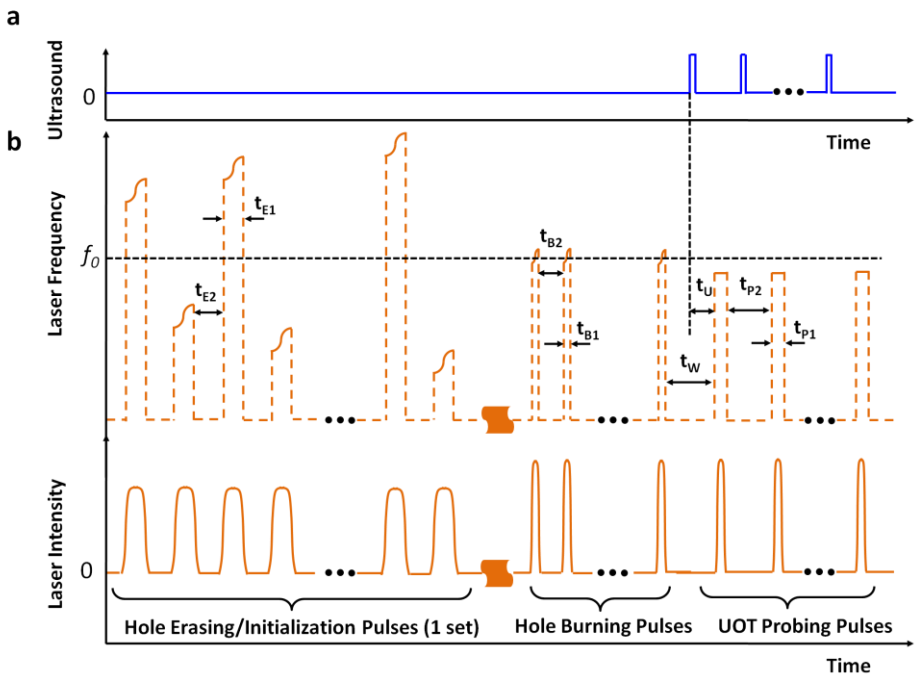

Figure 5.2 | Experimental pulse sequence. a, Pulsed US sequence. **b**, Laser pulse sequence. t_{E1}, 4MHz hole erasing pulse duration; t_{E2}, waiting time between consecutive erasing pulses; t_{B1}, 1MHz spectral hole burning pulse duration; t_{B2}, waiting period between consecutive burning pulses; t_W, waiting period between the end of burning pulses and the beginning of UOT probing pulses; both erasing and burning pulses are *sechyp* scan; t_{P1}, duration for each UOT probing pulse; t_{P2}, time spacing for different probing events; probing pulses are constant in frequency but Gaussian shape in time; t_U, advanced time for triggering US. Figure is for illustration purpose and not in scale.

3. Experiment Details: Hole-Burning Performance

With the above preparation procedure, we could efficiently create a 1MHz wide 'top-hat' shaped spectral hole. Inside the burned hole the absorption was smaller than 3 dB, but 2.3MHz away from the center it was more than 40 dB when measured with a collimated laser beam and 33dB when measured with highly scattered light respectively. Less absorption for diffuse light than plane wave may result from imperfection of our polarizer and polarization sensitivity of the material (Pr:YSO) we are using. Thus in all the on/off ratio was ~30 dB for highly scattered light. Here this ratio is defined as the log of the residual untagged light transmission, $\alpha(f_0)L$, minus the log of the transmission of the tagged light, $\alpha(f_0+f_a)L$, expressed in dB. Here α denotes material absorption coefficient at the corresponding frequency, L crystal length, f_0 is the optical carrier frequency and f_a is the ultrasound frequency.

C. Results and Discussion

1. Imaging with PSHB UOT

To record a 2D UOT image, a tissue phantom sample of size ($x \times y \times z$) = ($45\times70\times70$ mm^3) was used. The sample was made from a 10% porcine skin gelatine with 1% Intralipid solution, and had a reduced scattering coefficient $\mu_s' \approx 10\,\text{cm}^{-1}$. It was set on a translation stage and scanned in *y*-direction a range of 2 cm to produce an image in

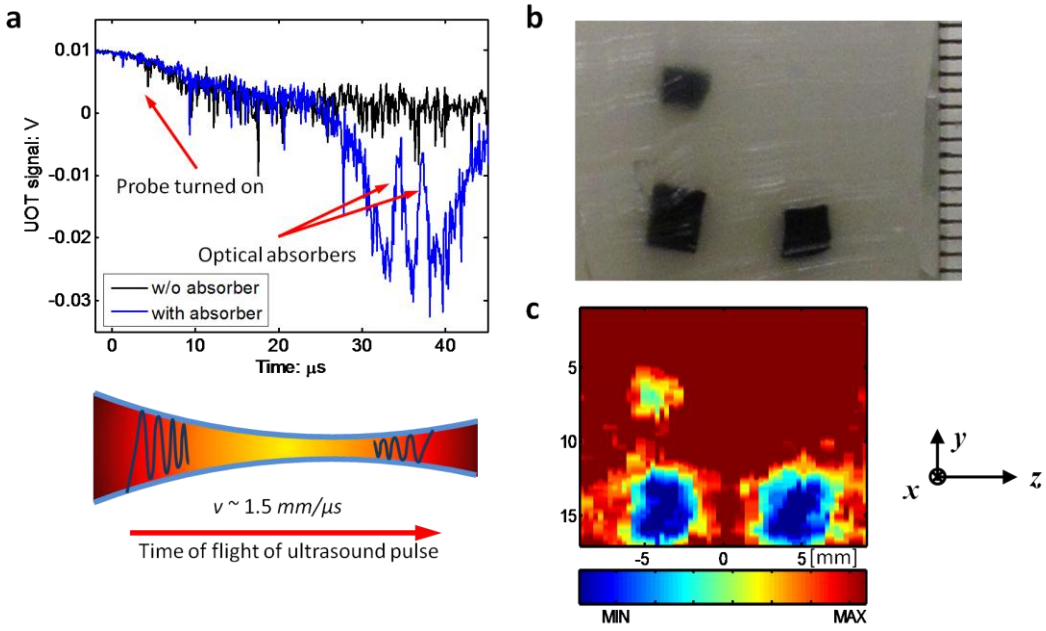

Figure 5.3 | Typical UOT signal and 2D image. a, Typical temporal dependence of the UOT signal during the propagation of an US pulse through the sample. Black trace in plot shows "untagged" photons leakage background; blue traces corresponds to "tagged" photons for diffuse light which carries optical information (absorption in this scenario) from tissue phantom. **b**, Photograph of the optical absorbers buried inside the tissue phantom. **c**, UOT for (**b**) with 50 times accumulation, interpolated and median filtered. Bottom-right inset: lab coordinates.

the *y*, *z* plane, where the acoustic pulse propagated in *z* direction. Each one-dimensional (1D) *z*-line (A-scan) of the image was averaged 50~100 times, for each US transverse position (*y* direction). Two-dimensional (2D) tomogram (B-mode) was achieved by scanning in *y* direction. The US source was 5 cycles of 2.3 MHz (peak pressure of ~4 MPa and mechanical index of 1.9 which is within US safety limit[125]) is generated from a spherically focused piezoelectric transducer (A395S-SU by Panametrics) with 1.5 inch diameter and 75mm focal length. A typical UOT temporal profile along z direction (A-scan) is shown in Fig. 5.3a. The signal to background ratio (SBR) was more than 3 and

signal to noise ratio (SNR) was around 7, high enough to reliably identify an object (known as Rose's Criterion [148]) . The lateral resolution was determined by US focal width, ~2 mm in our case. The axial resolution was directly related to 5 cycle US pulse length, which was shorter than 3 mm.

Three optical absorbers, as shown in Fig. 5.3b, buried inside were dyed with black Indian ink, They had sizes of $x \times y \times z = 4\times2\times2$ mm^3, $4\times3\times3$ mm^3 and $4\times3\times3$ mm^3. In B-mode tomogram Fig. 5.3c, these 3 absorbers were clearly imaged. For the large object the image contrast was bigger than 80%. For the smaller object (~2 mm) in the upper left side the contrast decreased to 50%, so the resolution limit is just under this[23].

To test the maximum depth for UOT imaging a phantom sample with a thickness of 9cm in the *x* direction was used. For a 5 cycle pulse of 2.3 MHz US modulation, the observed signal to background ratio (SBR) was 2 and signal to noise ratio (SNR) was 4 when averaging 500 pulses. In Fig. 5.4, modulation depth (MD, defined as ration between intensity of first order modulation side over carrier), measured using CW ultrasound (typical signal as shown in Fig. 5.4a), is plotted as a function of sample thickness (Fig. 5.4b). As seen the modulation depth does not change for samples thicker than a couple cm, as expected [57]. In Fig. 5.4c, the UOT signal is plotted versus sample thickness. As seen this decreases exponentially with increasing thickness. In Fig. 5.4d, the observed UOT SNR is plotted vs sample thickness (green squares), along with a shot noise estimate (yellow circles) calculated from the measured signal voltage and detector

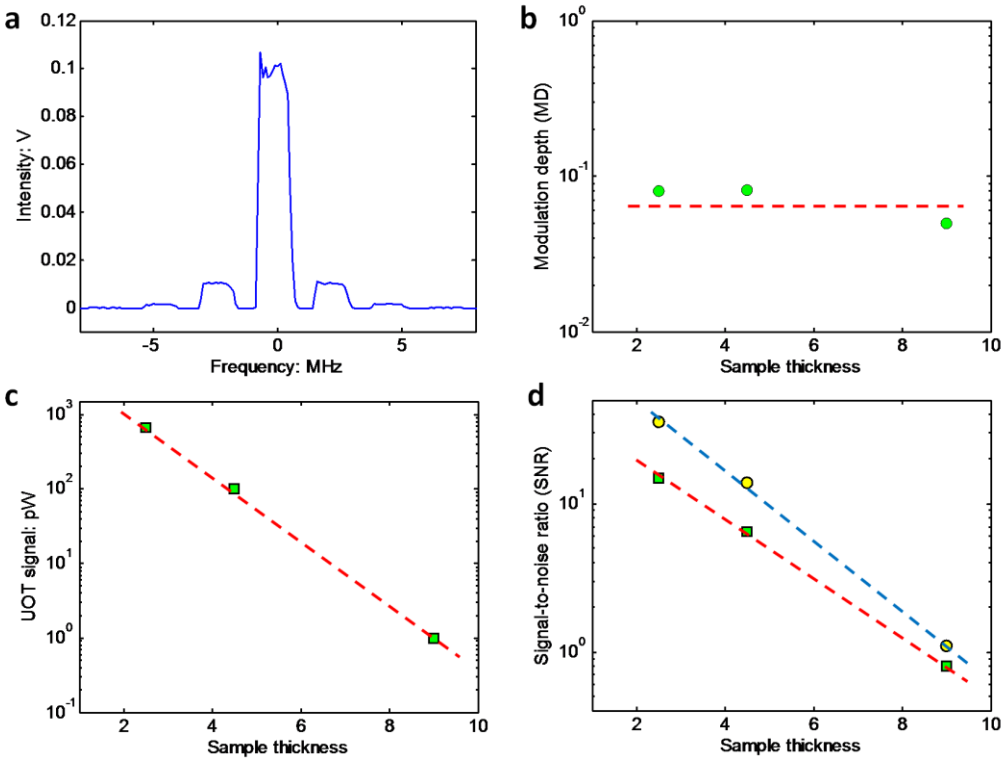

Figure 5.4 | UOT signal analysis. a, Intensity spectra of CW ultrasound modulated light measured with signal through spectral hole (prepared beforehand) by laser frequency chirping. **b**, Modulation depth (CW ultrasound with relatively high pressure) changes with tissue phantom thickness. Green circles show measurement for modulation depth, which is fairly close to a constant (as illustrated by dashed red line). **c**, UOT signal dependence of tissue phantom sample thickness. Green squares are experimental data and dashed red line is exponential fit. **d**, Signal-to-noise ratio (SNR) vs. sample thickness. Green squares are measurements and yellow circles correspond to shot noise theoretical estimates.

specifications (detector quantum efficiency ~8%, detection bandwidth ~1 MHz, PMT gain $G \geq 3\times10^5$, gain excess noise factor F ~ 1.3).The experimental SNR is normalized to a 20 trace average, which was the number of averages used for the thinner tissue samples. As can be seen the SNR is within a factor of 2 of shot noise over a wide range of thicknesses and for the thickness samples becomes very close to shot noise limited. This is as expected because weaker signals have a greater relative contribution of shot

noise. For the 9 cm sample the detected modulation sideband power was only ~1 pW or roughly 3 Mcts/s in photon counting mode. Ordinarily we would have expected to reach the shot noise limit in the 9 cm tissue however our photomultiplier did not have electronic discriminator to digitally remove excess noise. For thinner tissue samples the departure from shot noise could have been due to imperfect flatness inside the spectral hole.

We also examined the UOT signal in real tissue, a 3.5 cm thick chicken breast, not shown. In this case the SBR was 2, the SNR was 5, and the modulation sideband power was 2 pW. This poor performance in real tissue was expected because of the relatively high optical absorption of 605 nm light in biological tissue. If we had used a longer wavelength for example the 798 nm Tm:YAG wavelength, the performance with real tissue and phantoms would have been much closer. In fact at 1.06 μm both real tissue and phantoms showed similar signal strengths in recent work [127].

2. Discussion and Projections

It is the main point of the chapter to make projections as to the maximum tissue thickness for which UOT imaging is possible for the most successful techniques reported so far. Because these UOT experiments are done under different experimental conditions, for example different strength illumination lasers, different *etendue*, different US pulse lengths, and different numbers of traces averaged it is important to normalize the data in some way. Then, by using the observed dependence of UOT tagged light power vs tissue thickness in Fig. 5.4c, we can make realistic projections as to the

ultimate tissue thickness that can be imaged with UOT. To do this we normalize to the case of single shot imaging (no averages), an SNR of 10, an illumination laser intensity equal to the safety limit, and the maximum *etendue* that can be straightforwardly achieved with the technique used. The resulting projections are shown in Table 5.1. As can be seen, the maximum UOT imaging depth is 18 cm for PSHB.

Here we chose the normalizing case of single shot readout for each image line so that video rate images may be obtained. The SNR of 10 was chosen, although 5 is the minimum required, in order to allow for lower contrast cases. SNR projections were made by assuming the best possible case which is shot noise limited. The maximum illumination intensity, which depends on the wavelength used assumed laser pulses of 20 μs length and a repetition rate of 30 video lines/s. Here we acknowledge that often it is

Table 5.1 | Summary comparison of projected performance of leading UOT techniques. I_{max}, safety allowed maximum laser intensity[134]; $I_{current}$, reported laser intensity used in corresponding technique; G_{max}, maximum possible *entendue*; $R_{on/off}$, on/off ratio to characterize frequency discrimination capability; $D_{achieved}$, reported maximum imaging depth; $D_{single\text{-}shot}$, projected single-shot imaging depth. Data for Fabry-Perot (FP) approach are from Rousseau *et al*.[127]; We adopt parameters mainly from publication by Farahi et *al*.[149] for photorefractive (PR) detection method, except *etendue* estimate is from our work[54]. Notice there is 'untagged' photons suppression in PR method.

	I_{max} (kW)	$I_{current}$ (kW)	G_{max} (sr mm^2)	$R_{on/off}$ (dB)	$D_{achieved}$ (cm)	$D_{single\text{-}shot}$ (cm)
FP (1064 nm)	11.8	1.3	0.38	18	6	3
PR (790 nm)	3.6	0.00024	3	0	2.3	7
PSHB (606 nm)	2.4	0.0001	560	30 (140)	9	18

preferred to operate well below the safety limit, typically 10 times lower, due to strong heating at the safety limit. In this case the depth estimates should be derated appropriately 2cm according to Fig. 5.4c. For the maximum *etendue* of the techniques used, we chose the following: 1) for the FP technique we used the value given in the most recent work [127] as FP *etendue* depends on finesse which in turn controls filtering capability, and this tradeoff appeared optimized in the work. 2) for the PR technique we estimated maximum *etendue* based on our own measurements of the angular bandwidth of two-wave mixing in typical PR crystals[54]. 3) for the PSHB technique we assumed a 2 cm × 2 cm square crystal face and a 5cm diameter active area PMT, although significantly larger dimensions could be manufactured. Details of the current *etendue* limit in our experiment and the *etendue*-optimized design are shown below.

Because of the importance of *etendue* in UOT, we now give a detailed analysis of the limitations in our current setup and discuss the feasibility of straightforward improvements. *Etendue* limits for various components in the current setup are illustrated in Fig. 5.5 and listed in Table 5.2.

From Table 5.2, it is clear that the beam splitter used to bring in the erase/burning pulses is the main bottle neck for *etendue*. To eliminate this we plan to use side excitation for erasing and burning[140], thereby making this beamsplitter unnecessary. For the crystal itself *etendue* is unlimited because the refractive index of YSO (and also YAG) are large enough that a crystal with sides and at right angles to the end faces will From Table 5.2, it is clear that the beam splitter used to bring in the erase/burning pulses is the main bottle neck for *etendue*. To eliminate this we plan to use side excitation for

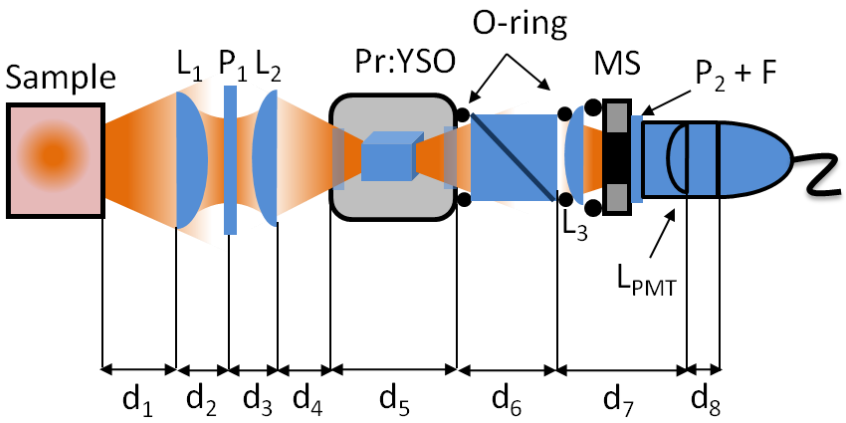

Figure 5.5 | *Etendue* estimation. $d_{1\sim8}$, distance between optical elements; $L_{1\sim3}$, lens; $P_{1\sim2}$, polarizer; F, fluorescence filter; $d_{1\sim8}$: 45, 25, 25, 30, 50, 40, 60, 40 respectively, unit: mm.

erasing and burning[140], thereby making this beamsplitter unnecessary. For the crystal itself *etendue* is unlimited because the refractive index of YSO (and also YAG) are large enough that a crystal with sides and at right angles to the end faces will trap any light incident on the input face and guide it to the output face via total internal reflection. The cryostat *etendue* can be made larger using large diameter windows on the UOT entrance and exit faces, as in some microscope cryostat designs (up to NA of 0.75 reported so far[150]). Here we choose a conservative numerical aperture (NA) of 0.7 for the cryostat. To eliminate the *etendue* limit of the polarizers, the single crystal of Pr:YSO we currently use can be replaced by two cross polarized Pr:YSO crystals back to back (Tm:YAG does not have the polarization problem). Lenses can have very large diameters and still be economical and so do not limit *etendue*. This leaves the active area of the PMT which we assume to be 5cm diameter. Since this is larger than the crystal

Table 5.2 | *Etendue* of elements in light path. *Etendue* characterizes system light collection efficiency and the smallest *etendue* determines the system performance. Except for the sample side, in all the other situations, *etendue* calculation is based on the product of current element surface area (in the right side as shown in Fig. 5.5) and solid angle when looking from the current component to the previous one.

	***S*, component area (mm^2)**	***Ω*, solid angle (sr)**	***G, Etendue*** ($sr\ mm^2$)
Sample side	$\pi*(25)^2 \sim 2{,}000$	2π	12,500
Lens L_1	$\pi*(25)^2 \sim 2{,}000$	0.8	1,600
Lens L_1 and L_2	$\pi*(25)^2 \sim 2{,}000$	0.66	1,300
Lens L_2 and Pr:YSO	$\pi*(3)^2 \sim 28$	1	28
Crystal geometry	$\pi*(3)^2 \sim 28$	0.66	18.5
Beam splitter	$\pi*(12.5)^2 \sim 490$	0.008	3.9
Lens L_3 and L_{PMT}	$\pi*(12.5)^2 \sim 490$	0.13	65
L_{PMT} and PMT head	$8\times24 \sim 192$	0.29	55

diameter it does not limit *etendue*. Assuming a tissue area light collection area of 10cm diameter, for imaging ~10cm deep into the tissue, this also does not limit etendue since it is larger than the crystal entrance face. Therefore at present, the limiting *etendue* is the NA of the cryostat window and the crystal diameter. To improve *etendue* more it may be possible to grow a larger crystal or possibly replace the single crystal with a Pr:YSO (or Tm:YAG) powder[151]. The fact that powders scatter light is not important since we are filtering highly diffuse light, and in fact the powder should also eliminate the polarization problem for Pr:YSO.

D. Summary

In summary in this chapter it has been shown that we can efficiently detect the UOT signal from a 5 cycle acoustic pulses in a 9 cm thick tissue phantom. The current *etendue* was 3.9 and the frequency discrimination was 30 dB. Using a high power pulsed laser such as in ref [127], we project a factor of 155 SNR improvement assuming shot noise limited detection, but not including *etendue* improvements. Based on our measured UOT signal strength vs tissue depth, we project deep tissue imaging down to 18 cm with improved *etendue* and higher laser power.

Here we point out that our 30 dB on/off ratio with scattered light and more than 40 dB with a collimated beam is still far less than the 140 dB demonstrated with Pr:YSO. This high performance was achieved by using a long crystal that was pumped from the side to burn and shape the spectral feature. Since our *etendue* is independent of crystal length, owing to the total internal reflection in YSO, this same result could be achieved for UOT filtering so that even deeper tissue imaging, or lower tissue illumination intensity, or higher ultrasound frequency (for higher resolution) modulation might be possible.

Finally although we were forced to use tissue phantoms, due to strong absorption of our 607 nm laser light by real tissue, PSHB crystals with similar performance exist that operate within the therapeutic window. For example Tm:YAG operates at 790 nm and with a magnetic field applied exhibits persistent hole burning. Though the optical absorption is weaker in Tm:YAG, a longer crystal can be used to compensate, since crystal length also does not affect *etendue* for YAG. Thus, we expect our performance

numbers to carry directly over to real tissue samples, for example chicken breast. Also the availability of higher power semiconductor lasers near 790 nm and the relative ease of frequency stabilizing them, means that we should be able to approach our 18cm projection for imaging in real tissue.

CHAPTER VI

UOT USING SLOW LIGHT WITH PERSISTENT SPECTRAL HOLE BURNING

A. Statement of Problem for UOT with PSHB and Slow Light Solution

1. PSHB UOT Polarization Residue Problem

The first SHB demonstrations of UOT imaging were limited to only about 14 dB of discrimination for scattered light[135] (also described in chapter IV). However, a recent demonstration with a persistent hole burning (PSHB) material Pr^{3+}:Y_2SiO_5 (Pr:YSO) showed better than 30dB discrimination (as in chapter V). Here the difference between SHB and PSHB materials is the amount of time the spectral filter lasts, or persists, after preparation. Longer persistence times allow more-selective filters to be engraved in the PSHB material[140]. In Pr:YSO this persistence time is minutes, compared to 10 ms with Tm^{3+}:$Y_3Al_5O_{12}$ (Tm:YAG). This 30 dB discrimination with diffuse light was enough to demonstrate detection of UOT tagged light in a 9 cm thick tissue phantom. However the performance of this Pr:YSO filter using diffuse light (30 dB) was found to be more than 10 times worse than that using laser beams (>40 dB). The poorer filtering performance with diffuse light was attributed to polarization sensitivity of the Pr:YSO transition as well as scattered light leaking around the crystal[1]. The polarization sensitivity of Pr:YSO also necessitated the incorporation of additional polarizers in the detection path, limiting the *etendue*. Thus if this residual leakage of untagged light could be suppressed by a means other than polarization, better filter discrimination as well as better *etendue* would be achievable, and deeper tissue UOT would be possible.

2. Slow Light Based on PSHB UOT

In this chapter, we report the use of slow light in Pr^{3+}:Y_2SiO_5 (Pr:YSO) to achieve significant additional frequency discrimination between tagged and untagged scattered light in UOT . The phenomenon of slow light has ignited keen interest in the past decade because of the successes in early demonstrations of very slowly propagating[152] and even stopped light [153]. Soon after these demonstrations, slow light was achieved in a solid using Pr:YSO[118]. Since then slow light has been explored for numerous applications such as optical information storage, controllable optical delay lines, high-precision spectroscopy, radar beam steering and *etc.*[154]. Finally, slow light in Pr:YSO was recently used to suppress the Pr:YSO polarization leakage for quantum memory applications[155]. However most of these applications are implemented by slowing a well-collimated beam. Our work is the first time that slow light has been observed with highly diffusive light such as that emerging from thick, soft biological tissue.

In our experiment, a spectral filter was first prepared in a Pr:YSO crystal and then used to filter out the tagged light produced by the ultrasound-tissue interaction. To do this the transmission passband of the filter was centered on one sideband of the ultrasound modulated light (red part in Fig. 6.1b), while keeping the fundamental or carrier frequency outside the spectral window (blue part in Fig. 6.1b). If the spectral window has a sufficiently sharp refractive index dispersion, the transmitted sideband will be time delayed due to slow light, as shown by the red part on the right side of Fig. 6.1b. However light with the wrong polarization to interact with the Pr ions in the

crystal, or light scattered around the crystal is not slowed (blue part on right side of Fig. 6.1b). Hence an additional degree of light discrimination based on time of arrival is possible. Here we note that it is also desirable to have enough transmission bandwidth to cover the spectral width of the modulation sideband in order to prevent time distortion of the signal which otherwise would degrade the UOT imaging quality.

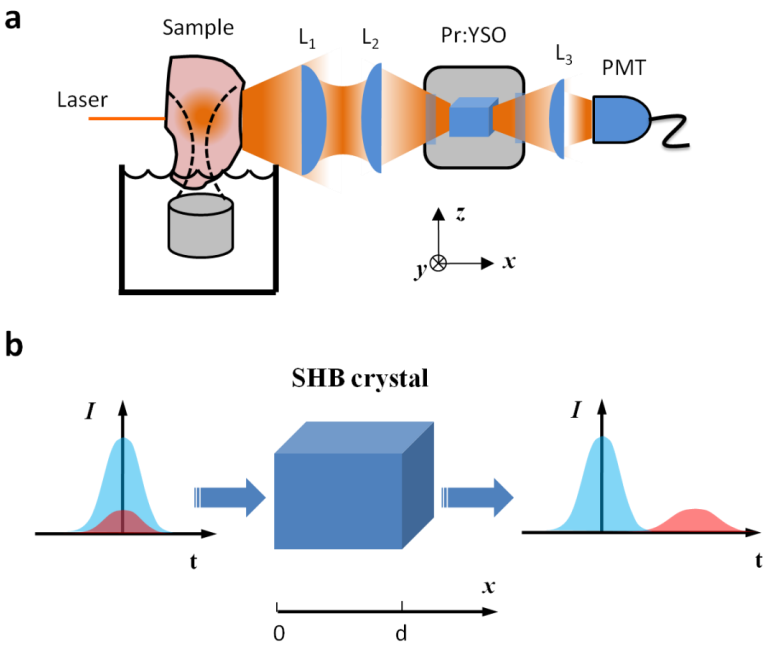

Figure 6.1 | Experimental setup and slow light working mechanism illustration. **a**, Simplified experimental setup schematics. **b**, Slow light UOT: blue Gaussian profile corresponds to 'untagged' light with frequency outside spectral hole; red profile corresponds to 'tagged' light and its frequency centers around spectral hole.

B. Time-Delay Bandwidth Product Analysis: Theory and Experiment

1. Theory about Slow Light

To determine the slow light properties of the crystal, the amplitude and phase responses are needed.

$$E_{out}(\omega) = G(\omega) E_{prob}(\omega), \tag{6.1}$$

where $E_{prob}(\omega)$ is the frequency domain amplitude of the probe field, in our case a Gaussian pulse with 1 μs full-width half maximum (FWHM)

$$I_{prob}(0,t) = I_0 \exp\left[-(t/\tau)^2\right],\ \tau = \frac{1}{2\sqrt{\ln(2)}}\mu s, \tag{6.2}$$

$$E_{prob}(0,t) = E_0 \exp\left[-(t/\tau)^2/2\right], E_0 = \sqrt{I_0} \tag{6.3}$$

$$E_{prob}(\omega) = \frac{1}{2\pi}\int E_{prob}(t') e^{-i\omega t'} dt', \tag{6.4}$$

and $G(\omega)$ is the complex frequency domain amplitude response function

$$G(\omega) = \sqrt{T(\omega)} e^{i\Delta\varphi(\omega)}, \tag{6.5}$$

If the intensity transmission spectrum is known, the phase of the response function can be calculated from the Hilbert transformation (so-called Hilbert phase):

$$\Delta\varphi(\omega) = \frac{1}{\pi}\int_{-\infty}^{\infty} \frac{\ln\sqrt{T(\omega')}}{\omega - \omega'} d\omega'. \tag{6.6}$$

The last formula is equivalent to Kramers-Krönig relation as discussed in[156] and is quite straightforward to implement numerically to estimate the slow light effect for an arbitrary spectral hole shape.

Fig. 6.2 shows the amplitude response functions for several different spectral hole filters used in our experiment along with the spectrum of the Gaussian input pulse used to illuminate the tissue sample. Here red, green and blue correspond to the transmission spectra $\sqrt{T(\omega)}$ for spectral hole burned with 1 MHz, 500 kHz and 250 kHz scanning respectively, and the black curve is the Gaussian pulse spectrum. As can be seen only the 1 MHz spectral hole passes the entire spectrum of the Gaussian pulse. However the group delay time (or light speed), which is related to the slope of the Hilbert phase $\Delta\varphi(\omega)$, calculated with equation (6.6) (circles in Fig. 6.2) is greatest for the narrowest spectral hole. This time-bandwidth tradeoff is familiar in slow light and is optimized by using an optically thick material.

Time domain intensity profile at the output of the Pr:YSO crystal was calculated by:

$$I(t) = \left|E_{out}(t)\right|^2 = \left|\int E_{in}(\omega) G(\omega) e^{i\omega t} d\omega\right|^2, \tag{6.7}$$

Fig. 6.3 shows this calculated time response for the spectral holes in Fig. 6.2, using the same color coding (red for 1 MHz, green for 500 kHz, and blue for 250 kHz). Again the black curve corresponds to the Gaussian input pulse.

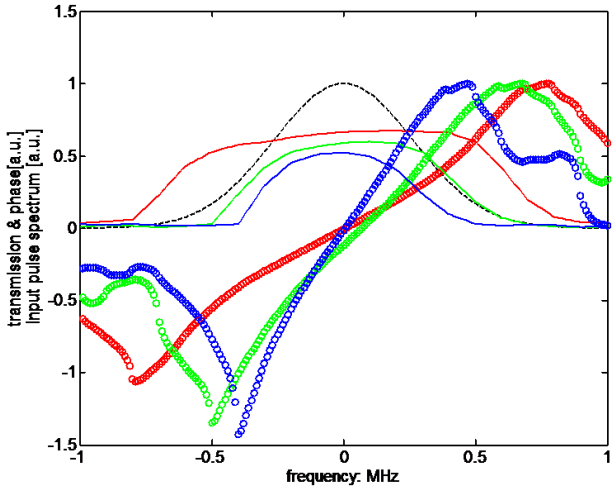

Figure 6.2 | Spectral hole shape and corresponding phase change. Black dashed line, amplitude spectrum of input Gaussian pulse; red, green and blue lines correspond to transmission spectrum of spectral hole burning for 1 MHz, 500 kHz and 250 kHz respectively; red, green and blue circles correspond to phase change over frequency with 1 MHz, 500 kHz and 250 kHz burning.

2. Compare Slow Light Theory to Experiment

To verify that these calculated slow light delays are correct for diffuse light we performed an experiment, as illustrated in Fig. 6.1a. Here, diffuse light was generated by back-illuminating a sample (opposite side of the PSHB crystal) with laser light and the scattered light emerging from the front of the sample was directed through a Pr:YSO crystal into a photomultiplier (PMT) detector. Prior to the light slowing experiments, spectral holes were engraved into the Pr:YSO crystal using pulse sequences similar to those by different group[102,157]. In particular these spectral holes were burned using a very slow scanning speed (10 kHz/μs) to avoid coherent radiation[158]. The resulting spectral hole transmission profiles are the actual traces shown in Fig. 6.2. The sample used to generate

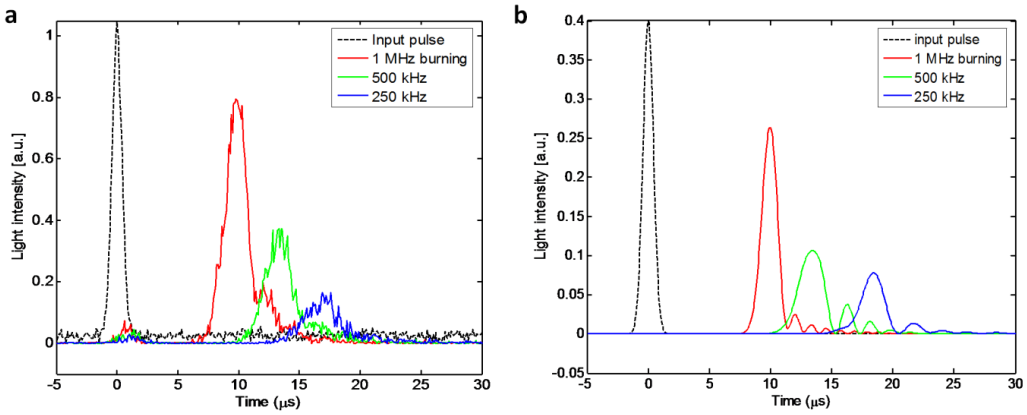

Figure 6.3 | Slow light effect with PSHB. a, Experimental data for 1 μs FWHM Gaussian pulse propagation through spectral holes burned with 1 MHz, 500 kHz and 250 kHz chirping. **b**, Numerical simulation for Gaussian input pulse delay with different hole burning width.

diffused light is a tissue phantom of dimensions ($x \times y \times z$ = 25×70×70 mm^3) where x is along the light propagation direction. It is made from 10% porcine skin gelatin and 1% Intralipid (reduced scattering coefficient μ_s' = 10 cm^{-1}). The diffuse light emerging from this phantom was then directed into the Pr:YSO SHB crystal with dimensions ($x \times y \times z$ = 12×10×10 mm^3), and the resulting slowed light was detected with the PMT.

The slowing of diffused light is shown in Fig. 6.3a. As seen, there is good agreement between these experimental delays and the simulation results in Fig. 6.3b. After passing through the crystal, the Gaussian pulse spread increased from 1 μs FWHM to ~2 μs FWHM even for the longest 17 μs delay, meaning this slowing technique can be used to make UOT images with minimal distortion. Note that the 'time-delay bandwidth product' is large in Fig. 6.3 (up to 7), as expected based on the ~33 dB optical depth of the crystal[159].

3. UOT Signal Bandwidth Estimate

In UOT experiment, the optical illumination should be matched to the ultrasound pulse duration to minimize laser exposure. To this end Fig. 6.4 shows the bandwidth calculation for a 2-cycle ultrasound pulse at an ultrasound frequency of 2.3MHz. The ultrasound pulse temporal shape is shown in Fig. 6.4a. The sound pressure amplitude spectrum produced by this pulse is shown in Fig. 6.4b. As can be seen the 2-cycle pulse gives a sound pressure bandwidth of 1.6 MHz FWHM. The spectrum of the ultrasound modulated light is close to that of the ultrasound pressure except the peak is slightly shifted (<10%) toward lower frequencies, but the linewidth is nearly unchanged [160].

To ensure a linear response between UOT signal and its corresponding slow down part, the illumination pulse was chosen to be much longer than the 2-cycle ultrasound pulse because of limited time-delay bandwidth product. Of course in actual applications, these could be more closely matched to reduce laser exposure. In particular we chose a 10 μs FWHM super-Gaussian pulse (of order 3). This illumination pulse has a ~80 kHz bandwidth and is therefore negligible.

Fig. 6.5 shows UOT signals for 2-cycle ultrasound pulses filtered through different spectral hole widths including the same as used above (red, green , blue) = (1 MHz, 500 kHz, 250 kHz) and an additional spectral hole width of 100 kHz (pink curve). As before, the black curve shows the super-Gaussian input pulse. A new curve, the light blue curve shows the UOT signal when no ultrasound is applied. This is the first key result of this chapter. From this blue curve it is seen that there is considerable light leakage during the on-time of the illumination pulse. However at later times, when the

delayed UOT signals appear (for example the pink one corresponding to 100 kHz hole burning), there is negligible background noise. Thus slow light has successfully eliminated the loss of filter discrimination due to polarization leakage and any other light leakage.

Also from Fig. 6.5 it is seen that the narrower spectral hole gives more delay for the UOT signal but at the expense of lower transmission. This is in agreement with other slow light experiments. Here we note that even though the light and ultrasound pulses were synchronized, the ultrasound had to propagate a distance of ~7 cm from the transducer to the focus. Assuming a sound speed in water is 1.5 mm/μs, the ultrasound pulse reaches its focus with a delay of 47 μs. This time delay was built into the trigger pulse for the laser illumination so that the ultrasound arrived at the center of the laser illumination pulse.

C. Slow Light UOT Experiment

To demonstrate the use of this diffuse slow light for deep tissue UOT imaging, we used a thicker tissue phantom sample (45×70×70 mm^3 along the *x, y* and *z* axes, reduced scattering coefficient $\mu_s' = 10\ cm^{-1}$) buried with jellified black Indian ink of size ($x \times y \times z = 40 \times 35 \times 35\ mm^3$). This time 5 cycles of ultrasound (US) pulses were used (corresponding to 0.8 MHz FWHM bandwidth, with a peak pressure of ~4 MPa at the focus, and mechanical index of 1.9, which is within the US safety limit[125]). Here the spectral hole burning width was 200 kHz which optimized the tradeoff of signal loss and background suppression as expected from discussion based on Fig. 6.5.

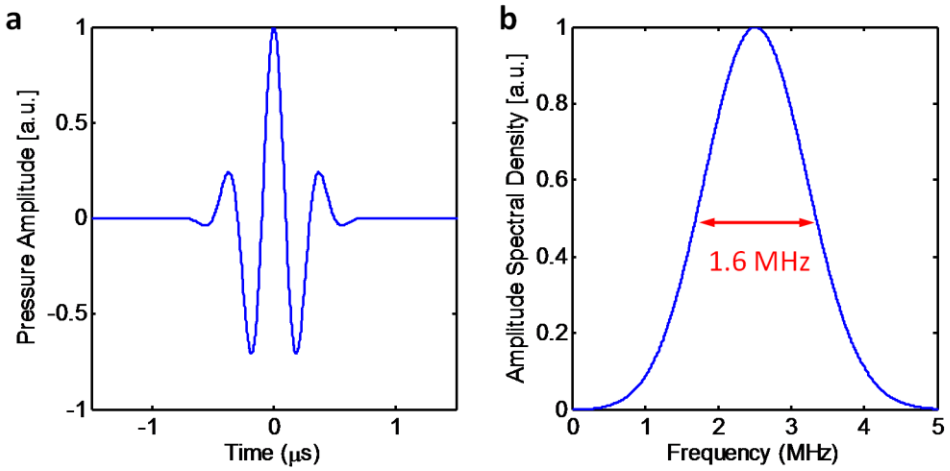

Figure 6.4 | Ultrasound pulse spectral density analysis. **a**, Temporal profile of the 2-cycle ultrasound pulse. **b**, Amplitude spectral density of the ultrasound pressure (1.6 MHz FWHM) calculated from (a).

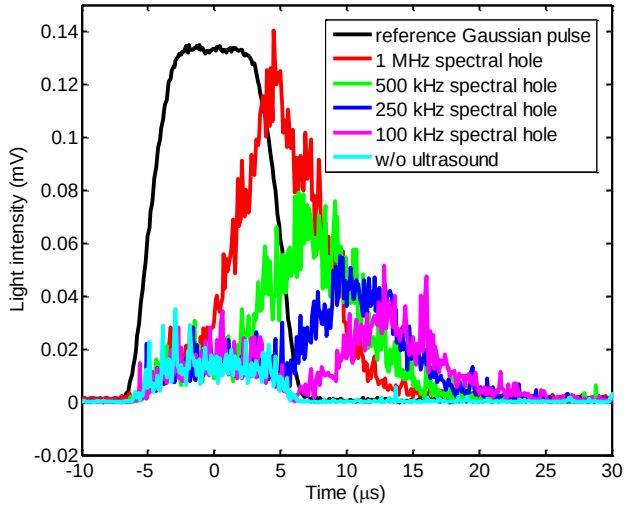

Figure 6.5 | Slow down of UOT signal from 'untagged' light residue with different width of hole burning.

Fig. 6.6 shows an A-scan image for this sample, which is a time domain trace of the UOT signal filtered through the spectral hole in the Pr:YSO crystal. The blue trace is without the absorber and the red trace is with the absorber. As seen the absorber

produces a 3 μs FWHM dip in the UOT signal. This corresponds to a 4.5 mm spatial width for the absorber (assuming speed of sound: 1.5 mm/μs), which was quite close to the actual 3.5 mm absorber length. Thus the UOT signal is not significantly degraded by the group delay distortion for the relatively narrow hole width used.

Fig. 6.7a shows the slow light UOT signal with a much thicker phantom sample ($x \times y \times z = 90 \times 100 \times 80$ mm^3). Here the signal-to-noise ratio (SNR) deteriorated because of the small amount of collected light from such a thick tissue sample. However it is clear from comparing the red curve with ultrasound to the blue curve without ultrasound that the delayed UOT signal clearly stands on a zero background. This is the second key result of this chapter. We note that a more sensitive detection method, such as higher quantum efficiency PMT or a photon counting approach, might enhance SNR in the future. Finally, Fig. 6.7b shows a slow light UOT experiment using 3.5 cm thick chicken breast tissue. Again it can be seen that the slow light time delay clearly separates the tagged light signal from the background leakage.

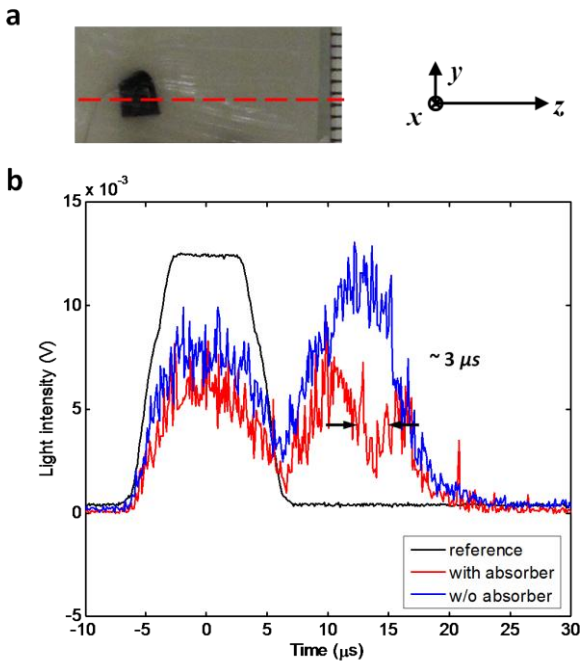

Figure 6.6 | Slow light UOT with optical absorptive features deep inside highly scattering median. **a**, Photography of optical absorbing inclusion inside tissue mimicking phantom. **b**, Black trace, reference signal (from beam sampler without passing through Pr:YSO crystal); blue trace, UOT signal, slowed down inside Pr:YSO, no optical absorber in ultrasound path; red trace, UOT signal slowed down inside Pr:YSO, optical absorber in ultrasound path.

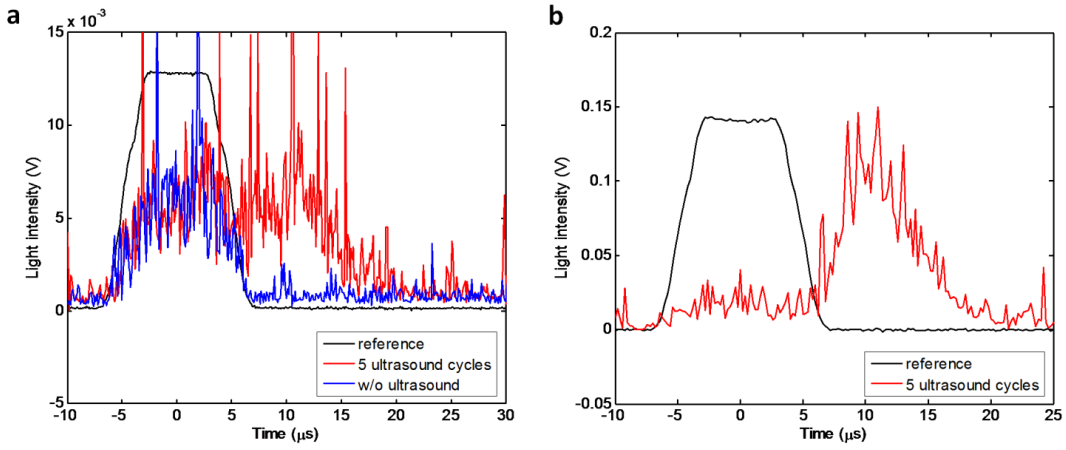

Figure 6.7 | Slow light UOT. **a**, Slow light UOT for 9 cm thick phantom. **b**, Slow light UOT for 3.5 cm thick chicken breast tissue. In both situations, the spectral hole was wider than 200 kHz.

D. Summary

In summary, we have shown that ultrasound-modulated optical tomography (UOT) performed with several cycle (2.3 MHz) ultrasound pulses bursts can significantly benefit from the temporal delay produced by slow light in a PSHB filtering crystal. The slow light gives an additional time-domain isolation of signal from background in addition to the already superior noise rejection capability of the persistent spectral hole burning (PSHB) filter [1]. Proper selection of the spectral hole width is based on a tradeoff between isolation and signal loss and distortion. Moreover for our optically thick PSHB crystal, this tradeoff is favorable even for relatively thick tissue samples: a 90 mm thick phantom and a 35 mm thick chicken breast. Here we note that even though this demonstration was done at 607 nm wavelength, slow light has also been observed in materials that work in the therapeutic window (for example Tm:YAG[157]). Thus slow light may find an application in early cancer detection via UOT.

CHAPTER VII

SUMMARY AND CONCLUSION

In this dissertation, different experimental methods including nonlinear optics and quantum optics approaches have been used to implement ultrasound-modulated optical tomography (UOT). The ultimate goals for these methods are to improve SNR with higher detection sensitivity so that we will have the chance to image really deep inside soft biological tissue still with mm resolution (determined by ultrasound frequency).

We begin with the photorefractive two-wave mixing method, which increases light collection efficiency because of its relative big *etendue* compared to previous methods. Phase change encoded with sound modulation is decoded by photorefractive holography. With this method by time gating the UOT signal, optical information and mechanical information can be separated. To suppress the "untagged" background, a photorefractive four-wave mixing approach has been realized for UOT signal extraction. Signal-to-background ratio can be increased to ~1 with this FWM approach. This has been the best reported result with nonlinear optics methods. Finally an optical novelty filter has been cascaded with the FWM setup to further deplete static scatter noise either from fanning effect in PR polymer or scatter noise in diffuse light path. An additional factor of 10 enhancement of SBR has been achieved.

Because of the relative slow response time of PR materials and inevitable noise from pump the beam, spectral-hole burning method with rare-earth ion doped crystal has

been investigated as a quantum spectral filter for UOT signal detection. After a brief overview of material chemical, physical and optical properties, we introduce SHB in a two-level (simplified) quantum system inside Tm:YAG for UOT application. Calculation shows the possibility to create an efficient spectral filter for "tagged" and "untagged" light separation. 15.6 dB on/off ratio is expected in theory and 14 dB has been realized in experiment where the discrepancy is because of broad laser linewidth and possible spectral diffusion due to the high concentration of Tm ions. Half mm resolution can be achieved with more than 1 cm imaging depth.

To overcome the limited on/off ratio problem in two-level quantum system (because of power broadening), Pr:YSO is chosen for persistent spectral-hole burning UOT. In Pr:YSO, persistent hole can survive longer than 100 s, which gives us enough time to fully deplete resonance ions before spin relaxation. Thus we can have narrow and deep spectral hole as an ideal optical filter. With carefully designed pulse sequence, we are able to create a spectral feature with 1 MHz wide and on/off ratio of more than 40 dB for collimated light but around 30 dB for highly scattered light. With this spectral filter, UOT signal can be distinguished from background noise for as thick as 9 cm tissue phantom and 3.5 cm thick chicken tissue (note the high absorption of chicken tissue in 606 nm). If equipped with a high power laser (still within safety limit), we should be able to image 18 cm deep inside with single shot read-out and video rate line acquisition.

Polarization leakage from PSHB crystal is the major noise source when we go to quite deep into tissue. Slow light can separate "tagged" light from the residual "untagged" background because of optical delay inside spectral hole whereas there is no

delay outside spectral hole. Incorrect polarization will not experience phase dispersion, or slowing, either because there is no interaction between that polarization of light and the ions. Both experiment and theory shows that we have quite good time-delay bandwith product (up to 7) for enough time separation with acceptable signal distortion. Experiments both in tissue phantom and real chicken tissue show that slow light works well for UOT and give us outstanding sensitivity because of elimination of residual background noise (except detector intrinsic dark counts).

REFERENCES

1 Rajadhyaksha, M., Grossman, M., Esterowitz, D., Webb, R. H. & Anderson, R. R. In vivo confocal scanning laser microscopy of human skin: melanin provides strong contrast. *The Journal of Investigative Dermatology* **104**, 946-952 (1995).

2 Denk, W., Strickler, J. H. & Webb, W. W. Two-photon laser scanning fluorescence microscopy. *Science* **248**, 73-76 (1990).

3 Fujimoto, J. G. Optical coherence tomography for ultrahigh resolution in vivo imaging. *Nature Biotechnology* **21**, 1361-1367 (2003).

4 Zhang, H. F., Maslov, K., Stoica, G. & Wang, L. V. Functional photoacoustic microscopy for high-resolution and noninvasive in vivo imaging. *Nature Biotechnology* **24**, 848-851 (2006).

5 Zeff, B. W., White, B. R., Dehghani, H., Schlaggar, B. L. & Culver, J. P. Retinotopic mapping of adult human visual cortex with high-density diffuse optical tomography. *Proceedings of the National Academy of Sciences* **104**, 12169-12174 (2007).

6 Wang, L. V. & Wu, H.-i. *Biomedical optics: principles and imaging*. (Wiley-Interscience, Hoboken, N.J., 2007).

7 Srinivasan, S., Pogue, B. W., Jiang, S., Dehghani, H., Kogel, C. *et al.* Interpreting hemoglobin and water concentration, oxygen saturation, and scattering measured in vivo by near-infrared breast tomography. *Proceedings of the National Academy of Sciences of the United States of America* **100**, 12349-12354 (2003).

8 Boas, D. A., Brooks, D. H., Miller, E. L., DiMarzio, C. A., Kilmer, M. *et al.* Imaging the body with diffuse optical tomography. *Signal Processing Magazine, IEEE* **18**, 57-75 (2001).

9 Wang, L., Jacques, S. L. & Zhao, X. Continuous-wave ultrasonic modulation of scattered laser light to image objects in turbid media. *Optics Letters* **20**, 629-631 (1995).

10 Dolfi, D. & Micheron, F. Imaging process and system for transillumination with photon frequency marking. *International Patent* **WO 89/00278** (January 12, 1989).

11 Marks, F. A., Tomlinson, H. W. & Brooksby, G. W. Comprehensive approach to breast cancer detection using light: photon localization by ultrasound modulation

and tissue characterization by spectral discrimination. *Proceedings of SPIE* **1888**, 500-510 (1993).

12 Lévêque-Fort, S. Three-dimensional acousto-optic imaging in biological tissues with parallel signal processing. *Applied Optics* **40**, 1029-1036 (2001).

13 Wang, L. V. & Ku, G. Frequency-swept ultrasound-modulated optical tomography of scattering media. *Optics Letters* **23**, 975-977 (1998).

14 Yao, G., Jiao, S. & Wang, L. V. Frequency-swept ultrasound-modulated optical tomography in biological tissue by use of parallel detection. *Optics Letters* **25**, 734-736 (2000).

15 Forget, B.-C., Ramaz, F., Atlan, M., Selb, J. & Boccara, A.-C. High-contrast fast fourier transform acousto-optical tomography of phantom tissues with a frequency-chirp modulation of the ultrasound. *Applied Optics* **42**, 1379-1383 (2003).

16 Lesaffre, M., Farahi, S., Gross, M., Delaye, P., Boccara, C. *et al.* Acousto-optical coherence tomography using random phase jumps on ultrasound and light. *Optics Express* **17**, 18211-18218 (2009).

17 Wang, L. V. *Photoacoustic imaging and spectroscopy*. (CRC, Boca Raton, FL, 2009).

18 Lev, A. & Sfez, B. G. Pulsed ultrasound-modulated light tomography. *Optics Letters* **28**, 1549-1551 (2003).

19 Gross, M., Goy, P. & Al-Koussa, M. Shot-noise detection of ultrasound-tagged photons in ultrasound-modulated optical imaging. *Optics Letters* **28**, 2482-2484 (2003).

20 Atlan, M., Forget, B. C., Ramaz, F., Boccara, A. C. & Gross, M. Pulsed acousto-optic imaging in dynamic scattering media with heterodyne parallel speckle detection. *Optics Letters* **30**, 1360-1362 (2005).

21 Murray, T. W., Sui, L., Maguluri, G., Roy, R. A., Nieva, A. *et al.* Detection of ultrasound-modulated photons in diffuse media using thephotorefractive effect. *Optics Letters* **29**, 2509-2511 (2004).

22 Bossy, E., Sui, L., Murray, T. W. & Roy, R. A. Fusion of conventional ultrasound imaging and acousto-optic sensing by use of a standard pulsed-ultrasound scanner. *Optics Letters* **30**, 744-746 (2005).

23 Sakadžić, S. & Wang, L. V. High-resolution ultrasound-modulated optical tomography in biologicaltissues. *Optics Letters* **29**, 2770-2772 (2004).

24 Kothapalli, S.-R. & Wang, L. V. Ultrasound-modulated optical microscopy. *Journal of Biomedical Optics* **13**, 054046-054048 (2008).

25 Rousseau, G., Blouin, A. & Monchalin, J.-P. Ultrasound-modulated optical imaging using a high-power pulsed laser and a double-pass confocal Fabry?Perot interferometer. *Optics Letters* **34**, 3445-3447 (2009).

26 Lev, A., Kotler, Z. & Sfez, B. G. Ultrasound tagged light imaging in turbid media in a reflectance geometry. *Optics Letters* **25**, 378-380 (2000).

27 Li, J., Sakadžić, S., Ku, G. & Wang, L. V. Transmission- and side-detection configurations in ultrasound-modulated optical tomography of thick biological tissues. *Applied Optics* **42**, 4088-4094 (2003).

28 Hisaka, M. Ultrasound-modulated optical speckle measurement for scattering medium in a coaxial transmission system. *Applied Physics Letters* **87**, 063504-063503 (2005).

29 Hisaka, M. Ultrasound-modulated optical parallel speckle measurement with stroboscopic illumination in a coaxial reflection system. *Applied Physics Letters* **88**, 033901-033903 (2006).

30 Kim, C., Song, K. H., Maslov, K. & Wang, L. V. Ultrasound-modulated optical tomography in reflection mode with ring-shaped light illumination. *Journal of Biomedical Optics* **14**, 024015-024013 (2009).

31 Lev, A. & Sfez, B. G. Direct, noninvasive detection of photon density in turbid media. *Optics Letters* **27**, 473-475 (2002).

32 Lev, A., Rubanov, E., Sfez, B., Shany, S. & Foldes, A. J. Ultrasound-modulated light tomography assessment of osteoporosis. *Optics Letters* **30**, 1692-1694 (2005).

33 Kobayashi, M., Mizumoto, T., Shibuya, Y., Enomoto, M. & Takeda, M. Fluorescence tomography in turbid media based on acousto-optic modulation imaging. *Applied Physics Letters* **89**, 181102-181103 (2006).

34 Hisaka, M. & Sasakura, Y. Coaxial ultrasound-modulated optical spectroscopy in scattering medium. *Applied Physics Letters* **92**, 163901-163903 (2008).

35 Kim, C. & Wang, L. V. Multi-optical-wavelength ultrasound-modulated optical tomography: a phantom study. *Optics Letters* **32**, 2285-2287 (2007).

36 Kim, C., Song, K. H. & Wang, L. V. Sentinel lymph node detection ex vivo using ultrasound-modulated optical tomography. *Journal of Biomedical Optics* **13**, 020507-020503 (2008).

37 Schenk, J. O. & Brezinski, M. E. Ultrasound induced improvement in optical coherence tomography (OCT) resolution. *Proceedings of the National Academy of Sciences of the United States of America* **99**, 9761-9764 (2002).

38 Yao, G. & Wang, L. V. Signal dependence and noise source in ultrasound-modulated optical tomography. *Applied Optics* **43**, 1320-1326 (2004).

39 Gross, M., Goy, P., Forget, B. C., Atlan, M., Ramaz, F. *et al.* Heterodyne detection of multiply scattered monochromatic light with a multipixel detector. *Optics Letters* **30**, 1357-1359 (2005).

40 Steel, W. H. Luminosity, throughput, or *etendue*? *Applied Optics* **13**, 704-705 (1974).

41 Dewhurst, R. J. & Shan, Q. Optical remote measurement of ultrasound. *Measurement Science and Technology* **10**, R139 (1999).

42 Siegman, A. E. The antenna properties of optical heterodyne receivers. *Applied Optics* **5**, 1588-1594 (1966).

43 Lai, P., Roy, R. A. & Murray, T. W. Quantitative characterization of turbid media using pressure contrast acousto-optic imaging. *Optics Letters* **34**, 2850-2852 (2009).

44 Blonigen, F. J., Nieva, A., DiMarzio, C. A., Manneville, S., Sui, L. *et al.* Computations of the acoustically induced phase shifts of optical paths in acoustophotonic imaging with photorefractive-based detection. *Applied Optics* **44**, 3735-3746 (2005).

45 Sui, L., Roy, R. A., DiMarzio, C. A. & Murray, T. W. Imaging in diffuse media with pulsed-ultrasound-modulated light and the photorefractive effect. *Applied Optics* **44**, 4041-4048 (2005).

46 Ramaz, F., Forget, B., Atlan, M., Boccara, A. C., Gross, M. *et al.* Photorefractive detection of tagged photons in ultrasound modulated optical tomography of thick biological tissues. *Optics Express* **12**, 5469-5474 (2004).

47 Gross, M., Lesaffre, M., Ramaz, F., Delaye, P., Roosen, G. *et al.* Detection of the tagged or untagged photons in acousto-optic imaging of thick highly scattering media by photorefractive adaptive holography. *The European Physical Journal E: Soft Matter and Biological Physics* **28**, 173-182 (2009).

48 Chang, T. Y., Chiou, A. E. & Yeh, P. Cross-polarization photorefractive two-beam coupling in gallium arsenide. *Journal of the Optical Society of America B* **5**, 1724-1729 (1988).

49 Lesaffre, M., Jean, F., Ramaz, F., Boccara, A. C., Gross, M. *et al.* In situ monitoring of the photorefractive response time in a self-adaptive wavefront holography setup developed for acousto-optic imaging. *Optics Express* **15**, 1030-1042 (2007).

50 Yeh, P. *Introduction to photorefractive nonlinear optics*. (J. Wiley & Sons, New York, NY, 1993).

51 Monchalin, J. P. Optical detection of ultrasound. *Ultrasonics, Ferroelectrics and Frequency Control, IEEE Transactions on* **33**, 485-499 (1986).

52 Saleh, B. E. A. & Teich, M. C. *Fundamentals of photonics*. (John Wiley & Sons, Hoboken, NJ, 2007).

53 Gunter, P. a., Huignard, J.-P. *Photorefractive materials and their applications*. (Springer, New York, NY, 2006).

54 Xu, X., Zhang, H., Hemmer, P., Qing, D.-k., Kim, C. *et al.* Photorefractive detection of tissue optical and mechanical properties by ultrasound modulated optical tomography. *Optics Letters* **32**, 656-658 (2007).

55 Cronin-Golomb, M., Fischer, B., White, J. & Yariv, A. Theory and applications of four-wave mixing in photorefractive media. *Quantum Electronics, IEEE Journal of* **20**, 12-30 (1984).

56 Ostroverkhova, O. & Moerner, W. E. Organic photorefractives: mechanisms, materials, and applications. *Chemical Reviews* **104**, 3267-3314 (2004).

57 Kempe, M., Larionov, M., Zaslavsky, D. & Genack, A. Z. Acousto-optic tomography with multiply scattered light. *Journal of the Optical Society of America A* **14**, 1151-1158 (1997).

58 de Montmorillon, L.-A. & Delaye, P. Novel theoretical aspects on photorefractive ultrasonic detection and implementation of a. *Journal of Applied Physics* **82**, 5913 (1997).

59 Wang, L. & Zhao, X. Ultrasound-modulated optical tomography of absorbing objects buried in dense tissue-simulating turbid media. *Applied Optics* **36**, 7277-7282 (1997).

60 Leutz, W. & Maret, G. Ultrasonic modulation of multiply scattered light. *Physica B: Condensed Matter* **204**, 14-19 (1995).

61 Wang, L. V. Mechanisms of ultrasonic modulation of multiply scattered coherent light: an analytic model. *Physical Review Letters* **87**, 043903 (2001).

62 Nightingale, K. R., Nightingale, R. W., Palmeri, M. L. & Trahey, G. E. A finite element model of remote palpation of breast lesions using radiation force: Factors affecting tissue displacement. *Ultrason. Imaging* **22**, 35-54 (2000).

63 Nightingale, K., Soo, M. S., Nightingale, R. & Trahey, G. Acoustic radiation force impulse imaging: in vivo demonstration of clinical feasibility. *Ultrasound in Medicine & Biology* **28**, 227-235 (2002).

64 Torr, G. R. The acoustic radiation force. *American Journal of Physics* **52**, 402-408 (1984).

65 Sugimoto, T., Ueha, S. & Itoh, K. in *IEEE 1990 Ultrasonics Symposium : Proceedings, Vols 1-3 Ultrasonics Symposium* (ed B. R. McAvoy) 1377-1380 (IEEE, 1990).

66 Fatemi, M. & Greenleaf, J. F. Ultrasound-stimulated vibro-acoustic spectrography. *Science* **280**, 82-85 (1998).

67 *American Institute of Ultrasound in Medicine, "Mammalian in vivo ultrasonic biological effects"*, (1992).

68 Khoury, J., Kane, J. S., Gianino, P. D., Hemmer, P. L. & Woods, C. L. Homodyne and heterodyne imaging through a scattering medium. *Optics Letters* **26**, 1433-1435 (2001).

69 Hale, T. C. & Telschow, K. Optical lock-in vibration detection using photorefractive frequency domain processing. *Applied Physics Letters* **69**, 2632-2634 (1996).

70 Tuchin, V. V. *Tissue optics: light scattering methods and instruments for medical diagnosis*. (SPIE Press, Bellingham, WA, 2007).

71 Grunnet-Jepsen, A., Thompson, C. L., Twieg, R. J. & Moerner, W. E. Amplified scattering in a high-gain photorefractive polymer. *Journal of the Optical Society of America B* **15**, 901-904 (1998).

72 Leahy, M. R. & McGee, D. J. Influence of pump beam diameter on beam fanning in a doped photorefractive polymer composite. *Optics Communications* **187**, 277-282 (2001).

73 Anderson, D. Z. & Feinberg, J. Optical novelty filters. *Quantum Electronics, IEEE Journal of* **25**, 635-647 (1989).

74 Cronin-Golomb, M., Biernacki, A. M., Lin, C. & Kong, H. Photorefractive time differentiation of coherent optical images. *Optics Letters* **12**, 1029-1031 (1987).

75 Cudney, R. S., Pierce, R. M. & Feinberg, J. The transient detection microscope. *Nature* **332**, 424-426 (1988).

76 Khoury, J., Woods, C. L. & Cronin-Golomb, M. Noise reduction using adaptive spatial filtering in photorefractive two-beam coupling. *Optics Letters* **16**, 747-749 (1991).

77 Anderson, D., Damiao, V., Popovic, D., Popovic, Z., Romisch, S. *et al.* -70 dB optical carrier suppression by two-beam coupling in photorefractive media. *Appl Phys B-Lasers O* **72**, 743-748 (2001).

78 Deng, Z., Qing, D.-K., Hemmer, P., Ooi, C. H. R., Zubairy, M. S. *et al.* Time-bandwidth problem in room temperature slow light. *Physical Review Letters* **96**, 023602 (2006).

79 Goonesekera, A., Wright, D. & Moerner, W. E. Image amplification and novelty filtering with a photorefractive polymer. *Applied Physics Letters* **76**, 3358-3360 (2000).

80 Hendrickx, E., Van Steenwinckel, D. & Persoons, A. Tracking novelty filter at 780 nm based on a photorefractive polymer in a two-beam coupling geometry. *Applied Optics* **40**, 1412-1416 (2001).

81 Zhang, C., Chen, G., Wei, X., Guo, Z., Tian, J. *et al.* Optical novelty filter using bacteriorhodopsin film. *Optics Letters* **30**, 81-83 (2005).

82 L. F. Johnson, G. D. Boyd & Nassau, K. Optical maser characteristics of Tm^{+3} in $CaWO_4$. *Proceedings of the IRE* **50**, 86-87 (1962).

83 Kitagawa, T., Hattori, K., Shuto, K., Yasu, M., Kobayashi, M. *et al.* Amplification in erbium-doped silica-based planar lightwave circuits. *Electronics Letters* **28**, 1818-1819 (1992).

84 Lin, S., Feuerstein, R. J. & Mickelson, A. R. A study of neodymium-chelate-doped optical polymer waveguides. *Journal of Applied Physics* **79**, 2868-2874 (1996).

85 Macfarlane, R. M. & Shelby, R. M. *Spectroscopy of solids containing rare earth ions*. (North-Holland, Amsterdam, 1987).

86 Freeman, A. J. & Watson, R. E. Theoretical investigation of some magnetic and spectroscopic properties of rare-earth ions. *Physical Review* **127**, 2058 (1962).

87 Dieke, G. H. & Crosswhite, H. M. The spectra of the doubly and triply ionized rare earths. *Applied Optics* **2**, 675-686 (1963).

88 Judd, B. R. Optical absorption intensities of rare-earth ions. *Physical Review* **127**, 750 (1962).

89 Baker, J. M. & Bleaney, B. Paramagnetic resonance in some lanthanon ethyl sulphates. *Proceedings of the Royal Society of London. Series A, Mathematical and Physical Sciences* **245**, 156-174 (1958).

90 Holliday, K., Croci, M., Vauthey, E. & Wild, U. P. Spectral hole burning and holography in an $Y_2SiO_5:Pr^{3+}$ crystal. *Physical Review B* **47**, 14741 (1993).

91 Macfarlane, R. M. & Shelby, R. M. Magnetic field dependent optical dephasing in $LaF_3:Er^{3+}$. *Optics Communications* **42**, 346-350 (1982).

92 Macfarlane, R. M. Photon-echo measurements on the trivalent thulium ion. *Optics Letters* **18**, 1958-1960 (1993).

93 Ganem, J., Wang, Y. P., Boye, D., Meltzer, R. S., Yen, W. M. *et al.* Nonexponential photon-echo decays of paramagnetic ions in the superhyperfine limit. *Physical Review Letters* **66**, 695 (1991).

94 Wang, G. M., Equall, R. W., Cone, R. L., Leask, M. J. M., Godfrey, K. W. *et al.* Optical dephasing mechanisms in $Tm^{3+}:Y_2Si2O_7$. *Optics Letters* **21**, 818-820 (1996).

95 Macfarlane, R. M. Photon echoes in rare earth doped solids – a materials perspective. *Laser Physics* **5**, 6 (1995).

96 Orbach, R. Spin-lattice relaxation in rare-earth salts. *Proceedings of the Royal Society of London. Series A. Mathematical and Physical Sciences* **264**, 458-484 (1961).

97 Ham, B. S., Shahriar, M. S., Kim, M. K. & Hemmer, P. R. Frequency-selective time-domain optical data storage by electromagnetically induced transparency in a rare-earth-doped solid. *Optics Letters* **22**, 1849-1851 (1997).

98 Taylor, D. R. & Hessler, J. P. Photon echo decay in ruby: electric dipole interactions and instantaneous diffusion. *Physics Letters A* **50**, 205-207 (1974).

99 Huang, J., Zhang, J. M., Lezama, A. & Mossberg, T. W. Excess dephasing in photon-echo experiments arising from excitation-induced electronic level shifts. *Physical Review Letters* **63**, 78 (1989).

100 Liu, G. K. & Cone, R. L. Laser-induced instantaneous spectral diffusion in Tb^{3+} compounds as observed in photon-echo experiments. *Physical Review B* **41**, 6193 (1990).

101 Nilsson, M. *Coherent interactions in rare-earth-ion-doped crystals for applications in quantum information science*, Lund Institute of Technology, Lund, Sweden, (2004).

102 Nilsson, M., Rippe, L., Kröll, S., Klieber, R. & Suter, D. Hole-burning techniques for isolation and study of individual hyperfine transitions in inhomogeneously broadened solids demonstrated in Pr^{3+}:Y_2SiO_5. *Physical Review B* **70**, 214116 (2004).

103 Macfarlane, R. M. High-resolution laser spectroscopy of rare-earth doped insulators: a personal perspective. *Journal of Luminescence* **100**, 1-20 (2002).

104 Armagan, G., Buoncristiani, A. M. & Di Bartolo, B. Excited state dynamics of thulium ions in yttrium aluminum garnets. *Optical Materials* **1**, 11-20 (1992).

105 Hesselink, W. H. & Wiersma, D. A. Photon echoes stimulated from an accumulated grating: Theory of generation and detection. *The Journal of Chemical Physics* **75**, 4192-4197 (1981).

106 Mitsunaga, M., Kubodera, K.-i. & Kanbe, H. Effects of hyperfine structures on an optical stimulated echo memory device. *Optics Letters* **11**, 339-341 (1986).

107 Ohlsson, N., Nilsson, M., Krll, S. & Mohan, R. K. Long-time-storage mechanism for Tm:YAG in a magnetic field. *Optics Letters* **28**, 450-452 (2003).

108 Guillot-Noël, O., Goldner, P., Antic-Fidancev, E. & Le Gouët, J. L. Analysis of magnetic interactions in rare-earth-doped crystals for quantum manipulation. *Physical Review B* **71**, 174409 (2005).

109 de Seze, F., Louchet, A., Crozatier, V., Lorgeré, I., Bretenaker, F. *et al.* Experimental tailoring of a three-level Lambda system in Tm^{3+}:YAG. *Physical Review B* **73**, 085112 (2006).

110 Sun, Y., Wang, G. M., Cone, R. L., Equall, R. W. & Leask, M. J. M. Symmetry considerations regarding light propagation and light polarization for coherent interactions with ions in crystals. *Physical Review B* **62**, 15443 (2000).

111 Macfarlane, R. M. Direct process thermal line broadening in Tm:YAG. *Journal of Luminescence* **85**, 181-186 (2000).

112 Li, C., Wyon, C. & Moncorge, R. Spectroscopic properties and fluorescence dynamics of Er^{3+} and Yb^{3+} in Y_2SiO_5. *Quantum Electronics, IEEE Journal of* **28**, 1209-1221 (1992).

113 Equall, R. W., Cone, R. L. & Macfarlane, R. M. Homogeneous broadening and hyperfine structure of optical transitions in Pr^{3+}:Y_2SiO_5. *Physical Review B* **52**, 3963 (1995).

114 Graf, F. R., Renn, A., Zumofen, G. & Wild, U. P. Photon-echo attenuation by dynamical processes in rare-earth-ion-doped crystals. *Physical Review B* **58**, 5462 (1998).

115 Graf, F. R., Plagemann, B. H., Renn, A., Wild, U. P. & Mitsunaga, M. Total dephasing-rephasing balancing in Stark-pulse-modulated photon echoes. *Optics Letters* **22**, 181-183 (1997).

116 Graf, F. R., Renn, A., Wild, U. P. & Mitsunaga, M. Site interference in Stark-modulated photon echoes. *Physical Review B* **55**, 11225 (1997).

117 Ham, B. S., Hemmer, P. R. & Shahriar, M. S. Efficient electromagnetically induced transparency in a rare-earth doped crystal. *Optics Communications* **144**, 227-230 (1997).

118 Turukhin, A. V., Sudarshanam, V. S., Shahriar, M. S., Musser, J. A., Ham, B. S. *et al.* Observation of ultraslow and stored light pulses in a solid. *Physical Review Letters* **88**, 023602 (2001).

119 Ham, B. S., Shahriar, M. S. & Hemmer, P. R. Radio-frequency-induced optical gain in Pr^{3+}:Y_2SiO_5. *Journal of the Optical Society of America B* **15**, 1541-1544 (1998).

120 Ham, B. S., Shahriar, S. M. & Hemmer, P. R. Electromagnetically induced transparency over spectral hole-burning temperature in a rare-earth?doped solid. *Journal of the Optical Society of America B* **16**, 801-804 (1999).

121 Meystre, P. & Sargent, M. *Elements of quantum optics*. 3rd edn, (Springer, New York, NY, 1999).

122 Colice, M., Schlottau, F. & Wagner, K. H. Broadband radio-frequency spectrum analysis in spectral-hole-burning media. *Applied Optics* **45**, 6393-6408 (2006).

123 Burr, G. W., Harris, T. L., Babbitt, W. R. & Jefferson, C. M. Incorporating excitation-induced dephasing into the Maxwell-Bloch numerical modeling of photon echoes. *Journal of Luminescence* **107**, 314-331 (2004).

124 Hayes, M. H. *Statistical digital signal processing and modeling*. (John Wiley & Sons, Inc., New York, NY, 1996).

125 Dalecki, D. Mechanical bioeffects of ultrasound. *Annual Review of Biomedical Engineering* **6**, 229-248 (2004).

126 Hobbs, P. C. D. Ultrasensitive laser measurements without tears. *Applied Optics* **36**, 903-920 (1997).

127 Rousseau, G., Blouin, A. & Monchalin, J.-P. Ultrasound-modulated optical imaging using a high-power pulsed laser and a double-pass confocal Fabry-Perot interferometer. *Optics Letters* **34**, 3445-3447 (2009).

128 Wang, L. V. Multiscale photoacoustic microscopy and computed tomography. *Nature Photonics* **3**, 503-509 (2009).

129 Ku, G. & Wang, L. V. Deeply penetrating photoacoustic tomography in biological tissues enhancedwith an optical contrast agent. *Optics Letters* **30**, 507-509 (2005).

130 Song, K. H. & Wang, L. V. Deep reflection-mode photoacoustic imaging of biological tissue. *Journal of Biomedical Optics* **12**, 060503-060503 (2007).

131 Fink, M. & Tanter, M. Multiwave imaging and super resolution. *Physics Today* **63**, 28-33 (2010).

132 Mahan, G. D., Engler, W. E., Tiemann, J. J. & Uzgiris, E. Ultrasonic tagging of light: Theory. *Proceedings of the National Academy of Sciences of the United States of America* **95**, 14015-14019 (1998).

133 Sakadžić, S. & Wang, L. V. Correlation transfer and diffusion of ultrasound-modulated multiply scattered light. *Physical Review Letters* **96**, 163902 (2006).

134 *American national standard for the safe use of lasers*. ANSI Z136.1-2000 (American National Standards Institute, 2000).

135 Li, Y., Zhang, H., Kim, C., Wagner, K. H., Hemmer, P. *et al.* Pulsed ultrasound-modulated optical tomography using spectral-hole burning as a narrowband spectral filter. *Applied Physics Letters* **93**, 011111-011113 (2008).

136 Li, Y., Hemmer, P., Kim, C., Zhang, H. & Wang, L. V. Detection of ultrasound-modulated diffuse photons using spectral-hole burning. *Optics Express* **16**, 14862-14874 (2008).

137 Afzelius, M., Usmani, I., Amari, A., Lauritzen, B., ouml *et al.* Demonstration of atomic frequency comb memory for light with spin-wave storage. *Physical Review Letters* **104**, 040503 (2010).

138 Amari, A., Walther, A., Sabooni, M., Huang, M., Kröll, S. *et al.* Towards an efficient atomic frequency comb quantum memory. *Journal of Luminescence* **130**, 1579-1585 (2010).

139 Sabooni, M., Beaudoin, F., Walther, A., Lin, N., Amari, A. *et al.* Storage and Recall of Weak Coherent Optical Pulses with an Efficiency of 25%. *Physical Review Letters* **105**, 060501 (2010).

140 Hedges, M. P., Longdell, J. J., Li, Y. & Sellars, M. J. Efficient quantum memory for light. *Nature* **465**, 1052-1056 (2010).

141 Moerner, W. E. *Persistent spectral hole-burning: science and applications*. (Springer-Verlag New York Inc., New York, NY, 1988).

142 Ham, B. S., Hemmer, P. R. & Shahriar, M. S. Efficient phase conjugation via two-photon coherence in an optically dense crystal. *Physical Review A* **59**, R2583 (1999).

143 Julsgaard, B., Walther, A., Kröll, S. & Rippe, L. Understanding laser stabilization using spectral hole burning. *Optics Express* **15**, 11444-11465 (2007).

144 Liu, G. & Jacquier, B. *Spectroscopic properties of rare earths in optical materials*. (Springer, Berlin; New York, 2005).

145 Silver, M. S., Joseph, R. I., Chen, C. N., Sank, V. J. & Hoult, D. I. Selective population inversion in NMR. *Nature* **310**, 681-683 (1984).

146 Rippe, L., Nilsson, M., Kr, ouml, ll, S. *et al.* Experimental demonstration of efficient and selective population transfer and qubit distillation in a rare-earth-metal-ion-doped crystal. *Physical Review A* **71**, 062328 (2005).

147 Nilsson, M. & Kröll, S. Solid state quantum memory using complete absorption and re-emission of photons by tailored and externally controlled inhomogeneous absorption profiles. *Optics Communications* **247**, 393-403 (2005).

148 Bushberg, J. T. *The essential physics of medical imaging*. 2nd edn, (Lippincott Williams & Wilkins, Philadelphia, PA, 2002).

149 Farahi, S., Montemezzani, G., Grabar, A. A., Huignard, J.-P. & Ramaz, F. Photorefractive acousto-optic imaging in thick scattering media at 790 nm with a $Sn_2P_2S_6$:Te crystal. *Optics Letters* **35**, 1798-1800 (2010).

150 Mackowiak, S. A., Herman, T. K. & Kaufman, L. J. Spatial and temporal heterogeneity in supercooled glycerol: Evidence from wide field single molecule imaging. *The Journal of Chemical Physics* **131**, 244513-244514 (2009).

151 F. Beaudoux, B. Tumino, A. Ferrier, R. Marino, J. Lejay *et al.* Photon echo radiated by a polycrystalline and opaque powder. *arXiv:1006.4887v1* (2010).

152 Hau, L. V., Harris, S. E., Dutton, Z. & Behroozi, C. H. Light speed reduction to 17 metres per second in an ultracold atomic gas. *Nature* **397**, 594-598 (1999).

153 Phillips, D. F., Fleischhauer, A., Mair, A., Walsworth, R. L. & Lukin, M. D. Storage of light in atomic vapor. *Physical Review Letters* **86**, 783 (2001).

154 Khurgin, J. B. & Tucker, R. S. *Slow light: science and applications*. (CRC Press, Boca Raton, FL, 2009).

155 Walther, A., Amari, A., Kroll, S. & Kalachev, A. Experimental superradiance and slow-light effects for quantum memories. *Physical Review A* **80**, 012317 (2009).

156 Rebane, A., Shakhmuratov, R. N., Mégret, P. & Odeurs, J. Slow light with persistent spectral hole burning in waveguides. *Journal of Luminescence* **127**, 22-27 (2007).

157 Lauro, R., Chanelière, T. & Le Gouët, J. L. Slow light using spectral hole burning in a Tm^{3+}-doped yttrium-aluminum-garnet crystal. *Physical Review A* **79**, 063844 (2009).

158 Chang, T., Tian, M., Mohan, R. K., Renner, C., Merkel, K. D. *et al.* Recovery of spectral features readout with frequency-chirped laser fields. *Optics Letters* **30**, 1129-1131 (2005).

159 Shakhmuratov, R. N., Rebane, A., eacute, gret, P. & Odeurs, J. Slow light with persistent hole burning. *Physical Review A* **71**, 053811 (2005).

160 Sakadžić, S. & Wang, L. V. Correlation transfer equation for multiply scattered light modulated by an ultrasonic pulse. *Journal of the Optical Society of America A* **24**, 2797-2806 (2007).

161 George B. Arfken & Weber, H. J. *Mathematical methods for physicists*. 6th edn, (Elsevier Academic Press, Burlington, MA, 2005).

APPENDIX

CALCULATION FOR TWO-LEVEL SHB FOR UOT

1. Calculation procedure for equation (4.30)

$$\int_{-\infty}^{\infty} d\omega' \frac{\dfrac{1}{\gamma + i(\omega' - \nu_P)}}{1 + \left[I_P(\nu_P, z) / I_{sat} \right] \dfrac{\gamma^2}{\gamma^2 + (\omega' - \nu_P)^2}} = \int_{-\infty}^{\infty} d\omega' \frac{\dfrac{\gamma - i(\omega' - \nu_P)}{\gamma^2 + (\omega' - \nu_P)^2}}{1 + \left[I_P(\nu_P, z) / I_{sat} \right] \dfrac{\gamma^2}{\gamma^2 + (\omega' - \nu_P)^2}} \tag{A.1}$$

let $\omega' - \nu_P = x$, $d\omega' = dx$;

$$\begin{aligned} &\int_{-\infty}^{\infty} dx \frac{\dfrac{\gamma - ix}{\gamma^2 + x^2}}{1 + \left[I_P(\nu_P, z) / I_{sat} \right] \dfrac{\gamma^2}{\gamma^2 + x^2}} \\ &= \int_{-\infty}^{\infty} dx \left\{ \frac{\gamma}{\gamma^2 + x^2 + \left[I_P(\nu_P, z) / I_{sat} \right] \gamma^2} - i \frac{x}{\gamma^2 + x^2 + \left[I_P(\nu_P, z) / I_{sat} \right] \gamma^2} \right\} \end{aligned} \tag{A.2}$$

The second term of integral is 0, For the first integral,

$$\int_{-\infty}^{\infty} dx \frac{\gamma}{\gamma^2 + x^2 + \left[I_P(\nu_P, z) / I_{sat} \right] \gamma^2} = \int_{-\infty}^{\infty} dx \frac{1}{\gamma \left\{ 1 + \left[I_P(\nu_P, z) / I_{sat} \right] \right\} \left\{ 1 + \dfrac{x^2}{\gamma^2 \left\{ 1 + \left[I_P(\nu_P, z) / I_{sat} \right] \right\}} \right\}}$$

remember that $\int_{-\infty}^{\infty} \frac{dz}{z^2 + 1} = \pi$,

so we have $\dfrac{\pi}{\sqrt{1 + \left[I_P(\nu_P, z) / I_{sat} \right]}}$

$$\alpha(\nu_S,\nu_P,z)=\frac{\alpha_0 G(\nu_S)\pi}{T_2\sqrt{1+\left[I_P(\nu_P,z)/I_{sat}\right]}}=\frac{\alpha'_0(\nu_S)}{\sqrt{1+\left[I_P(\nu_P,z)/I_{sat}\right]}}, \tag{A.3}$$

Here $\alpha'_0(\nu_S)=\alpha_0\gamma\pi G(\nu_S)$ (A.4)

2. Calculation procedure for equation (4.32)

$$\int_{-\infty}^{\infty}\frac{-i}{\delta'-i\gamma}d\delta' \tag{A.5}$$

Consider the contour C as shown in Fig. A-1.

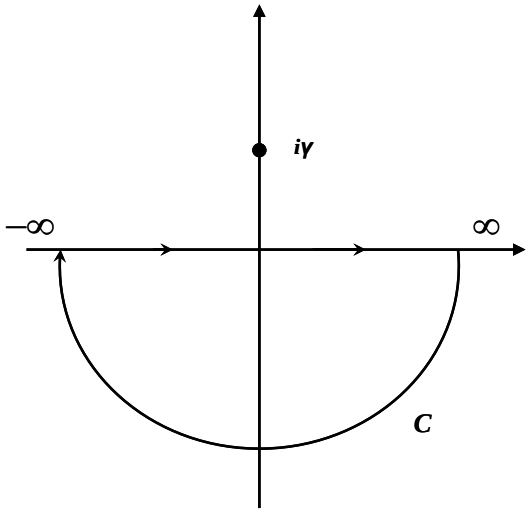

Figure A-1 | Integration contour C. $\int_{-\infty}^{\infty}\frac{-i}{\delta'-i\gamma}d\delta'+\int_C\frac{-i}{\delta'-i\gamma}d\delta'=0$

let $\delta'=Re^{i\theta}$, $d\delta'=iRe^{i\theta}d\theta$,

$$-\int_C\frac{-i}{\delta'-i\gamma}d\delta'=-\int_0^{-\pi}\frac{-i}{\mathrm{Re}^{i\theta}-i\gamma}iRe^{i\theta}d\theta=\lim_{R\to\infty}\left[-\int_0^{-\pi}\frac{1}{1-\frac{i\gamma}{\mathrm{Re}^{i\theta}}}d\theta\right]=\pi,$$

so we have

$$\int_{-\infty}^{\infty} \frac{-i}{\delta' - i\gamma} d\delta' = \pi . \tag{A.6}$$

For the second part integral, we need residue theorem[161]. Consider the integration path as shown in Fig. A-2.

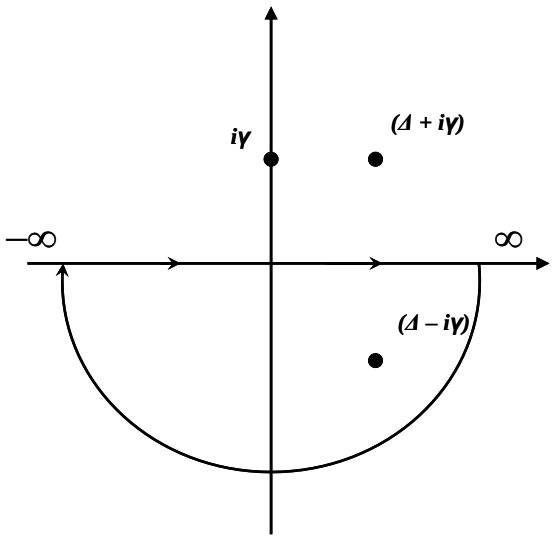

Figure A-2 | Integration contour calculated with residue theorem.

$$\mathrm{Res}\left(f, \delta'\right) = \lim_{\delta' \to \Delta - i\gamma} \left[\left(\delta' - \Delta + i\gamma'\right) \frac{i}{\delta' - i\gamma} \frac{\gamma^2 I_2}{\left(\delta' - \Delta\right)^2 + \gamma'^2} \right] \tag{A.7}$$

where $\gamma' = \sqrt{1 + I_2}\gamma$. After some algebra, we get

$$\mathrm{Res}\left(f, \delta'\right) = -\frac{\gamma^2 I_2}{2\gamma'} \frac{\Delta + i\left(\gamma' + \gamma\right)}{\Delta^2 + \left(\gamma' + \gamma\right)^2} \tag{A.8}$$

Since the integration path is clockwise, we have

$$\int_{-\infty}^{\infty} d\delta' \frac{i}{\delta' - i\gamma} \frac{\gamma^2 I_2}{\left(\delta' - \Delta\right)^2 + \gamma'^2} = -2\pi i \,\mathrm{Re}\, s\left(f, \delta'\right) = \frac{\pi\gamma^2 I_2}{\gamma'} \frac{i\Delta - \left(\gamma' + \gamma\right)}{\Delta^2 + \left(\gamma' + \gamma\right)^2} \tag{A.9}$$

In all, we have

$$\alpha\left(\nu_S, \nu_P, z\right) = \alpha'_0\left(\nu_S\right)\left[1 - \frac{\gamma^2 I_2}{\gamma'} \frac{\left(\gamma' + \gamma\right) - i\Delta}{\Delta^2 + \left(\gamma' + \gamma\right)^2}\right] \tag{A.10}$$

VITA

Huiliang Zhang was born in Shanghai, China. He received BS degree from Microelectronics Department, Peking University, Beijing, China in July, 2003. He received his Ph.D. in 2010 in the Electrical and Computer Engineering Department, Texas A&M University, College Station. His research focuses on development of novel detection techniques of ultrasound-modulated optical tomography deep inside soft biological tissue. Successful experiments include nonlinear optics approach with photorefractive materials and quantum optics approach with spectral-hole burning materials. He is also experienced with single molecule detection/single spin resonance imaging with nitrogen-vacancy defect center in diamond and atomic force microscope related nano-fabrication techniques. Mr. Zhang may be reached at Department of Electrical and Computer Engineering, c/o Dr. Philip Hemmer, Texas A&M University, College Station, TX 77843-3128. His email is aggiezhl@gmail.com